

Abstract

Nelson, Andrew Lincoln: Characterization of Winding Faults in Axial Flux Reluctance Motors in the Context of Electric Vehicle Propulsion Systems. (Under the direction of Dr. Mo-Yuen Chow.)

Since the late 1980's there has been a major resurgence in electric vehicle propulsion research and development. This trend has been stimulated by various factors, including rising fossil fuel costs, environmental concerns, and developments in technologies, such as improved permanent magnets, switching transistors and storage batteries. New technology has allowed motor types previously not suitable for use in electric vehicles, such as variable reluctance permanent magnet motors and brushless DC motors, to be adapted for use as electric vehicle propulsion systems.

The process of motor fault detection and diagnosis is becoming an important part of electric motor applications, including electric vehicle propulsion. A key element in this process, when applied to a particular motor topology, is the characterization of motor faults in the context of that particular motor type. This research examines one class of motor faults, namely stator winding faults, in an axial flux variable reluctance permanent magnet motor. The research focuses on two types of winding faults. The first of these is an insulation failure induced turn-to-turn stator coil short in which a significant portion of the coil has been shorted out. This type of fault can be the result of a single insulation failure between two adjacent coil turns if the turns happen to be in adjacent winding ranks. The second fault considered is one in which a portion of the coil is actually destroyed or removed in a manner that allows the remainder of the coil to continue to carry current.

To facilitate the study of stator winding faults in variable reluctance motors, a prototype axial flux variable reluctance permanent magnet motor was designed and built. The motor was equipped with experimental fault simulation stator windings capable of simulating several types of winding faults. A salient finding of this research is that two

common types of winding faults can be differentiated by their effects on rotor velocity in this type of motor. It is found that turn-to-turn stator winding faults cause a damping in rotor velocity due to permanent magnet rotor induced current in the shorted portion of the coil. In contrast, coil faults with a reduced number of turns, but without the presence of coil shorts, result in a slight increase in rotor velocity.

**CHARACTERIZATION OF WINDING FAULTS IN AXIAL FLUX
RELUCTANCE MOTORS IN THE CONTEXT OF ELECTRIC VEHICLE
PROPULSION SYSTEMS**

By

ANDREW LINCOLN NELSON

A Thesis Submitted to the Graduate Faculty of North Carolina State University in Partial
Fulfillment for the Degree of Master of Science

DEPARTMENT OF ELECTRICAL AND COMPUTER ENGINEERING

Raleigh

2000

APPROVED BY:

Chair of Advisory Committee

Dedication

To my parents, Dr. David Alan Nelson and Dr. Joan Blackadar Nelson.

Biography

Andrew Lincoln Nelson was born on February 28, 1967 in Laramie, Wyoming to Joan Blackadar Nelson and David Alan Nelson. He received his B.S. in Computer Science from The Evergreen State College, Olympia, Washington in 1991. He received his M.S. in Electrical and Computer Engineering from North Carolina State University, Raleigh, North Carolina in 2000.

Acknowledgements

I would like to thank my advisor, Dr. Mo-Yuen Chow, for the opportunity to pursue this degree. I would like to thank my fellow graduate students for their support, especially Yodyium Tipsuwan. Most of all, I would like to thank Julia A. Nelson and Dr. Edward Grant, without whose encouragement this thesis could not have been completed.

Table of Contents

LIST OF TABLES	vii
LIST OF FIGURES	viii
INTRODUCTION TO THE THESIS	1
<i>Overview.....</i>	<i>1</i>
<i>Brief Overview of Modern Electric Vehicle Drives</i>	<i>1</i>
<i>Motor Winding Faults in Electric Vehicle Drives.....</i>	<i>3</i>
<i>Research Objectives.....</i>	<i>5</i>
<i>Thesis format</i>	<i>6</i>
ELECTRIC VEHICLES AND AXIAL FLUX PERMANENT MAGNET MOTOR PROPULSION SYSTEMS	7
I. INTRODUCTION.....	7
<i>Overview.....</i>	<i>7</i>
<i>A Brief History of the Electric Vehicle.....</i>	<i>8</i>
<i>New and Emerging Electric Vehicle Propulsion Systems.....</i>	<i>10</i>
II. THE AXIAL FLUX VARIABLE RELUCTANCE PERMANENT MAGNET DISC MOTOR	10
<i>A General Overview of Variable Reluctance Motor Function and Structure</i>	<i>10</i>
<i>A Specific Motor Topology</i>	<i>12</i>
<i>Modes of Operation</i>	<i>14</i>
<i>Advantages and Disadvantages of the Axial Flux Disc Motor</i>	<i>14</i>
III. MULTI-MOTOR AND DIRECT WHEEL DRIVE SYSTEMS IN ELECTRIC VEHICLES	15
<i>General Description</i>	<i>15</i>
<i>Some Examples of Direct Wheel Drive Systems in Electric Vehicles</i>	<i>16</i>
<i>The Four Direct Wheel Drive Electric Vehicle.....</i>	<i>17</i>
IV. CLOSING REMARKS	18
<i>Challenges and opportunities for the future</i>	<i>18</i>
ACKNOWLEDGMENTS	19
REFERENCES	19
DEVELOPMENT OF A MOTOR FAULT SIMULATION PLATFORM FOR EDUCATIONAL AND EXPERIMENTAL PURPOSES USING AN AXIAL FLUX VARIABLE RELUCTANCE DC MOTOR.	20
ABSTRACT.....	20
I. INTRODUCTION.....	21
II. MOTOR PHYSICAL DESCRIPTION.....	23
III. MATHEMATICAL MODEL.....	27
IV. MOTOR DRIVER STRATEGIES	31
<i>Driver types</i>	<i>31</i>
<i>Stepping Motor Driver.....</i>	<i>31</i>
<i>Brushless Motor Driver</i>	<i>35</i>
V. EXPERIMENTAL FAULT SIMULATION PLATFORM DESCRIPTION.....	40
VI. EXAMPLE USES OF THE PLATFORM AND CLOSING REMARKS	43
<i>Some Uses of the Motor Platform.....</i>	<i>43</i>
<i>Closing Remarks.....</i>	<i>44</i>
ACKNOWLEDGMENTS	45
REFERENCES	45

ANALYSIS OF ROTOR VELOCITY DAMPING DUE TO COIL FAULTS IN AN AXIAL FLUX VARIABLE RELUCTANCE PM MOTOR	46
ABSTRACT	46
I. INTRODUCTION.....	47
II. MOTOR DESCRIPTION	48
III. MATHEMATICAL MODEL	52
IV. DESCRIPTION OF EXPERIMENTAL PLATFORM SETUP	56
V. RESULTS	58
VI. DISCUSSION AND ANALYSIS	70
<i>Overview and identification of damping current</i>	<i>70</i>
<i>Formulation of a mathematical expression for damping torque.....</i>	<i>73</i>
<i>Prediction of rotor velocity from measured currents in the turn-to-turn fault case.....</i>	<i>74</i>
<i>Identification of turn-to-turn faults from rotor velocity data.....</i>	<i>77</i>
VII. CONCLUSION.....	78
ACKNOWLEDGMENTS	79
REFERENCES	79
BIBLIOGRAPHY	80
APPENDIX A: MOTOR MECHANICAL DRAWINGS	85
APPENDIX B: MOTOR ELECTRICAL SCHEMATICS.....	93
APPENDIX C: MOTOR FABRICATION PHOTOGRAPHS.....	95

List of Tables

Table 1. Average velocities and percentage of nominal no-fault velocity for cases 1 through 4.....	64
--	----

List of Figures

Figure 2-1. The Honda EV Plus.....	9
Figure 2-2. Cross sectional view of a six coil four pole variable reluctance motor.....	11
Figure 2-3. The ADAC axial flux disc motor.....	12
Figure 2-4. Drawing of the axial flux disc motor.	13
Figure 2-5. A four direct wheel drive arrangement showing motor and controller locations. (a) Each wheel has a disc motor mounted inside its hub. (b) Battery pack. (c) System controller. (d) Accelerator pedal.	18
Figure 3-1. The axial flux variable reluctance DC motor.....	24
Figure 3-2. Top view of the prototype motor showing the relative locations of the rotor poles and the stator coils.....	24
Figure 3-3. Prototype motor stator coil cores:(a) Laminated cores before winding. (b) Laminated cores after winding.....	25
Figure 3-4. Three dimensional motor view highlighting the interaction between two rotor pole sets and two stator coils.	27
Figure 3-5. The idealized unit piecewise linear wave forms, $l_m(\theta)$, and its partial $d l_m(\theta)/d\theta$ with respect to θ . These curves are shown for 360 electrical degrees.	29
Figure 3-6. Time-voltage wave forms supplied to each of the stator phases to implement the half stepping open loop sequence driver scheme.	32
Figure 3-7. Diagram showing the interconnections between the computer, motor, power switching relay array, and power supply in the open loop stepping control.	34
Figure 3-8. Graphic user interface for the PC implemented stepping motor driver.	35
Figure 3-9. Photograph of electronic commutator installed on the prototype motor.....	36
Figure 3-10. The voltage, $v_m(\theta)$, and ideal inductance, $L_m(\theta)$, wave forms with respect to rotor position, θ , when the motor is driven with the brushless driver scheme.	37
Figure 3-11. Schematic diagram of the brushless DC motor driver configuration.	39
Figure 3-12. Photograph of the experimental fault simulation platform in the ADAC laboratory.....	40
Figure 3-13. The experimental fault simulation coil. (a) A photograph of a fault wound coil. (b) Diagram indicating the locations of the fault simulation tap switches.....	41
Figure 3-14. Schematic layout of the fault simulation and data collection platform.....	42

Figure 3-15. Examples of motor data reported by the motor platform graphic user interface. (a) Phase back emf voltage wave forms. (b) Phase voltage and current wave forms.....	43
Figure 4-1. The axial flux variable reluctance DC motor.....	49
Figure 4-2. Top view of the prototype motor showing the relative locations of the rotor poles and the stator coils.....	51
Figure 4-3. The idealized unit piecewise linear wave forms, $l_m(\theta)$, and its partial $d l_m(\theta)/d\theta$ with respect to θ . These curves are shown for 360 electrical degrees.....	54
Figure 4-4. A photograph of the experimental fault simulation platform in the ADAC lab.	56
Figure 4-5. Diagram of the experimental fault simulation coil indicating the locations of the fault simulation tap switches.	57
Figure 4-6. Schematic layout of the fault simulation and data collection platform.....	58
Figure 4-7. Experimental fault simulation phase with tap switches shown: (a) No-fault: 100% switch closed only. (b) Reduced-coil fault: 47% switch closed only. (c) Turn-to-turn short fault: both 47% and 100% switches closed. (d) Open phase: All switches open.	59
Figure 4-8. The prototype motor showing the experimental fault simulation coil and associated tap switch box.	59
Figure 4-9. No fault motor operation data (case 1).....	62
Figure 4-10. Motor operation with the reduced-coil fault (case 2).....	62
Figure 4-11. Motor operation with the turn-to-turn fault (case 3).....	63
Figure 4-12. Motor operation with the open circuit fault (case 4).....	63
Figure 4-13. Schematic circuit diagram of the experimental fault simulation coil and sensor arrangement.....	65
Figure 4-14. Panel (a): Phase current draw for the no-fault case, the reduced-coil fault and the turn-to-turn fault. Panel (b): The differences between each of the two fault cases and the no-fault case are plotted together.	67
Figure 4-15. Panel (a): Phase voltage for the no-fault case, the reduced-coil fault and the turn-to-turn fault. Panel (b): The differences between each of the two fault cases and the no-fault case are plotted together.	68
Figure 4-16. Panel (a): Velocity for the no-fault case, the reduced-coil fault and the turn-to-turn fault. Panel (b): The differences between each of the two fault cases and the no-fault case are plotted together.	69
Figure 4-17. Current draw through the 47% tap switch in each of the four experimental configurations. Data are shown for 360 electrical degrees.....	70

Figure 4-18. Power source and back emf induced current paths in the
turn-to-turn faulted coil..... 71

Figure 4-19. Net current flow in the faulted portion of the experimental
fault simulation coil in the reduced-coil fault case (a), and the
turn-to-turn fault case (b). 72

Introduction to the Thesis

Overview

The work presented here stemmed jointly out of a study of modern electric vehicle drives and from the existing motor fault detection and diagnosis emphasis of the Advanced Diagnosis and Control (ADAC) laboratory in the Electrical and Computer Engineering department at North Carolina State University.

The research presented here focuses on an axial flux variable reluctance permanent magnet motor designed and built in the ADAC laboratory. The motor was originally designed to be similar to a class of experimental electric vehicle drive motors, namely axial flux variable reluctance brushless motors. The motor is a low power machine and is useful mainly for laboratory research purposes. A main consideration affecting the design of the motor was to make it useful for studying motor faults in this class of motors.

This work is also intended to provide a review of modern electric vehicle propulsion motors.

Brief Overview of Modern Electric Vehicle Drives

In the last 15 years many new motor configurations have been proposed for use in electric vehicles. Some of these new motor types have been used in production electric vehicles while others remain in the prototype and development stages. This section contains a brief survey of modern electric vehicle propulsion motors.

The brushed DC motor is still used in some electric vehicles and is often the drive of choice for the hobbyist. Its ease of control and simplicity of design make it amenable for use in do-it-yourself gas to electric conversions. In the 1970s and 80s DC motor drives

were probably the most common electric vehicle on the road. The main drawback with the brushed DC motor is the commutator. The commutator brushes carry high current which results in repeated high power arcing during motor operation. This not only causes constant degradation of the brushes, but also results in a considerable reduction in motor efficiency [1]. The average brushed DC motor is between 75% and 80% efficient.

The Induction motor has been used in several production line vehicles in the U.S. and remains the most common motor in the American electric vehicle market. Initially, its popularity in the automobile industry was due to its low cost and ready availability. This was especially true in the case of General Motors, which has used induction motors in almost all of its production electric vehicles in the last decade [2].

More recently, the brushless DC motor has been used in electric vehicle propulsion. In industrial settings, this motor is commonly referred to as the brushless servo motor. The Japanese automobile companies, Honda, Toyota and Nissan, all use various forms of the brushless DC motors in their electric vehicles [3]. These motors have greater torque to size ratios than induction motors [4].

The synchronous AC motor, although less common than the brushless DC or induction motor, has also been used as a propulsion drive in recent years. Examples of vehicles using synchronous AC motors include the Nissan Hypermini EV [5] and the Ford GE ETX-II [6].

The variable reluctance and switched reluctance motors are relative newcomers to the field of electric vehicle propulsion. Although these motor types have been used in industry for many years, they were not generally considered a viable option for electric vehicle propulsion motors until the 1990s [7][4].

In recent years, permanent magnet motors have become more common in electric vehicle propulsion design, especially in experimental vehicles. Contributing factors to this trend include the availability of new rare earth permanent magnets and recent technological advances in power electronics [8]. Many of the non-permanent magnet motor topologies that were first implemented as electric vehicle drive systems during the 1960s and 1970s have been re-examined in permanent magnet form. These include the permanent magnet synchronous AC machine [9], the permanent magnet brushless DC motor [10], and the variable reluctance permanent magnet motor.

Axial flux permanent magnet machines are also receiving considerable attention in conjunction with electric vehicle propulsion. This class of machines includes motors from a wide variety of motor topologies such as reluctance motors, permanent magnet DC motors and synchronous motors [11] [8] [12] [13]. Axial flux machines utilize a rotor-stator magnetic circuit that contains an axially oriented flux path. Axial flux disc motors are often chosen for use as in-wheel drive motors because of their high torque to weight ratio. In addition, their disc shape makes them amenable to mounting inside a drive wheel rim.

Motor Winding Faults in Electric Vehicle Drives

The overall area of motor fault research is an extremely broad field and includes many sub-specialties. An incomplete list of these sub-areas might include bearing faults, induction rotor cage faults, driver faults, insulation failures, and so on. The general area of motor winding faults also encompasses a wide range of sub-fields divided by motor type, fault type and method of analysis, among other things. The research presented here is focused on motor stator winding faults in the class of permanent magnet variable reluctance motors.

The working environment of an electric vehicle propulsion motor is significantly different than that of a motor used in an industrial setting. Motor drives in electric vehicles experience high levels of vibration and turbulence due to the motion of the vehicle. This vibration is even more pronounced in in-wheel drives in which the vehicle drive motor(s) are mounted inside the hubs of the drive wheels. In such systems, the drive motors are part of the vehicle's unsprung mass and do not benefit from the vehicle's suspension system (see [14]). Electric vehicle propulsion motors are also more likely to experience impacts of various types.

There is a large body of work involving the investigation of winding faults in industrial settings [15][16]. Much of this work has been done in induction motors [18][19] [17] and large synchronous machines. There has been considerably less work done on fault detection and analysis in smaller motors such as those intended for use in electric vehicles, although there has been a marked increase in research in the last decade. In recent times motor winding faults in smaller motors such as brushless DC motors and variable reluctance motors have received more attention [20][21].

The main focus of the motor fault characterization research presented in this work is motor winding faults. These types of faults can occur in almost all electric motors. Faults due to wire insulation failure in the stator coil windings can occur in any motor that has a wound stator. This clearly includes many types of motors used in both industrial and other settings. Another type of winding fault is related to damage caused by impact. This fault may be more common in motors used in vehicles than motors used in industrial settings.

Insulation failure is a major case of stator winding faults. This type of fault is especially relevant in motors used in electric vehicles. This is partly due to the environmental factors affecting electric vehicle motors. For instance, temperatures can vary from below freezing to the high operating temperature of the motor. In addition, humidity and cold

resting temperatures such as those experienced by a vehicle parked outside in winter can result in frost accumulation inside the motor. These factors can accelerate the deterioration of coil wire insulation.

Research Objectives

The main objective of this research was to investigate stator winding faults in axial flux motors intended for use in electric vehicle propulsion systems. A key component of this research was the design and construction of an axial flux variable reluctance permanent magnet motor.

Variable reluctance motors are relative new-comers to the area of electric vehicle propulsion. Permanent magnet versions of these motors, along with permanent magnet brushless DC motors, are considered to be viable candidates for the next generation of electric vehicles. Relatively little work has been done in the area of fault diagnosis in these types of motors. This is especially true for axial flux motor topologies, which, except in a few applications, such as computer disc drives, are in the experimental development stage.

Fault characterization is a necessary step in the process of fault detection and diagnosis for a particular motor type. This research was intended to provide characterization of several types of winding faults in the specific motor topology of the axial flux variable reluctance permanent magnet motor. In addition, it was an objective of this work to produce results that have relevance to the field of fault diagnosis in the larger general class of variable reluctance permanent magnet motors.

Thesis format

This thesis is in the form of three journal manuscript papers. In addition, appendices containing mechanical drawings and electrical schematics are included.

The first paper, "Electric Vehicles and Axial Flux Permanent Magnet Motor Propulsion Systems", [Nelson and Chow, 1999] was published in the IEEE Industrial Electronics Society Newsletter. This paper serves as an introduction to axial flux motors and their experimental use as in-wheel drives for electric vehicles.

The second manuscript paper, "Development of a Motor Fault Simulation Platform for Educational and Experimental Purposes Using an Axial Flux Variable Reluctance DC Motor", [Nelson and Chow] was written for submission to IEEE Transactions on Education. This paper serves as an in-depth description of the motor used in this research. It also describes the experimental setup used to generate and collect the data for this work.

The third manuscript paper contains experimental results and analysis of coil faults. This paper, "Analysis of Rotor Velocity Damping Due to Coil Faults in an Axial Flux Variable Reluctance PM Motor," [Nelson and Chow] is intended for submission to IEEE Transactions on Energy Conversion.

The references for each paper have been compiled into one bibliography at the end of the thesis. The reference numbers in all of the papers are consistent with the reference numbers in the master bibliography.

Electric Vehicles and Axial Flux Permanent Magnet Motor Propulsion Systems

Andrew L. Nelson and Mo-Yuen Chow
Department of Electrical and Computer Engineering
North Carolina State University
Raleigh, NC 27695
USA.

I. Introduction

Overview

Recent years have shown a resurgence in electric vehicle drive research and development. This trend has been stimulated by various factors including rising fossil fuel costs and environmental concerns. New developments in basic technologies, such as improved permanent magnets, switching transistors and storage batteries (although these remain a weak point in modern electric vehicles), have contributed to recent developments in electric vehicle propulsion motors [6] [23]. Several novel motor configurations have been investigated by various groups and organizations. In addition, new technology has allowed motor types, such as variable reluctance stepping motors and brushless DC motors, previously not suitable for use in electric vehicles, to be adapted for use as electric vehicle propulsion systems.

In addition to providing a brief history of the electric vehicle, the goal of this paper is to give a short overview of recent developments in electric vehicle propulsion systems with

an emphasis on a particular class of motors, namely the variable reluctance axial flux permanent magnet motor.

A Brief History of the Electric Vehicle

The brushed DC motor has been the mainstay of EV propulsion for close to 100 years [24]. In the early part of the 20th century, both electric and fossil fuel vehicles were in development. Early electric vehicles used simple DC motors, lead-acid batteries and rheostat speed controls. Due mainly to the relatively low power densities of early electric storage batteries compared to that of fossil fuels, electric vehicles began to fall out of favor. By 1915 the rate of development of the internal combustion engine vehicle was proceeding more rapidly than that of the electric vehicle [25]. The internal combustion engine vehicle quickly outpaced the electric vehicle in power, top speed and range. By the 1920s, electric vehicle technology for small vehicles was almost completely abandoned [26].

The early 1960's saw a resurgence in electric vehicle development. Although the internal combustion engine vehicle remained almost completely dominant in the market place, several companies began developing and building prototype electric vehicles. While the brushed DC motor continued to be used in electric vehicle propulsion, this period saw the implementation of several new motor types not available to engineers in the early part of the century. Variable frequency AC induction motors have been used in prototype vehicles since the resurgence of the electric vehicle, and in production electric vehicles since the late 1980's [2]. General Motors used AC induction motors in several of its prototype electric vehicles in the 1960's. The first production line electric vehicles, the General Motors EV1 and its predecessor the Impact, both used 3-phase induction motors.

The period from the late 1980's to the present represents a second resurgence for electric vehicle development. In the last decade several major automobile companies, including General Motors, Honda, Nissan, Daimler-Chrysler and others, have offered electric

vehicles for sale as fleet vehicles and to the general public. In addition, various dedicated electric vehicle companies, such as Solar Vehicles Inc. and Green Motor Works, have appeared on the scene. Numerous companies selling electric vehicle components and gas-to-electric vehicle conversion plans have also sprung up.

Although it seems that the electric vehicle still hasn't caught the public's eye, the electric vehicle is here to stay. In recent years, large auto companies have allocated significant research and development funds to electric vehicles. For example, General Motors has invested billions of dollars in electric vehicle development in the last few years. In Europe and Asia, pure electric and hybrid electric vehicles are already on the road. The U.S. has lagged behind somewhat, with electric vehicles from the big auto companies only available for lease or as fleet vehicles in a few states including California, Arizona and New York [27]. At the time of the writing of this article, both Toyota and Honda have electric vehicles in production. These vehicles will be shipped to dealers in the U.S. in December 1999 and January 2000, and will be for sale to the general public. Figure 2-1 shows the Honda EV Plus, now available through dealers nation wide in the US.



Figure 2-1. The Honda EV Plus.

New and Emerging Electric Vehicle Propulsion Systems

In recent years many new motor topologies have been proposed for use in electric vehicles. Some of these new motor types have been used in production electric vehicles while others remain in the prototype and development stages. As mentioned above, the variable phase induction motor has been used since the 1960's and continues to be the motor of choice for the major electric vehicle developers (GM, Ford and Daimler-Chrysler) in the U.S. market [3]. In the last ten years several other motor types have been researched and/or used for electric vehicle propulsion. These include the permanent magnet synchronous AC machine, the brushless DC motor, and the variable reluctance motor. In contrast, the Japanese companies, Honda, Toyota and Nissan, all use brushless DC motors in their electric vehicles. EMB Inc. has recently offered a line of electric motorcycles, which utilize variable reluctance brushless DC motor drive systems. In addition, implementation of electric vehicle drives based on several more esoteric motor topologies, such as the hybrid induction motor and the permanent magnet hysteresis hybrid synchronous motor, have been proposed.

One interesting and promising new motor topology is the axial flux permanent magnet DC machine [12]. A particular configuration of this class of motors, the axial flux variable reluctance permanent magnet disc motor, will be considered in more detail in the next section of this paper.

II. The Axial Flux Variable Reluctance Permanent Magnet Disc Motor

A General Overview of Variable Reluctance Motor Function and Structure

The basic means of torque development in a variable reluctance motor is magnetic attraction between electromagnetic coils, usually on the stator, and iron or permanent magnets on the rotor. When a stator coil is excited with electric current, magnetic flux is

induced. The induced flux flows through the core of the excited coil, across the stator-rotor air gap, and through one or more static flux paths on the rotor, thus producing magnetic attraction between the stator and the rotor. As the rotor turns, the air-gap portion of the flux path changes, thus the name "variable reluctance".

One can also describe force development in variable reluctance motors in terms of the law of conservation of energy. In a magnetic system, a force will be generated that tends to reduce the reluctance of any flux path to a minimum. When a flux producing coil is excited, a directed force is generated that tends to move the rotor to a position that minimizes the variable part of the flux path (in this case, the air gap), thus causing rotational torque (depending on the initial position of the rotor). Figure 2-2 shows a typical 3-phase six stator coil four rotor pole variable reluctance motor layout.

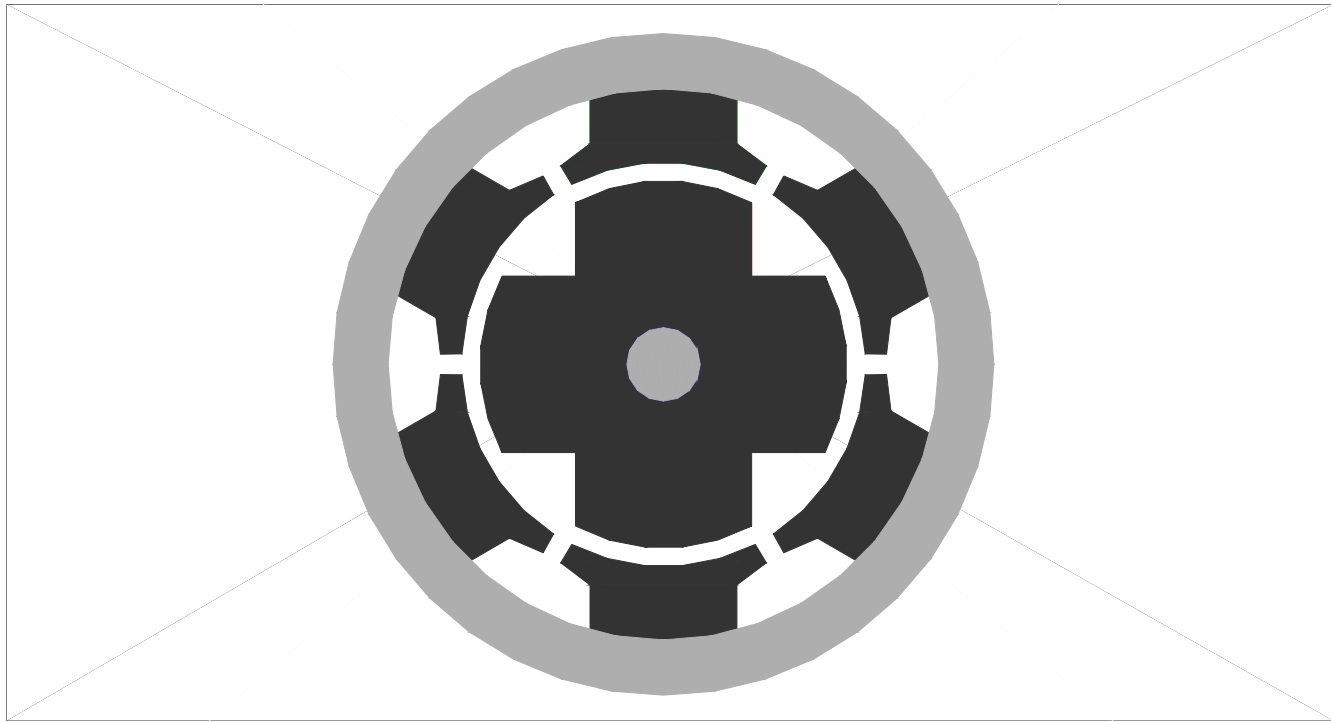


Figure 2-2. Cross sectional view of a six coil four pole variable reluctance motor.

A Specific Motor Topology

For purposes of illustration and explanation, we will consider a particular motor configuration, the axial flux variable reluctance permanent magnet disc motor, in more detail. For the remainder of this article, the term *axial flux disc motor* will be used to refer to this particular class of motors. The reader should note that in the broader context of motor design, the term *axial flux disc motor* describes a much larger class of motors, including various types of brushless DC and synchronous motors.

The motor described below has been prototyped for purposes of demonstration and control research in the Advanced Diagnosis and Control (ADAC) lab at North Carolina State University, and is shown in Figure 2-3. This motor has four permanent magnet rotor poles and seven stator phases. Each stator phase consists of two coils to make a total of 14 stator poles.

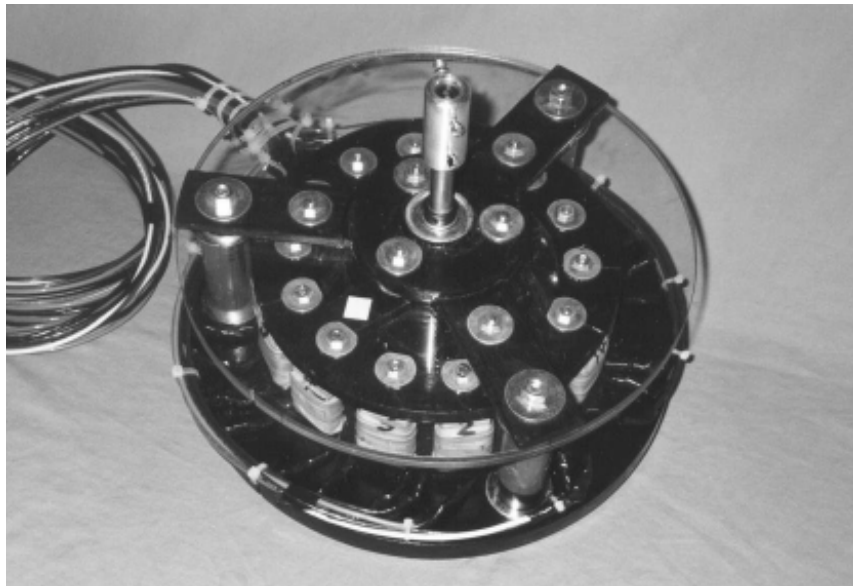


Figure 2-3. The ADAC axial flux disc motor.

The motor has wound coils on the stator and permanent magnets on the rotor. In this motor design, the phrase "Axial Flux" indicates that the stator coils and rotor poles are

arranged so that the magnetic flux paths have components that are parallel to the axis of the rotor. The rotor is a disc with permanent magnets set into the edge of the disc so that each pole of every magnet is oriented toward one or the other face of the disc. Similarly, the stator coils are arranged to induce north and south poles oriented axially as to attract (or repel) a pair of rotor poles. Note that the term "pole" actually refers to a set of north and south poles from a single permanent magnet.

Figure 2-4 shows a schematic representation of the axial flux disc motor described above. Note that the rotor 'disc' in this case has a relatively small radius. Motors of this type can be made to have much wider disc rotors (resulting in higher torque) without significantly increasing overall motor weight. Two stator coils and two rotor permanent magnets have been shaded in Figure 2-4 to emphasize the torque generation relationship between the stator and the rotor.

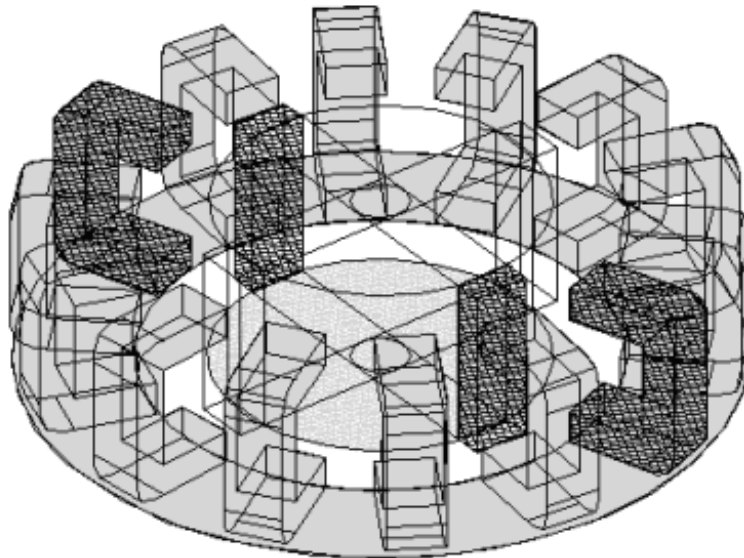


Figure 2-4. Drawing of the axial flux disc motor.

Unlike traditional variable reluctance motor arrangements, it should be emphasized that magnetic flux does not flow through the center of the rotor, nor does it flow

circumferentially around the stator during motor operation. Flux generated by a stator coil flows axially through the stator coil core, then radially across the (upper) air gap, then axially through one or more rotor permanent magnets, and then back across the (lower) air gap to the originating stator coil. Motors of this configuration exhibit a high degree of flux path isolation. There is no low reluctance (iron) path between neighboring stator coils.

Modes of Operation

Motors of the configuration described above can be operated in several modes, including as a stepping motor, as a brushless DC motor (in conjunction with a rotor position sensor), and as a synchronous AC motor.

To operate this type of motor as a stepping motor, the stator coils are switched on and off in a set pattern that causes the rotor to "step" forward as the switching pattern proceeds.

Operation as a brushless DC motor requires the addition of a rotor position sensor. Often, Hall effect sensors are used for this purpose. Using position information from the sensor(s), the motor can be electronically commutated and driven as a DC motor via power switching devices such as MOSFETs [10].

To drive the motor as an AC motor, each coil must be fed with a differentially phased sinusoidal current. The number of coil sets per rotor pole determines the required number of current phases.

Advantages and Disadvantages of the Axial Flux Disc Motor

Compared to traditional motor configurations, axial flux disc motors have very short iron flux paths. Minimizing the iron flux path length results in a reduction in core losses (hysteresis and eddy current losses). No eddy current losses within a permanent magnet are associated with flux generated by that permanent magnet. Thus the use of permanent

magnets in the rotor also contributes to a reduction in flux path related losses. In addition, because permanent magnets produce magnetic flux, the torque to weight ratio of a permanent magnet rotor motor is higher than that of its iron rotor counterpart. Flux does not flow radially through the rotor, so the iron used in traditional rotor flux paths can be eliminated altogether. This motor configuration also provides for flux path isolation, which significantly reduces coil to coil induced inductance and associated losses. This flux path isolation structure also allows for a large degree of freedom in the choice of control strategy. Because of its light weight and high efficiency, this type of motor lends itself to use in electric vehicles, mobile electric equipment of various types, and many other applications.

The axial flux disc motor requires a more sophisticated control strategy than that of the brushed DC motor. A rotor position sensor is required in order to achieve efficient high speed control. This type of motor generally requires micro-processor based control for efficient power utilization. Also, since the stator contains many distinct core units and axially oriented windings, manufacturing complexity is increased.

III. Multi-Motor and Direct Wheel Drive Systems in Electric Vehicles

General Description

Direct wheel drive systems consist of a motor drive coupled directly to a driven wheel without any intervening gear or suspension linkage. As a result, there is a direct one to one correspondence between the rotation of the motor drive and that of the driven wheel. This arrangement simplifies the drive train considerably but alters the suspension characteristics of the vehicle. In a conventional drive system (electric or internal combustion), the only unsprung mass in the vehicle are the wheels and a small portion of the drive train. Generally, the drive motor(s) in a direct wheel drive system are part of

the vehicle's unsprung mass. Most electric motors and all internal combustion engines are too heavy to be removed from the body of the vehicle and incorporated into one or more of the drive wheels. In order for an electric motor to be suitable for use in a direct wheel drive system, it must have a relatively low mass and a high torque to mass ratio. In addition, direct wheel drive motors must have physical dimensions that are amenable to location near or in a drive wheel. Because of these constraints, various configurations of brushless permanent magnet DC motors and permanent magnet variable reluctance motors have been shown to be good candidates for direct wheel drive systems. The axial flux disc configuration allows for the incorporation of the motor directly into the hub of a driven wheel [12].

In the 1990's new technologies, such as the development of powerful rare earth permanent magnets and advances in power switching electronics, have made the production of light weight high torque motors feasible [12].

Some Examples of Direct Wheel Drive Systems in Electric Vehicles

Recent years have seen the development of numerous direct wheel drive prototype vehicles. One of the earlier (1994) examples of a functional direct wheel drive electric vehicle was the Di-Elettrica [22], a motor scooter with a direct drive rear wheel. The Di-Elettrica was powered by a slotless axial flux permanent magnet DC motor with a single disc shaped stator sandwiched between two permanent magnet disc rotors. The motor was mounted inside the rim of the scooter's drive wheel.

Eastham and Gair et al. describe a motor arrangement in which the stator of a permanent magnet disc motor is attached to the sprung body of the vehicle, while the rotor is attached to the unsprung drive wheel shaft [14]. This arrangement further reduces the unsprung mass of the vehicle, but requires a relatively complicated and dynamic control strategy to accommodate motor torque fluctuations due to constant and variable rotor-stator misalignment associated with vehicle suspension movement.

Motors have been specially designed for direct in-wheel use. Chen and Tseng and others describe permanent magnet motors designed and optimized for placement in the hub of an electric vehicle drive wheel [28].

The Four Direct Wheel Drive Electric Vehicle

One of the most promising direct wheel drive configurations for electric vehicles is the four in-wheel drive electric vehicle [29]. Figure 2-5 shows a four direct wheel drive electric vehicle arrangement. Incorporating a motor in each wheel increases the number of drive motors in the vehicle, thus decreasing the required power and mass of each individual drive motor. Four in-wheel drive vehicles require a distributed control system that can deliver the appropriate control to each individual drive motor. Although this may at first seem like a drawback, it should be noted that conventional four wheel drive systems also require a relatively complex control system to regulate the performance of the drive train. In addition, a modern conventional four wheel drive train and transmission system is quite complex mechanically and very expensive to manufacture. The complexity required to implement control in an electric four in-wheel drive system can be reduced to programming a micro-controller chip.

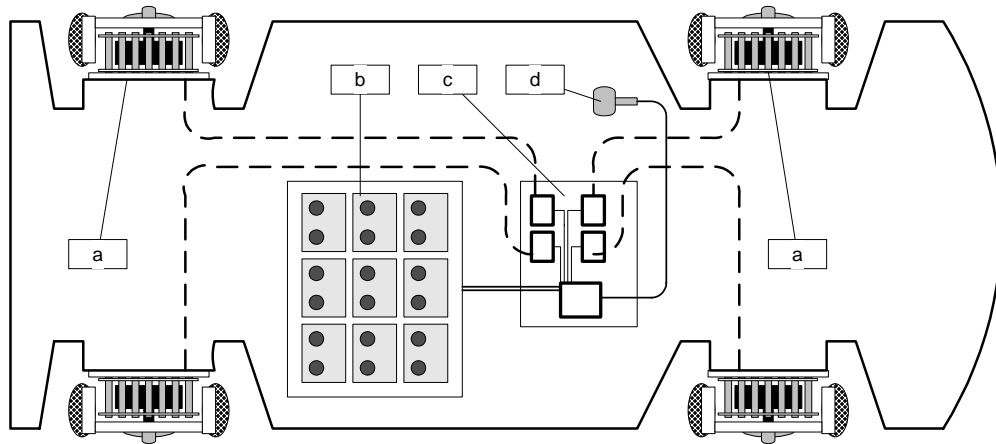


Figure 2-5. A four direct wheel drive arrangement showing motor and controller locations. (a) Each wheel has a disc motor mounted inside its hub. (b) Battery pack. (c) System controller. (d) Accelerator pedal.

IV. Closing Remarks

Challenges and opportunities for the future

The field of electric motor fault detection has generally received attention in the context of industrial applications. The working environment of electric motors used for electric vehicle drive applications is significantly different than that seen by typical industrial motors. In the coming era of hybrid electric, fuel cell electric, and pure electric vehicles, the field of motor fault detection in the context of electric vehicles will receive much greater attention.

Direct in-wheel drive systems offer opportunities for the development and implementation of dynamic fault detection and accommodation systems [18]. Multi-motor drive systems will require the continued development and application of distributed control technology.

New application specific motor topologies will continue to be developed. The line between motor design and motor control is becoming less distinct. As computer and power electronics technologies continue to advance, motor designs that take advantage of new control options are becoming more common. This blending of mechanical electrical design and control technology will offer new opportunities for motor designers, technology experts and control theorists to work together to develop more robust and efficient electric vehicle drive systems.

Acknowledgments

The authors of this article would like to acknowledge the support of the National Science Foundation grants ECS-9521609 and ECS-9610509 which helped make the work at the ADAC lab possible.

References

See Thesis Bibliography.

Development of a Motor Fault Simulation Platform for Educational and Experimental Purposes Using an Axial Flux Variable Reluctance DC Motor.

Andrew L. Nelson and Mo-Yuen Chow
Department of Electrical and Computer Engineering
North Carolina State University
Raleigh, NC 27695
USA.

Abstract

This paper describes a motor fault simulation platform built around a prototype axial flux variable reluctance motor. The motor is useful for both demonstration of motor principles and for research purposes. The motor was prototyped in the Advanced Diagnosis and Control (ADAC) laboratory at North Carolina State University. The motor platform has been used as a basis for graduate and undergraduate projects. In addition, the prototype motor has been used as a model system for graduate control systems classes. The motor has a relatively exposed architecture. Each stator coil can be identified without disassembling the motor. Much of the structure of the motor, including the rotor, is visible when the motor is fully assembled. This is useful for demonstration and teaching purposes because it allows students to see the interaction of the various motor components while the motor is in operation. The motor was also designed to facilitate the demonstration and study of various motor faults. To this end, one of the motor's stator phases was equipped with fault simulation coils. The motor is connected to an array of voltage, current, and position sensors. Data from these sensors can be collected and stored on a computer. In addition, the motor can be controlled with a computer linked to the internet. This allows for its use in network based control studies. Students

can learn about motor control theory, fault detection and diagnosis more effectively by combining theory learned in the classroom, simulations obtained from computers, and actual measurements from a physical motor system.

I. Introduction

Demonstration of physical properties and interactions are important in the educational process. Many introductory engineering courses use physical devices and apparatus to demonstrate fundamental principles. In contrast, advanced courses often rely solely on mathematics and computer simulation. Modeling and control courses are typically taught at the senior undergraduate or graduate level. A favorite subject for electrical engineering control and modeling courses is the electric motor. The motor platform described here represents a dynamic system that can be used in such courses as a subject for modeling, simulation and control. Using a physical system in conjunction with computer simulation and theory can help to motivate students, and to tie theory to application.

The focus of this paper is the description of a prototype motor and a motor fault simulation platform constructed for educational and research purposes. The motor used is an axial flux variable reluctance permanent magnet (VRPM) motor. This class of motors has received increasing amounts of attention in recent years as a candidate for use in applications requiring motors with a high torque to size ratio. These applications include use in electric vehicle propulsion systems and in mobile equipment applications [30][7]. In addition, variable reluctance motors are well suited for high technology aerospace and medical applications. This is because these motors can be designed to operate at very high speeds, and they possess a degree of inherent fault tolerance.

The motor described in this paper is similar in topology to experimental in-wheel drive motors for electric vehicles. Several such motors are described in the literature. For example, an axial flux permanent magnet brushless DC motor designed to be mounted directly on the drive wheel hub of a solar-electric vehicle is described in [31]. Additionally, [22] describes a variable reluctance axial flux disc motor with two outer rotors designed for mounting inside the rear wheel of an electric motor scooter.

Although the specific motor discussed in this work is designed with a somewhat unconventional topology (i.e. physical arrangement), its fundamental method of torque generation is the same as that in standard variable reluctance permanent magnet motors. As such, it is useful as a demonstration tool for variable reluctance motor operating principles. In addition, when the motor is driven with a brushless DC driver strategy, it displays some of the operating characteristics of a conventional brushless DC motor. The motor described here has been designed with a relatively exposed architecture compared to other motor types. This makes it well suited for educational purposes because it can more readily demonstrate the motor operation principals. The front face of the motor is made of a transparent material, allowing the rotor and the interior of the stator to be viewed. Also, the stator phases are numbered and their wiring is color coded so that their interconnections can be traced.

Sections II, III, IV and V of this paper describe in detail, the design of the prototype motor, the system dynamical equations, the motor driver, and the motor fault simulation platform, respectively. Throughout the paper, an effort has been made to highlight aspects of the motor and platform design that make it useful as an educational tool. Section VI provides brief descriptions of several of the education related applications of this motor platform.

II. Motor Physical Description

Before delving into the particular topology of the motor described in this work, it will be beneficial to briefly discuss variable reluctance motors in general. In earlier decades, many types of variable reluctance motors would have been classified as stepping motors or as synchronous AC motors [32][10][33]. In recent years, due to advances in permanent magnet technology and in solid state power electronics, many new types of variable reluctance motors have appeared [34][7][35]. These are often intended for use in applications in which a DC or universal motor would have been used in the past. Examples include a high output variable reluctance PM motor suitable for use in robotics applications[36], and a switched reluctance machine for use in aircraft control actuators[37].

Variable reluctance permanent magnet motors are sometimes designed with unconventional geometries to facilitate their use in special applications [11][38] [39]. Unlike standard induction or synchronous motors, VRPM are often built with a high degree of electrical and magnetic flux path isolation between the phases. Motors designed with flux path isolation lend themselves to unconventional topologies more than traditional motor types, because there is relatively little interaction between the different phases [40]. This allows for greater freedom in stator coil shape, and in the number of stator coils used.

The motor described in this section is an axial flux variable reluctance permanent magnet disc motor with 14 stator coils and 4 pairs of rotor PM poles. This motor was prototyped in the Advanced Diagnosis and Control (ADAC) laboratory at North Carolina State University. The prototype motor is shown in Figure 3-1. A top view diagram of the stator coil and rotor pole arrangement of the motor is shown in Figure 3-2. In this motor design, the phrase "axial flux" indicates that the stator coils and rotor pole pairs are arranged so that the magnetic flux paths have components that are parallel to the axis of

the rotor. This will be discussed in greater detail following a description of the stator and rotor designs.

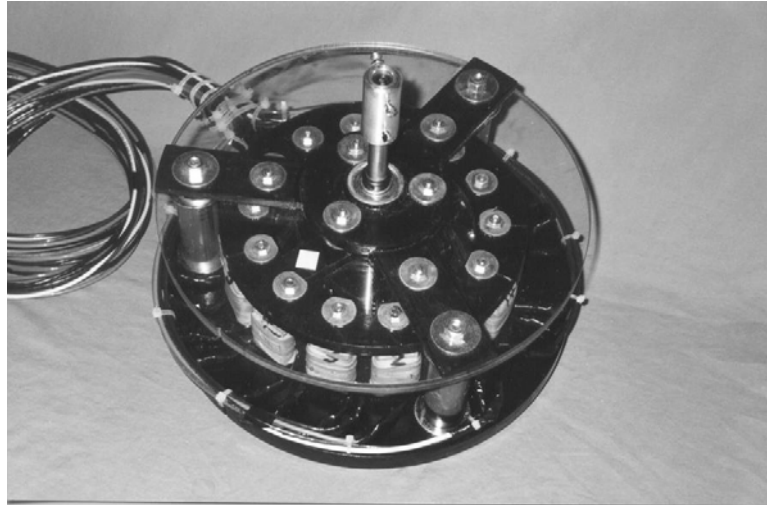


Figure 3-1. The axial flux variable reluctance DC motor.

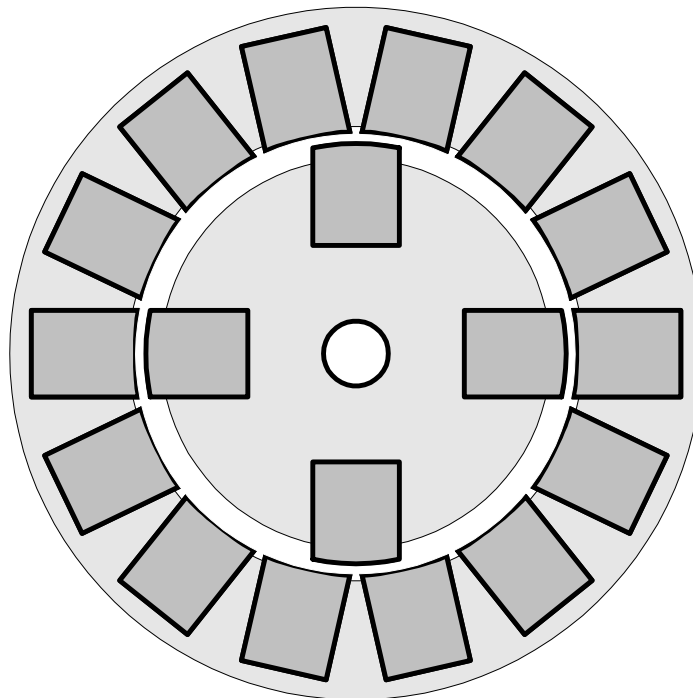


Figure 3-2. Top view of the prototype motor showing the relative locations of the rotor poles and the stator coils

The motor is designed with 7 stator phases. Each stator phase consists of two coils making a total of 14 stator coils. The stator coils are wound on separate laminated cold rolled steel cores, which are attached to a non-conducting substrate. Each stator coil is isolated from the others both electrically and magnetically. The only iron in the stator is contained in the coil cores. The remainder of the stator is made up of non-conductive material, and serves a structural roll only. These cores also serve as flux paths to direct the magnetic flux and the resulting mmf (magneto-motive force) from the coils to the rotor. Each core has two machined surfaces that make up the stator side of the air gap. Figure 3-3 shows the stator cores during the assembly of the motor.

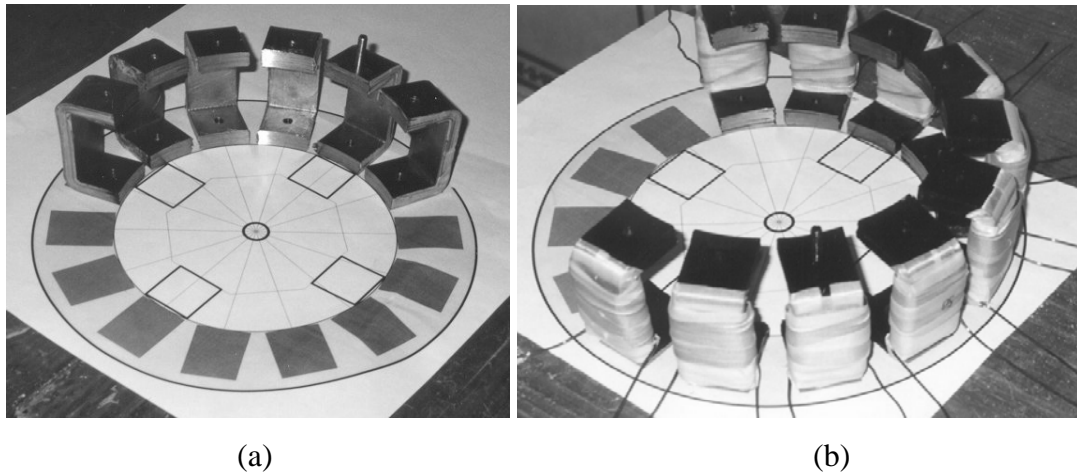


Figure 3-3. Prototype motor stator coil cores.(a) Laminated cores before winding. (b) Laminated cores after winding.

The rotor is a disc with permanent magnets imbedded close to the edge of the disc, so that each pole of every magnet is oriented toward one or the other face of the disc. The term “pole pair” refers to a set of north and south poles from a single permanent magnet. As with the stator coils, the rotor pole pairs are magnetically isolated from one another. In this type of motor, flux does not pass through the center of the rotor, and the majority of the material making up the rotor is not conductive to magnetic flux. The rotor side of the

air gap is made up of short iron flux paths that direct magnetic flux to/from the individual permanent magnet pieces.

We will now discuss the overall topology of the motor. The arrangement of the 4 PM pieces in the rotor produces 4 axially oriented pole pairs spaced at 90 degree intervals. Likewise, the stator coils are arranged to induce north and south poles oriented axially as to attract (or repel) a pair of rotor poles when energized. Because the motor is designed to operate with unidirectional coil current and unidirectional flux generation, it is desirable to maximize the distance between consecutively firing stator coils, while minimizing the step size that the rotor must cover for each commutation segment. The traditional three phase 6:4 configuration is well suited for small motors with bi-directional flux generation, and in which coils are energized in a positive-negative-off sequence. These motors are generally designed so that the rotor travels half the radial distance between two consecutive stator coils during each commutation sector. The 7 phase 14:4 arrangement allows for the same half step commutation scheme, but introduces an extra stator pole between each consecutively firing stator coil. Many rotor pole stator coil configurations are possible. The 14:4 is the second smallest possible arrangement that allows for half stepping with a four pole rotor. Increasing the number of coils per phase allows for a greater overall motor radius, and produces a greater torque lever arm associated with force generation during stator coil-rotor pole interaction. Figure 3-4 shows a three dimensional depiction of the stator coil and rotor pole relative locations. In this figure, two stator coils and two rotor PM pole pairs are highlighted to emphasize their interaction during torque generation.

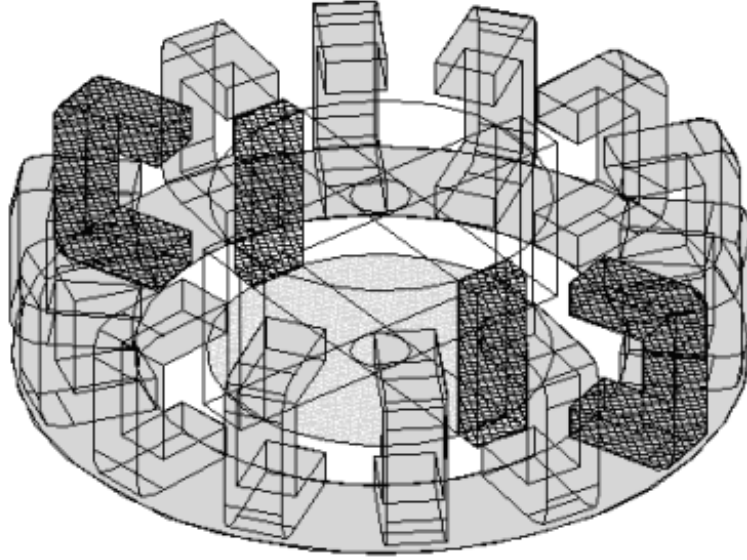


Figure 3-4. Three dimensional motor view highlighting the interaction between two rotor pole sets and two stator coils.

III. Mathematical Model

In this section, mathematical equations describing the dynamical behavior of a generalized axial flux variable reluctance motor with M stator coils and P permanent magnet rotor pole pairs will be presented. The dynamical equations presented in this section are similar to standard variable reluctance motor equations found in the literature [38][30][41]. It should be noted that variable reluctance and switch reluctance motor dynamics are generally nonlinear, and therefore the standard linear DC motor equations are not directly applicable to the prototype motor described in this work.

The voltage for a particular stator coil is given by equation (eq1) as follows

$$v_m = R_m i_m + L_m \frac{di_m}{dt} + e_m, \quad m = 1, \dots, M \quad (\text{eq1})$$

where v_m is the source voltage applied over the m th stator coil, R_m is the resistance of the m th coil, L_m is the self inductance of the m th coil, and e_m is the induced voltage in the m th coil due to the rotation of the permanent magnet rotor (i.e. 'induced back emf'). As indicated in the previous section, variable reluctance motors of the type described in this paper possess a high degree of electrical and magnetic isolation between the phases. There is no direct iron flux path between the various stator coils, and hence the mutual inductance is considered to be negligible [38]. L_m is a function of rotor position, θ , while e_m is a function of both rotor position and rotor velocity, ω . For modeling purposes, L_m and e_m are often approximated by piecewise linear curves [42][43]. In the case of e_m , the piecewise linear curve would be scaled by a term proportional to ω .

For purposes of analysis, it will be convenient to express $L_m(\theta)$ in the following form

$$L_m(\theta) = Nk_L l_m(\theta) \quad (\text{eq2})$$

where N , k_L , and $l(\theta)$ are the number of turns per coil, a constant representing the static elements of the flux path, and a unit function representing the variable part of the flux path, respectively. The partial derivative of $l_m(\theta)$ with respect to θ will be used later in the motor torque equation. This is also approximated by a piecewise linear curve. Figure 3-5 shows idealized wave forms used to approximate the unit wave form inductance seen by a single phase, $l_m(\theta)$, and its partial derivative with respect to θ . The shaded portion of Figure 3-5 indicates the phase sector of the stator phase corresponding to the wave forms shown (phase 1).

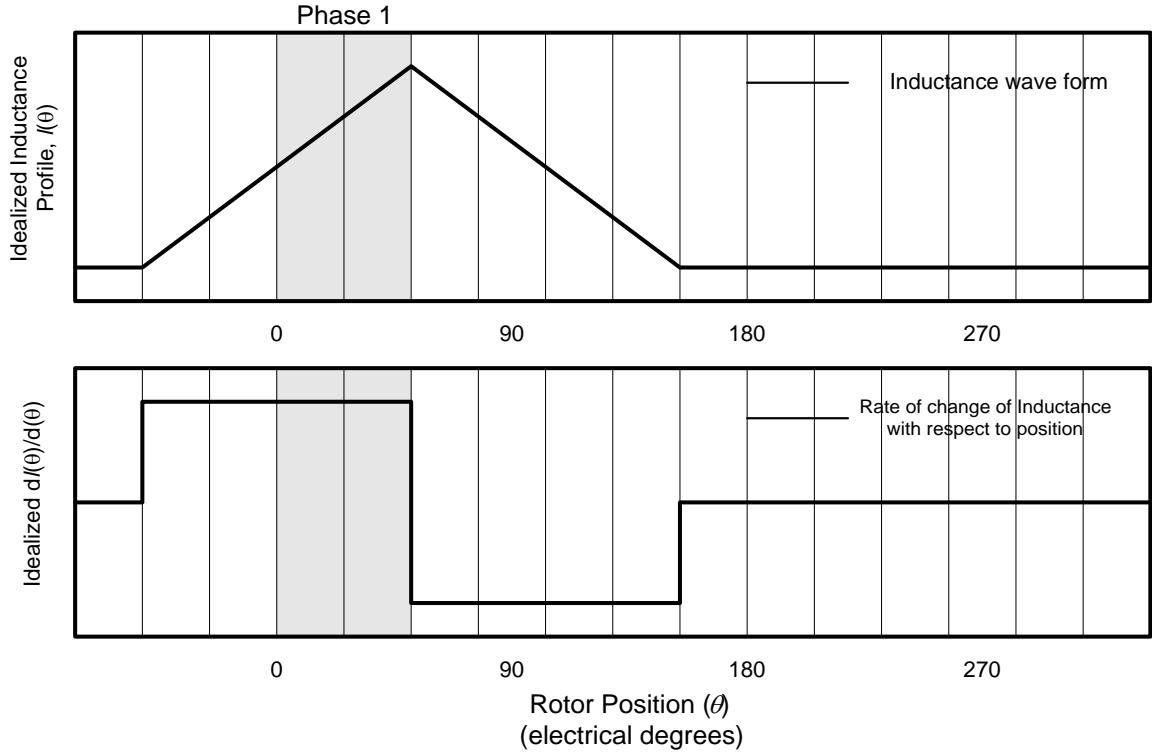


Figure 3-5. The idealized unit piecewise linear wave forms, $l_m(\theta)$, and its partial $d l_m(\theta)/d\theta$ with respect to θ . These curves are shown for 360 electrical degrees.

The $k_L(\theta)$ term in equation (eq2) accounts for deviations from the idealized wave form as well as constant factors due to the static parts of the flux path. This term is generally derived from experimental data and is particular to each specific motor topology. This paper is not primarily focused on modeling. As such, the idealized wave forms shown in Figure 3-5 will be sufficient for the later analyses in this work.

The motor is considered to operate under non-saturating flux conditions. In this case, the inductance, L_m , is a function of rotor position only. Then the flux linkage in the m th coil is given by

$$\phi_m = L_m(\theta)i_m \quad (\text{eq3})$$

In the formulation of state space equations, it will be convenient to solve (eq3) for i_m to give

$$i_m = \frac{\phi_m}{L_m(\theta)} \quad (\text{eq4})$$

The net electrical torque applied to the rotor by a given stator coil can be written as [44]

$$T_m = \frac{1}{2}(i_m)^2 \frac{\partial L_m(\theta)}{\partial \theta} \quad (\text{eq5})$$

The total torque is then given by the sum of the torques due to each of the stator coils:

$$T_e = \sum_{m=1}^M T_m \quad (\text{eq6})$$

The motor mechanical dynamics are described by the sum of the various mechanical loads on the rotor. This is given by

$$T_e = J \frac{d\omega}{dt} + B\omega + T_l \quad (\text{eq7})$$

In the torque equations, T_e is the electrical torque on the rotor, J is the moment of inertia of the system, B is the damping coefficient, and T_l is the load torque.

Finally, from basic physics, the angular velocity and position are related by

$$\omega = \frac{d\theta}{dt} \quad (\text{eq8})$$

To formulate the state space equations for this model, we will select

$$\phi_1, \phi_2 \dots \phi_m$$

ω , and

θ

as the state variables and

$$v_1, v_2 \dots v_m$$

as the inputs.

Substituting (eq4) into equation (eq1), and then solving for $d\phi_m/dt$ gives m state equations of the form

$$\dot{\phi}_m = v_m - R_m \frac{\phi_m}{L_m(\theta)} - e_m \quad (\text{eq9})$$

Equating (eq6) and (eq7) gives

$$T_e = \sum_{m=1}^M T_m = J \frac{d\omega}{dt} + B\omega + T_l \quad (\text{eq10})$$

Solving equation (eq10) for $d\omega/dt$ we get

$$\dot{\omega} = \frac{1}{J}(T_e - B\omega - T_l) \quad (\text{eq11})$$

and equation (eq8) gives our last state equation.

$$\dot{\theta} = \omega \quad (\text{eq12})$$

IV. Motor Driver Strategies

Driver types

Motor driver strategy is an important component in overall motor design. Classification of motors takes into account the manner in which the motor is driven, as well as the motor's physical arrangement. For example, a variable reluctance motor might be called a synchronous motor if it is driven with phased sinusoidal AC power. On the other hand, the same motor might be called a variable reluctance stepping motor if it is driven with phased square wave power in an open loop configuration [10]. The motor described in this paper is suited for several driver control strategies. These drivers include stepping, synchronous AC, and brushless DC. We will focus on two of these. Firstly, a computer based stepping motor driver configuration will be discussed. In addition, a brushless DC motor driver strategy will be described. The computer implemented stepping motor driver is useful to students for hands on demonstration of fundamental motor and control concepts. The brushless DC motor driver is more complex and is similar to drivers that might actually be employed in electric vehicle propulsion applications.

Stepping Motor Driver

The first driver arrangement, the stepping motor strategy, involves delivering phased square wave voltage pulses to the stator phases. The pulses are delivered in a repeating sequence that causes the rotor to increment its position, or 'step', with each pulse. Figure 3-6 shows the voltage wave forms that are delivered the motor stator phases for a half-

stepping sequence. In this case, the phased pulses are delivered with respect to time and are independent of rotor position. The speed of the rotor is regulated by changing the frequency of the pulses. This strategy is an open loop control system. If the rotor stalls, the switching sequence will continue, causing the rotor to fall out of step with the sequence.

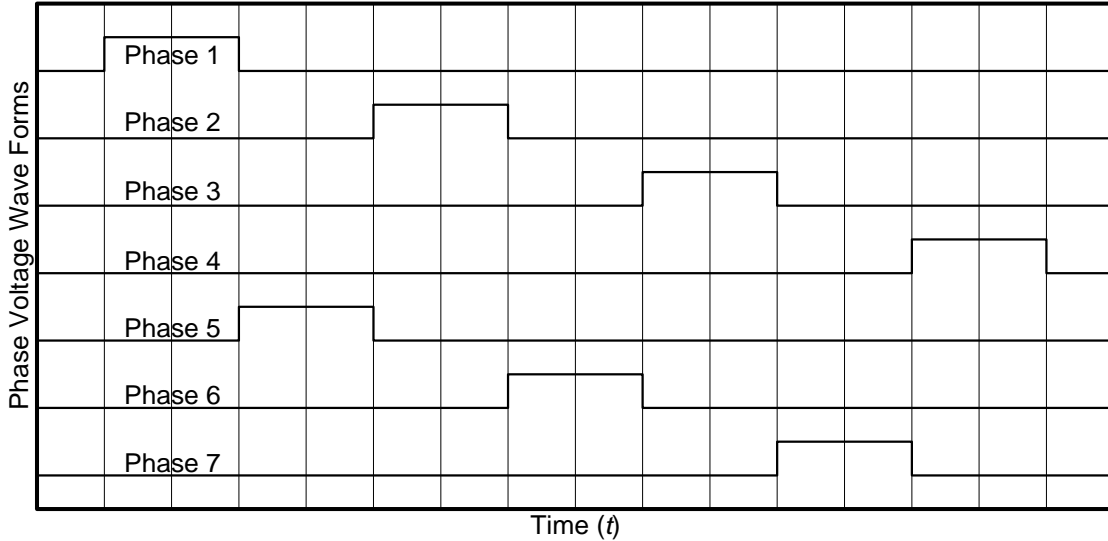


Figure 3-6. Time-voltage wave forms supplied to each of the stator phases to implement the half stepping open loop sequence driver scheme.

The behavior of this type of open loop driver configuration under load conditions can be understood by considering the voltage and torque equations given in the mathematical modeling section. Let us consider the torque generation due to phase #1 when it is energized. In this case equation (eq1) can be written as

$$v_1(t) = R_1 i_1 + L_1(\theta) \frac{di_1}{dt} + e_1 \quad (\text{eq13})$$

Equation (eq13) indicates that when $v_1(t)$ is non-zero, a current will result. At low speeds, the last two terms become negligible. In this case, we see that a current will flow in the phase coils when $v_m = v_{source}$, regardless of rotor position. The current profile can

be found by solving the motor dynamic equations, or by experiment for non static conditions. When v_m is zero, i.e. when the coil is not energized, i_m is also zero because there is no longer a closed path for current flow. Torque generation, on the other hand, is dependant on rotor position. Equation (eq5) indicates that torque generation in the m th phase is dependant on the rate of change of inductance in the m th phase with respect to rotor position. In the case of the open loop stepping driver, only one phase is energized at a time. This can be seen from the phase input voltages shown in Figure 3-6. When phase one is energized, the total electrical torque given in equation (eq6) becomes

$$\begin{aligned}
 T_e &= \sum_{m=1}^M T_m \\
 &= \sum_{m=1}^M \frac{1}{2} (i_m)^2 \frac{\partial L_m(\theta)}{\partial \theta} \\
 &= \frac{1}{2} (i_1)^2 \frac{\partial L_1(\theta)}{\partial \theta}
 \end{aligned} \tag{eq14}$$

since $i_m = 0$ for each phase except in the case of phase 1. Now it is clear from equation (eq14) that torque generation is dependant on the rate of change of inductance in the energized phase. From Figure 3-5 it can be seen that this value is zero for some positions. These positions are referred to as dead zones. Note that a dead zone for one stator phase is not necessarily a dead zone for another phase. If the rotor is loaded so that it lags the stator stepping sequence to the degree that it can fall into a dead zone for which ever coil is currently being energized, the rotor will stall.

As a demonstration of computer control, a stepping motor driver for the axial flux variable reluctance motor was implemented on a PC. A National Instruments SCXI chassis with several I/O modules, and a PCI board were used to interface the motor to the computer. The driver was written using G-code, a graphical programming language developed by National Instruments for use with LabVIEW. The SCXI-1161 power relay array module was used to switch power to the stator phases. The motor was powered by a Tektronix PS280 fixed 5 volt supply. A diagram showing the arrangement of these components is shown in Figure 3-7.

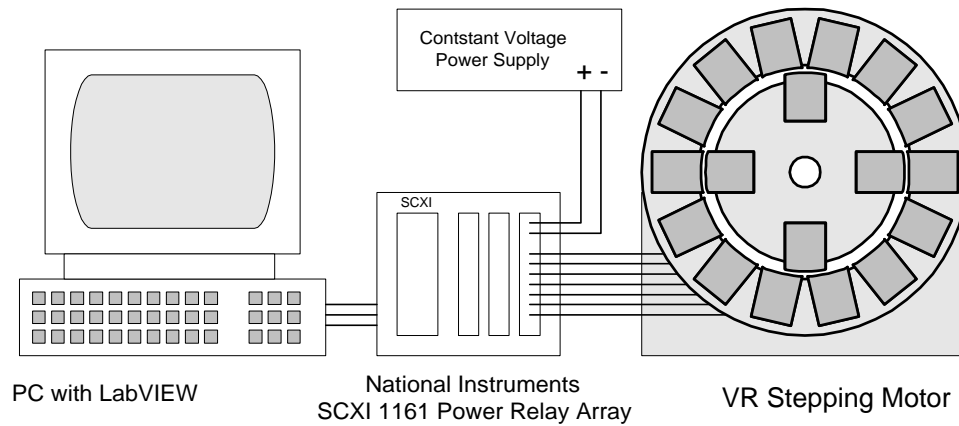


Figure 3-7. Diagram showing the interconnections between the computer, motor, power switching relay array, and power supply in the open loop stepping control.

The computer implementation of the stepping motor driver allows students to change the driver configuration and directly see the effects on motor performance. For instance, students can experiment with different stepping sequences to see how these affect stability and rotor speed. In addition to allowing students to experiment with stepping sequences and rates, the computer interface also allows students to energize the phases individually. This lets students explore motor operation principles in a very direct fashion. Figure 3-8 shows a computer screen interface for the stepping motor driver. The speed of the stepping sequence can be adjusted via a dial control on the left. The phase sequence is reported via the graphic on the right.

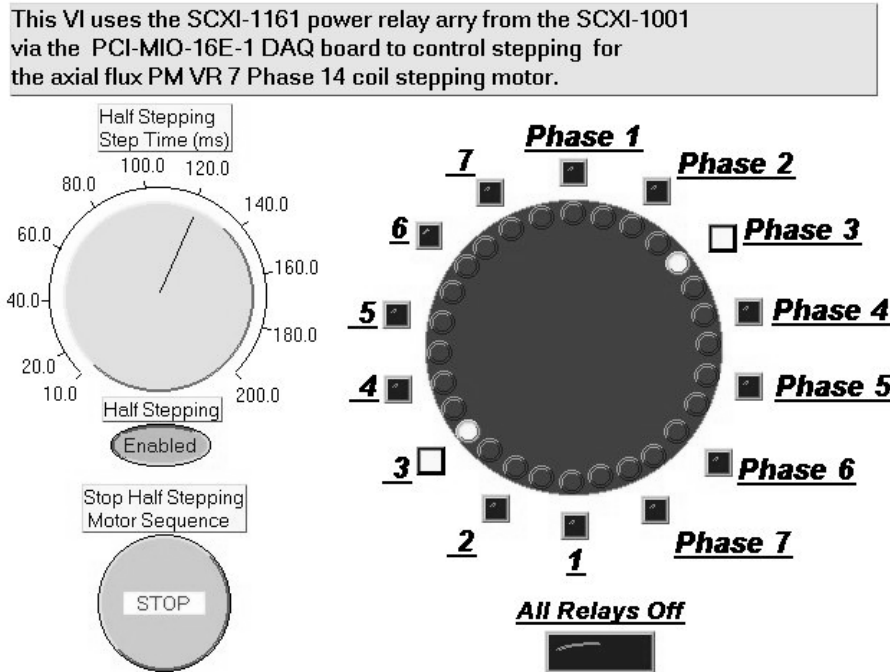


Figure 3-8. Graphic user interface for the PC implemented stepping motor driver.

Brushless Motor Driver

A second driver was developed to drive the motor as a brushless DC motor. Brushless DC motors use rotor position sensors to coordinate power switching to the stator phases. The rotor position sensors produce signals that allow the driver to electronically commutate the motor phases. The actual phase switching is generally done by solid state power switching transistors. Brushless DC motors often use Hall effect sensors or optical encoders to determine rotor position.

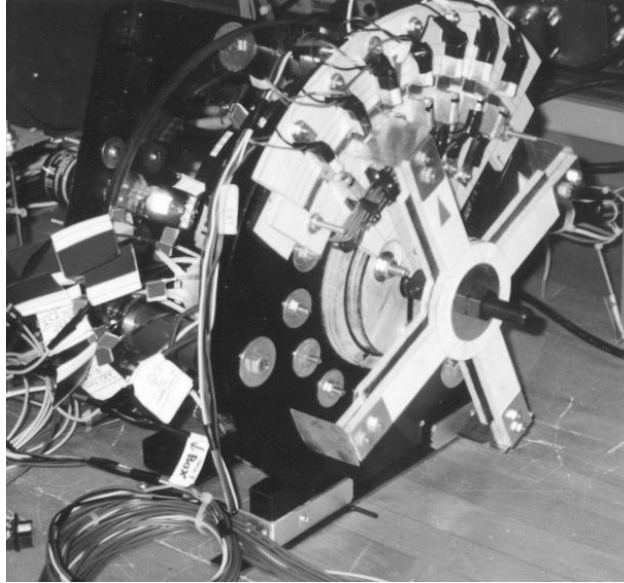


Figure 3-9. Photograph of electronic commutator installed on the prototype motor.

To implement a brushless DC motor driver on the prototype axial flux variable reluctance motor, an infrared optical electronic phase sector position detector was constructed. To make the system more useful as a demonstration tool, the position detector was constructed so that its functional elements could be viewed while the motor is in operation. Figure 3-9 shows the position detector installed on the prototype motor. The position sensor sends signals to a steering circuit. The steering circuit in turn produces logic output signals that drive an array of solid state power transistors. In conjunction with the power transistor relays, the phase sector position detector electronically commutates the motor phases. The entire brushless DC motor driver is laid out so that the components of the system and their interconnections can be physically identified and more easily understood.

In the case of the brushless driver scheme, the voltage waveforms delivered to the stator phases are functions of rotor position. In this case it is possible to deliver voltage waveforms to each stator phase in a manner that coincides with a region of the inductance profile that is associated with a non-zero rate of change for that phase. Figure 3-10

shows ideal voltage and inductance wave forms in the case of the brushless driver scheme. Both voltage and inductance are functions of rotor position, (θ). This is in contrast to the stepping driver, in which voltage was a function of time.

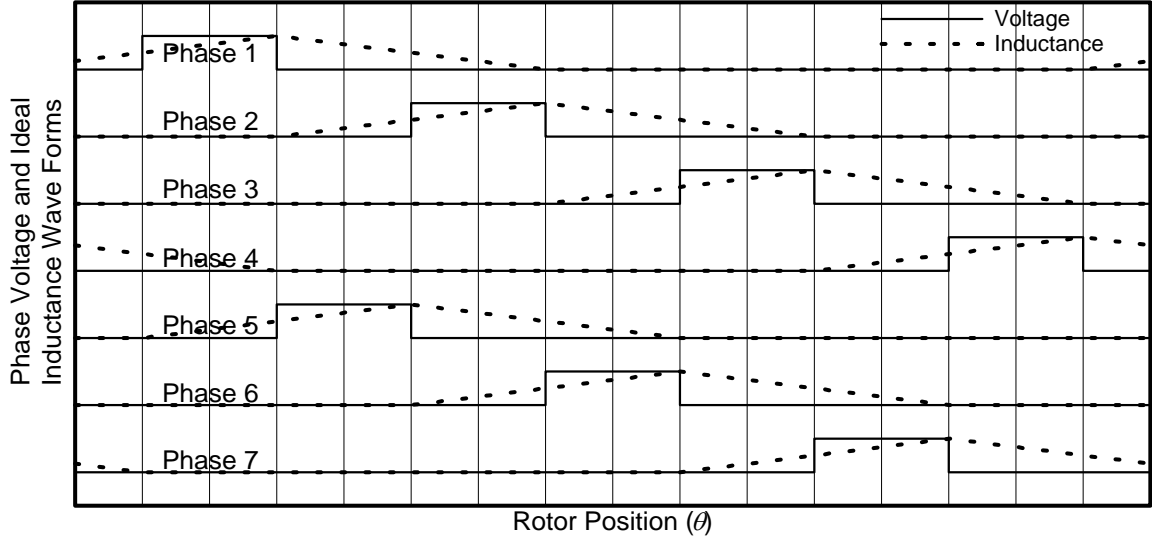


Figure 3-10. The voltage, $v_m(\theta)$, and ideal inductance, $L_m(\theta)$, wave forms with respect to rotor position, θ , when the motor is driven with the brushless driver scheme.

In this case, the phase voltage loop equation from the mathematical modeling section (equation (eq1)) can be written as

$$v_m(\theta) = R_m i_m + L_m \frac{di_m}{dt} + e_m, \quad m = 1..M \quad (\text{eq15})$$

To gain insight into the general behavior of the prototype motor operation with the brushless driver, we will consider static torque production. This is sometimes called starting torque and corresponds to the electrical torque experienced by the rotor when it is stopped or just starting to move. In this case, the last two terms in equation (eq15) become zero and we are left with

$$v_m(\theta) = R_m i_m, \quad m = 1..M \quad (\text{eq16})$$

From equation (eq16), it is clear that phase current can be considered as a square wave with respect to position. In addition, phase current will be in phase (with respect to position) with $v_m(\theta)$, since R_m is assumed to be a constant. For the static torque case, we can write current as a function of position by solving equation (eq16) for i_m . Substituting this into equation (eq6) from the mathematical modeling section, we can express static torque as a function of position and of the magnitude of the supply voltage.

$$\begin{aligned}
 T_{e,Static} &= \sum_{m=1}^M T_{m,Static} \\
 &= \sum_{m=1}^M \frac{1}{2} \left(\frac{v_m(\theta)}{R_m} \right)^2 \frac{\partial L_m(\theta)}{\partial \theta}
 \end{aligned} \tag{eq17}$$

Inspection of the wave forms shown in Figure 3-10 reveals that each $v_m(\theta)$ pulse is associated with a non-zero, positive rate of change of $L_m(\theta)$. From this it is clear that the summation in equation (eq17) will have at least one non-zero term for every possible position of the rotor. This eliminates the dead zones that were seen in the open loop stepping driver.

Current in the steady state constant average rotor velocity case, while no longer a simple step function with respect to position, is still non-zero only when v_m is non-zero (i.e. when the m th coil is energized via the source). The result that dead zones cannot occur is still valid, but the steady state torque cannot be described solely as a function of rotor position.

In the description of the stepping motor driver, the average steady-state rotor velocity was found to be a function of time only, so long as the source voltage is sufficient to keep rotor in step with the switching sequence. In the brushless driver case, average steady-state velocity is a function of the source voltage and the load torque.

Figure 3-11 shows a schematic diagram of the brushless DC motor driver circuit. In this figure, the steering circuit receives rotor position signals, θ , and produces the required

switching control signals, Q1, Q2, ... Q7. These signals control the power switching transistors and the energizing of the stator phases.

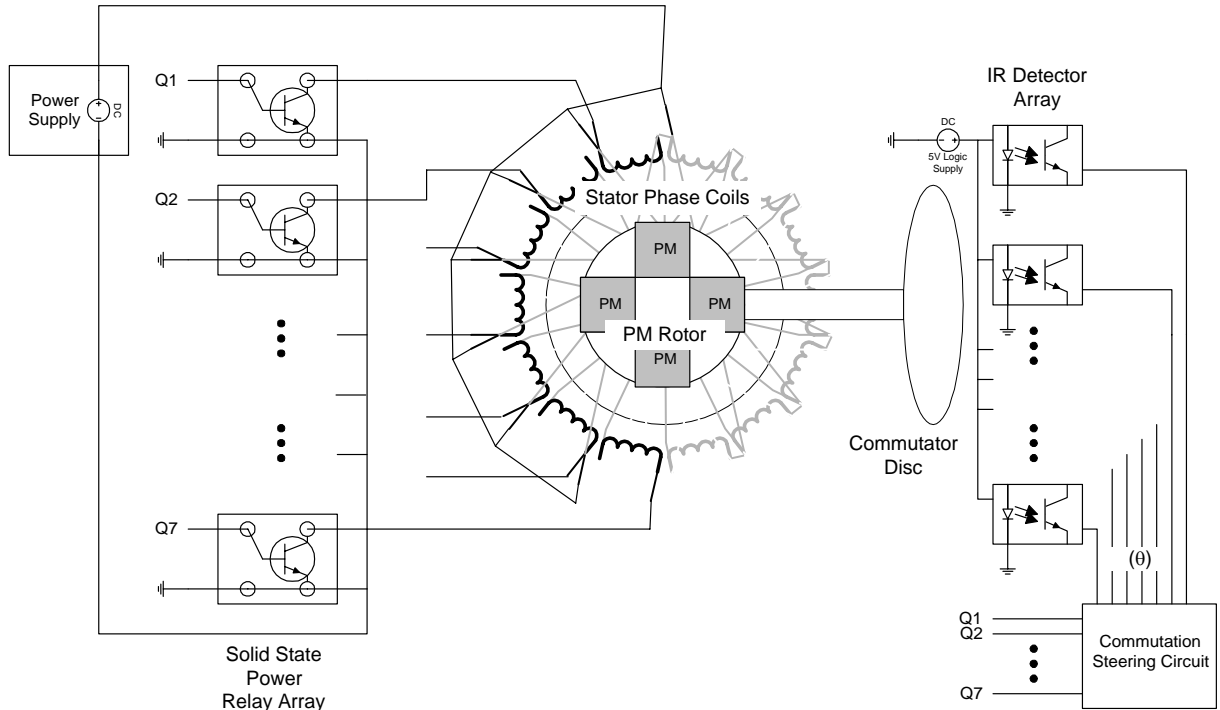


Figure 3-11. Schematic diagram of the brushless DC motor driver configuration.

The stepping motor driver and the brushless DC motor driver can be used to demonstrate the effects of different control strategies on motor performance. For example, in the open loop stepping case, the motor speed was determined by the computer-timed stepping sequence. Supply voltage did not affect the speed of the rotor so long as it was sufficient to energize the phases. In contrast, the brushless driver configuration can allow the motor to behave similarly to a brushless DC motor [45][46]. In this case, speed is regulated by the supply voltage level and the load.

V. Experimental Fault Simulation Platform Description

This section describes an experimental fault simulation platform built around the prototype motor described above. The exposed topology and the accessible interior of the prototype axial flux variable reluctance motor make it a good candidate for motor fault research. For example, sensors, such as thermocouples, can be attached directly to the surfaces of the stator windings without the need to disassemble the motor. The platform described is intended to support the investigation of winding faults such as turn-to-turn faults and open phase faults. Figure 3-12 shows a photograph of the experimental fault simulation platform in the ADAC laboratory.

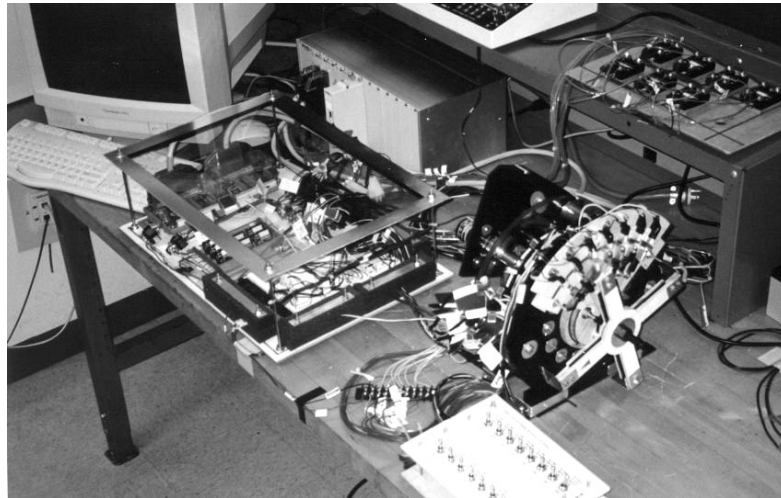


Figure 3-12. Photograph of the experimental fault simulation platform in the ADAC laboratory.

Winding faults are a major cause of motor failure. Over time, and in the presence of heat and adverse conditions, wire insulation in a motor coil can degrade. This situation will generally lead to one or more low resistance paths between neighboring turns in the coil. The result is that a portion of the coil will be shorted out. This can result in excessive heat generation, vibration, and a change in motor torque output. If such faults are not detected, the motor may suffer catastrophic failure at a later time. For systems in which

safety or continual performance are critical factors, it may be important to detect faults so that the present condition of the motor can be assessed, and so that maintenance can be scheduled.

To facilitate the study of turn-to-turn coil faults, the coils in one of the stator phases were wound with taps at various points in the coil. Figure 3-13 panel (a) shows one of the experimental fault simulation coils. The coils can simulate turn-to-turn shorts involving between 1% to 50% of the coil turns. Each of these taps were connected via separate switches to the phase common ground. A schematic representation of one of the fault simulation coils is shown in panel (b) of Figure 3-13. This arrangement allows for the simulation of several winding faults. These include coil turn-to-turn faults of various magnitudes, open phase faults, and maintenance faults in which a coil has been improperly wound or connected.

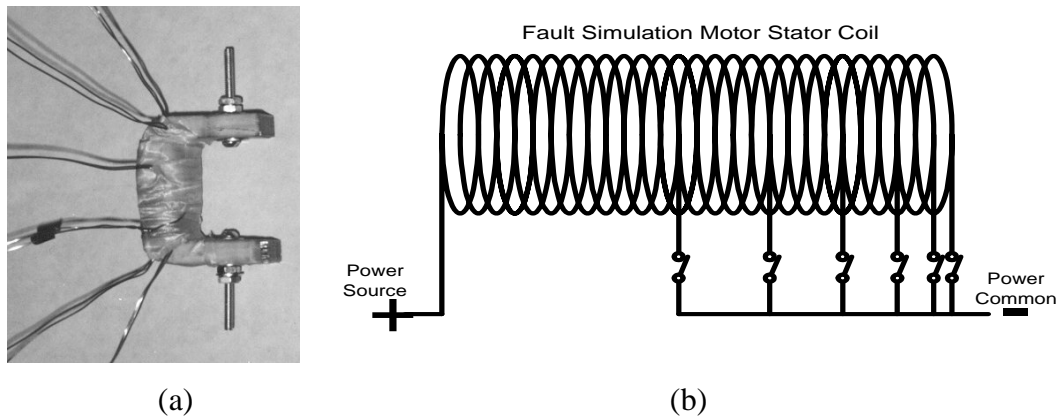


Figure 3-13. The experimental fault simulation coil. (a) A photograph of a fault wound coil. (b) Diagram indicating the locations of the fault simulation tap switches.

The motor was fitted with various sensors so that data could be collected via computer. Both the fault simulation phase and a normal healthy phase were fitted with voltage and current sensors. In addition, a high-resolution position encoder (OMRON model E6B2 rotary encoder, 2000 ppr) was mounted on the rotor shaft. Several of the stator windings were also fitted with RTD thermocouples. The data from these sensors can be collected

and stored on a computer using National Instruments software and hardware. A National Instruments SCXI-1121 8 input isolated op amp module was used to collect the data. The data collection and fault simulation platform configuration is shown in Figure 3-14.

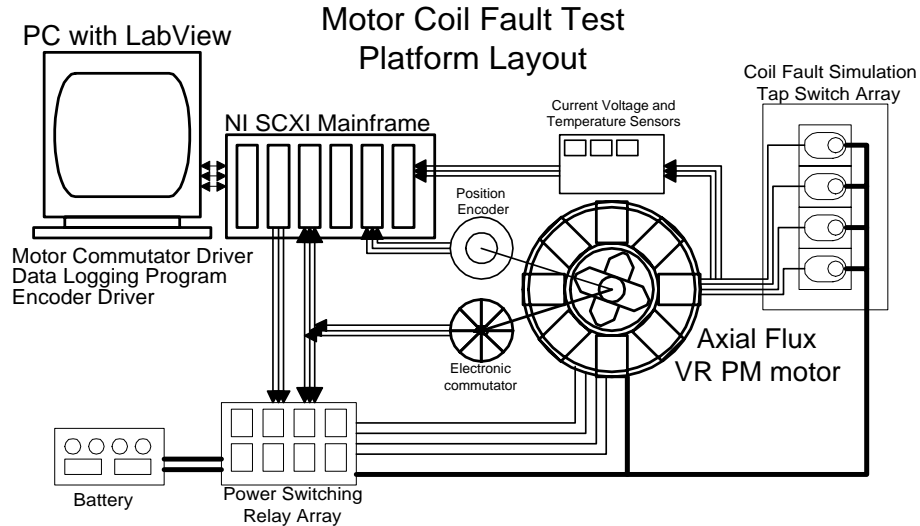


Figure 3-14. Schematic layout of the fault simulation and data collection platform.

As noted above, a primary focus of the experimental fault simulation and data collection platform is to perform research related to the characterization of winding faults in variable reluctance permanent magnet motors. The platform can also be used as a tool to demonstrate the effects of winding faults for educational purposes. Faults can be introduced while the motor is running. Some of these faults produce tangible effects in the motor's performance. In addition, current, voltage and temperature data are reported in graphic form on the PC. This gives students an opportunity to see a detailed profile of the effects of such faults on this type of motor. Students can also turn the rotor by hand and see a plot of the resulting back emf on the computer. Figure 3-15 shows graphic user interface screens from the PC based motor data collection portion of the experimental platform. For the screens shown, the motor is configured to experimentally simulate a 47% turn-to-turn stator coil short in phase number one. In panel (a), the rotor has been turned by hand and the resulting PM rotor induced back emf wave forms are shown. In panel (b), the motor was powered by a Tektronix PS280 constant voltage supply set to 5

Volts. In each case, the graphic interface reports current and voltage wave forms measured in both a healthy phase (phase 2) and in the experimental fault phase (phase 2).

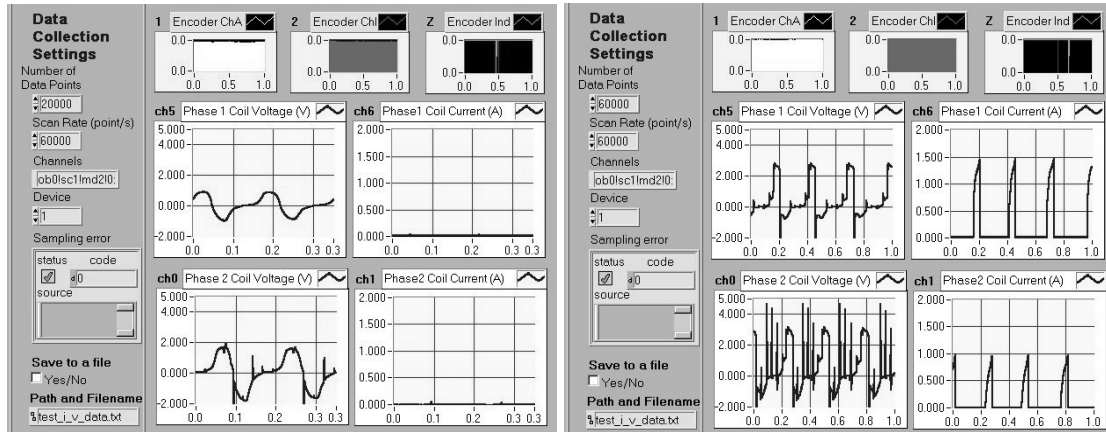


Figure 3-15. Examples of motor data reported by the motor platform graphic user interface. (a) Phase back emf voltage wave forms. (b) Phase voltage and current wave forms.

VI. Example Uses of the Platform and Closing Remarks

Some Uses of the Motor Platform

The motor platform was used as motivation for a class project for a graduate level optimal control course taught in the Electrical Engineering department at North Carolina State University. In this course, students derived state space models for the motor system and formulated optimal control laws to drive the motor under simple conditions. Performance measures such as minimum time and minimum energy were considered.

The platform was used by an undergraduate student research group to investigate various motor control issues. The students measured various physical motor parameters and then developed simulation models of the dynamical behavior of the motor. In this project, students used National Instruments and LabVIEW to implement a controller for the

prototype motor based on their modeling efforts. Among other things, this type of project allows students to investigate elements of computer based motor control systems and to implement control on a physical motor system.

The motor has also been used on several occasions for demonstration during departmental laboratory open houses. By directly illustrating elements of motor control and motor faults, such demonstrations can help to attract students to fault diagnosis and control areas of study.

Closing Remarks

This paper has described a prototype axial flux variable reluctance permanent magnet motor and associated experimental fault simulation platform. This platform has been presented as a tool for educational demonstration and for motor coil fault research. The motor described here was designed with a relatively exposed architecture compared to other motor topologies. This facilitates its use as a demonstration and teaching tool.

Using a physical system such as the one described, in conjunction with computer simulation and theory, can help to motivate students, and to tie theory to application. The motor described in this work has been used in control and modeling classes in the electrical engineering curriculum.

A detailed description of the axial flux variable reluctance permanent magnet motor design was presented. In addition, the associated fault simulation platform was described and results generated using this platform were presented.

Acknowledgments

The authors of this paper would like to acknowledge the support of the National Science Foundation grants ECS-9521609 and ECS-9610509 which helped make the work at the ADAC lab possible.

References

See Thesis Bibliography.

Analysis of Rotor Velocity Damping Due to Coil Faults in an Axial Flux Variable Reluctance PM Motor.

Andrew L. Nelson and Mo-Yuen Chow
Department of Electrical and Computer Engineering
North Carolina State University
Raleigh, NC 27695
USA.

Abstract

In recent years, variable reluctance (VR) and switch reluctance (SR) motors have been proposed for use in applications requiring a degree of fault tolerance. A range of topologies of brushless SR and VR permanent magnet (PM) motors are not susceptible to some types of faults, such as phase to phase shorts, and can often continue to function in the presence of other faults. In particular, coil winding faults in a single stator coil may have relatively little effect on motor performance, but may affect overall motor reliability, availability and longevity. It is important to distinguish between, and characterize, various winding faults for maintenance and diagnostic purposes. This paper examines rotor velocity damping due to stator winding turn-to-turn short faults in a fault tolerant axial flux variable reluctance PM motor. In this type of motor, turn-to-turn shorts due to insulation failures have similar I-V characteristics to coil faults resulting from other problems, such as faulty maintenance or damage due to impact. In order to investigate the effects of such coil faults, a prototype axial flux variable reluctance PM motor was constructed. The motor was equipped with experimental fault simulation stator windings capable of simulating these and other types of stator winding faults. The salient finding of this research is that two common types of winding faults can be differentiated by their effects on rotor velocity in this type of motor. These fault

characterization and analysis results are a necessary first step in the process of motor fault detection and diagnosis for this motor topology.

Key Words: Winding fault, turn-to-turn fault, insulation failure, variable reluctance motor, axial flux, brushless DC, failure analysis, stator fault, fault tolerant design, electric vehicle propulsion.

I. Introduction

For specialized applications SR and VR permanent magnet motors are often designed to be less susceptible to various faults [40][47]. These motors generally possess a high degree of electrical and magnetic isolation between the stator phases. This makes phase to phase faults unlikely [40]. In addition, brushless versions of these motors with PM rotors lack rotor coils and commutator brushes, and hence are not susceptible to faults involving these components. In many cases, it is found that SR and VR motors that have not been specifically designed for fault tolerance still possess a high degree of resistance to certain types of faults.

Arguably, the largest class of faults to which these types of motors remain vulnerable are those involving winding failures. In more traditional topologies, such as induction motors and three phase synchronous machines, a winding failure can cause severe degradation of motor performance [21]. In contrast, many fault tolerant SR and VR motors will continue to operate under the influence of winding failures with a minimum of performance degradation [48]. Some of these motors can operate with the complete loss of a stator phase. Even in the case of fault tolerance, fault identification and characterization remains a priority. Although many of these types of motors continue to operate with winding failures, if the fault is not detected, the future performance of the motor may be jeopardized. Other factors secondary to the primary fault may cause

catastrophic failure of the motor. These include increased vibration, and heat generation. In motor applications in which safety is a factor, it is important to detect faults even if the motor is capable of continued operation. If such a fault is detected, the motor's new fault imposed operation limits can be assessed and maintenance can be scheduled.

This paper focuses on the investigation and analysis of insulation failure induced turn-to-turn stator coil shorts in which a significant portion of the coil has been shorted out. This type of fault can be the result of a single insulation failure between two adjacent coil turns if the turns happen to be in adjacent winding ranks. In the case of this particular fault, an associated drop in rotor velocity can be detected under situations of open loop constant voltage control. In contrast, a similar fault, in which a portion of the coil is actually destroyed or removed in a manner that allows the remainder of the coil to continue to carry current, is not associated with a decrease in rotor velocity.

The prototype motor used in this work was designed to be similar to experimental in-wheel drives for electric vehicles and mobile machines. In addition, this motor was specifically designed to facilitate stator winding fault simulation. The motor has a relatively exposed architecture, allowing for invasive testing and data collection. In particular, the coils in one of the stator phases have been wound to include a set of inter-turn taps. Each tap is connected via separate switches to a common ground. This arrangement allows several faults to be simulated experimentally. These simulated faults include coils with turn-to-turn shorts, coils with a reduced number of turns, and open circuited phase faults.

II. Motor Description

Variable reluctance permanent magnet motors are sometimes designed with unconventional geometries for use in special applications [11][38]. In recent years

variable reluctance motors have gained attention as candidates for use in electric vehicle propulsion systems[7][49]. Variable reluctance motors designed with flux path isolation lend themselves to unconventional topologies more than traditional motor types because there is relatively little interaction between the different phases. This allows for greater freedom in stator coil shape, and in the number of stator coils used. Several such motors have been described in the literature. These include a five phase 22 pole motor with a claw-type rotor for use in small electric vehicles [39], and an axial flux brushless DC motor for use in a solar-electric vehicle [50].

The motor described in this work is an axial flux variable reluctance permanent magnet disc motor with 14 stator coils and 4 pairs of rotor PM poles. This motor was prototyped in the Advanced Diagnosis and Control (ADAC) laboratory at North Carolina State University. The prototype motor is shown in Figure 4-1. In this motor design, the phrase "axial flux" indicates that the stator coils and rotor poles pairs are arranged so that the magnetic flux paths have components that are parallel to the axis of the rotor. This will be discussed in more detail with a description of the stator and rotor designs.

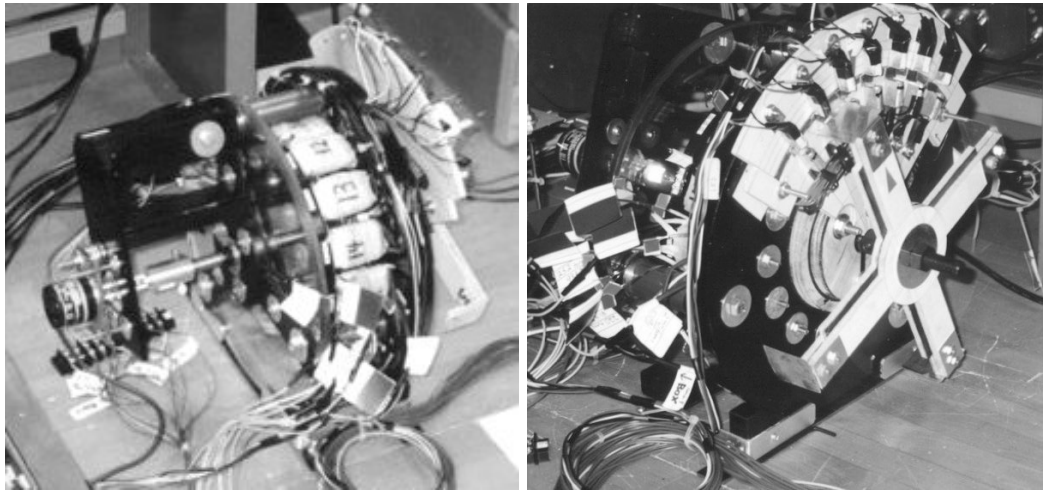


Figure 4-1. The axial flux variable reluctance DC motor.

The motor is designed with 7 stator phases. Each stator phase consists of two coils to make a total of 14 stator coils. The stator coils are wound on separate laminated cold

rolled steel cores, which are attached to a non-conducting substrate. Each stator coil is isolated from the others both electrically and magnetically. The only iron in the stator is contained in the coil cores. The remainder of the stator is made up of non-conductive material, and serves a structural roll only. These cores also serve as flux paths to direct the mmf to the rotor. Each core has two machined surfaces that make up the stator side of the air gap.

The rotor is a disc with permanent magnets imbedded close to the edge of the disc so that each pole of every magnet is oriented toward one or the other face of the disc. The term "pole pair" refers to a set of north and south poles from a single permanent magnet. As with the stator coils, the rotor pole pairs are magnetically isolated from one another. In this type of motor, flux does not pass through the center of the rotor and the majority of the material making up the rotor is not conductive to magnetic flux. The rotor side of the air gap is made up of short iron flux paths that direct magnetic flux to/from the individual permanent magnet pieces.

A cross-sectional view of the motor topology depicting the relationship of the stator coils and the rotor poles is shown in Figure 4-2. The arrangement of the 4 PM pieces in the rotor produces 4 axially oriented pole pairs spaced at 90 degree intervals. Likewise, the stator coils are arranged to induce north and south poles oriented axially as to attract (or repel) a pair of rotor poles when energized. Because the motor is designed to operate with unidirectional coil current and unidirectional flux generation, it is desirable to maximize the distance between consecutively firing stator coils while minimizing the step size the rotor must cover for each commutation segment. The traditional three phase 6:4 configuration is well suited for small motors with bi-directional flux generation and in which coils are energized in a positive-negative-off sequence. These motors are generally designed so that rotor travels half the radial distance between to consecutive stator coils during each commutation sector. The 7 phase 14:4 arrangement allows for the same half step commutation scheme but introduces an extra stator pole between each

consecutively firing stator coil. Increasing the number of coils per phase allows for a greater overall motor radius and hence a greater torque lever arm for each stator coil-rotor pole interaction.

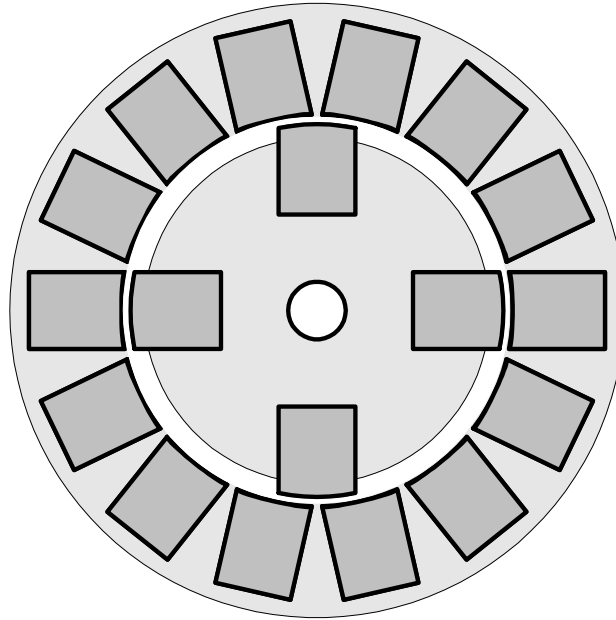


Figure 4-2. Top view of the prototype motor showing the relative locations of the rotor poles and the stator coils.

A brushless DC motor driver strategy was used in this work. Brushless DC motors use rotor position sensors to coordinate power switching to the stator phases with regard to rotor position. The rotor position sensor(s) produce signals that allow the driver to electronically commutate the motor phases. The actual phase switching is generally done by solid state power switching transistors such as power MOSFETs. Brushless DC motors often use Hall effect sensors or optical encoders to determine rotor position. The motor described here uses an array of infrared (IR) sensors to detect rotor position to a resolution of one stator phase sector.

The brushless motor driver implemented on the prototype motor uses an inner rotor position closed loop to commutate power switching to the stator phase. An outer open loop is used to control motor speed via a variable voltage source. Motors driven in this

manner have similar dynamics to those of traditional DC motors. Although less common in industrial settings, this type of control is often used in electric vehicle propulsion systems in which the vehicle operator controls the motors speed and torque via an accelerator pedal.

III. Mathematical Model

In this section, mathematical equations describing the dynamical behavior of a generalized axial flux variable reluctance motor with M stator coils and P permanent magnet rotor pole pairs will be presented. Note that the particular motor described in this paper has $M = 14$ and $P = 4$. The dynamical equations presented in this section are similar to standard variable reluctance and switched reluctance motor equations found in the literature [38][30][41]. It should be noted that variable reluctance and switch reluctance motor dynamics are generally nonlinear. Unlike the case of the standard DC motor, the prototype motor described in this work is not modeled by a set of linear equations.

The voltage loop equation for a particular stator coil (the m th coil), is given by equation (4-1) as follows:

$$v_m = R_m i_m + L_m \frac{di_m}{dt} + e_m, \quad m = 1, \dots, M \quad (4-1)$$

where v_m is the source voltage applied over the m th stator coil, R_m is the resistance of the m th coil, L_m is the self inductance of the m th coil, and e_m is the induced voltage in the m th coil due to the rotation of the permanent magnet rotor (i.e. 'induced back emf'). As indicated in the previous section, variable reluctance motors of the type described in this paper possess a high degree of electrical and magnetic isolation between the phases. There is no direct iron flux path between the various stator coils, and hence the mutual inductance is considered to be negligible [38]. L_m is a function of rotor position, θ , while

e_m is a function of both rotor position and rotor velocity, ω . For modeling purposes, L_m and e_m are often approximated by piecewise linear curves [42][43]. In the case of e_m , the piecewise linear curve would be scaled by a term proportional to ω .

For purposes of analysis, it will be convenient to express $L_m(\theta)$ in the following form:

$$L_m(\theta) = Nk_L l_m(\theta) \quad (4-2)$$

where N , k_L , and $l(\theta)$ are the number of turns per coil, a constant representing the static elements of the flux path (i.e. the permeability of the core and the PMs), and a unit function representing the variable part of the flux path, respectively. The partial derivative of $l_m(\theta)$ with respect to θ will be used later in the motor torque equation. This is also approximated by a piecewise linear curve. Figure 4-3 shows idealized wave forms used to approximate the unit wave form inductance seen by a single phase, $l_m(\theta)$, and its partial derivative with respect to θ . The shaded portion of Figure 4-3 indicates the phase sector of the stator phase corresponding to the waveforms shown (phase 1).

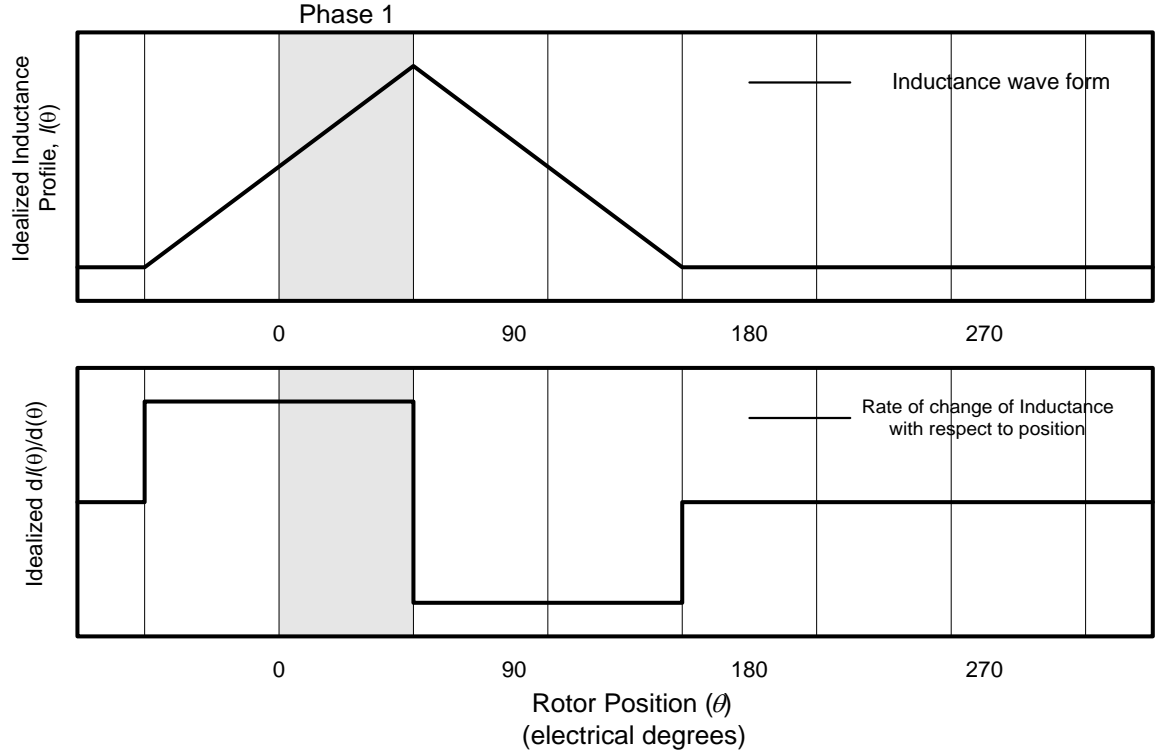


Figure 4-3. The idealized unit piecewise linear wave forms, $l_m(\theta)$, and its partial $d l_m(\theta)/d\theta$ with respect to θ . These curves are shown for 360 electrical degrees.

The $k_L(\theta)$ term in equation (4-2) accounts for deviations from the idealized wave form as well as constant factors due to the static parts of the flux path. This term is generally derived from experimental data and is particular to each specific motor topology. This paper is not primarily focused on modeling. As such, the idealized wave forms shown in Figure 4-3 will be sufficient for the later analyses in this work.

The motor is considered to operate under non-saturating flux conditions. In this case, the inductance, L_m , is a function of rotor position only [51]. Then the flux linkage in the m th coil is given by

$$\phi_m = L_m(\theta)i_m \quad (4-3)$$

In the formulation of state space equations it will be convenient to solve (4-3) for i_m to give

$$i_m = \frac{\phi_m}{L_m(\theta)} \quad (4-4)$$

The net electrical torque applied to the rotor by a given stator coil can be written as [44]

$$T_m = \frac{1}{2}(i_m)^2 \frac{\partial L_m(\theta)}{\partial \theta} \quad (4-5)$$

The total torque is then given by the sum of the torques due to each of the stator coils:

$$T_e = \sum_{m=1}^M T_m \quad (4-6)$$

The motor mechanical dynamics are described by the sum of the various mechanical loads on the rotor. This is given by

$$T_e = J \frac{d\omega}{dt} + B\omega + T_l \quad (4-7)$$

In the torque equations, T_e is the electrical torque on the rotor, J is the moment of inertia of the system, B is the damping coefficient, and T_l is the load torque.

Finally, from basic physics, the angular velocity and position are related by

$$\omega = \frac{d\theta}{dt} \quad (4-8)$$

To formulate the state space equations for this model, we will select

$$\phi_1, \phi_2 \dots \phi_m$$

$$\omega, \text{ and}$$

$$\theta$$

as the state variables and

$$v_1, v_2 \dots v_m$$

as the inputs.

Substituting (4-4) into equation (4-1), and then solving for $d\phi_m/dt$ gives m state equations of the form

$$\dot{\phi}_m = v_m - R_m \frac{\phi_m}{L_m(\theta)} - e_m \quad (4-9)$$

Equating (4-6) and (4-7) gives

$$T_e = \sum_{m=1}^M T_m = J \frac{d\omega}{dt} + B\omega + T_l \quad (4-10)$$

Solving equation (4-10) for $d\omega/dt$ we get

$$\dot{\omega} = \frac{1}{J}(T_e - B\omega - T_l) \quad (4-11)$$

and equation (4-8) gives our last state equation.

$$\dot{\theta} = \omega \quad (4-12)$$

IV. Description of Experimental Platform Setup

In this section, the experimental fault simulation platform used to generate and record the data presented in this paper is described. The fault simulation platform is built around the prototype motor described previously in section II. The exposed topology and the accessible interior of this axial flux variable reluctance motor make it a good candidate for motor fault research. Sensors can be attached directly to the surfaces of the stator windings without the need to disassemble the motor. In addition, individual stator coils can be removed without the need to fully disassemble the motor. Figure 4-4 shows a photograph of the experimental fault simulation platform in the ADAC lab.

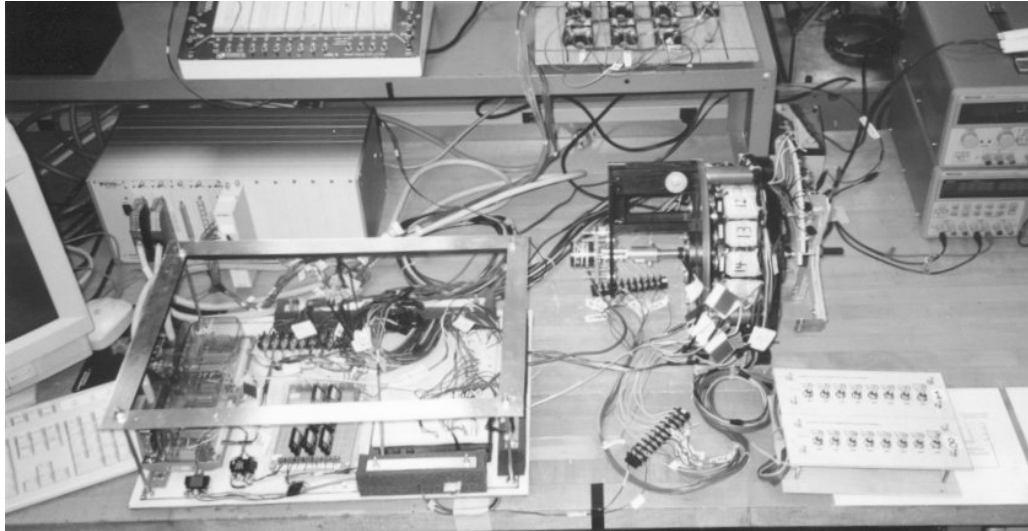


Figure 4-4. A photograph of the experimental fault simulation platform in the ADAC lab.

To facilitate the study of turn-to-turn coil faults, the coils in one of the stator phases (phase 1) were wound to include inter-turn taps at various points in the coil. These taps were connected via separate switches to the phase common ground. By connecting the coil taps to ground and/or to each other, various winding related faults can be experimentally simulated. The platform can be used to experimentally simulate turn-to-turn shorts involving between 1% and 50% of the coil turns. Such turn-to-turn faults result from insulation breakdown between the coil winding turns. Another related fault that can be simulate is one that results in a reduced number of coil turns but in which the faulted portion of the coil is destroyed or removed. Such faults can occur as a result of improper maintenance of damage due to impact. A schematic representation of one of the fault simulation coils is shown in Figure 4-5.

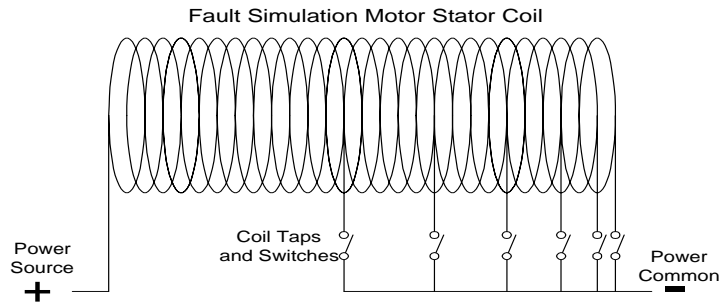


Figure 4-5. Diagram of the experimental fault simulation coil indicating the locations of the fault simulation tap switches.

The motor was fitted with various sensors so that data could be collected via computer. The experimental fault simulation phase, and a healthy phase were fitted with voltage and current sensors. In addition, a high resolution (2000 ppr) position encoder was mounted on the rotor shaft so that rotor position and velocity data could be recorded. The data from these sensors can be collected and stored on a computer using National Instruments software and hardware. A National Instruments SCXI-1121 8 input isolated op amp module was used to collect the data. The data collection and fault simulation platform configuration is shown in Figure 4-6.

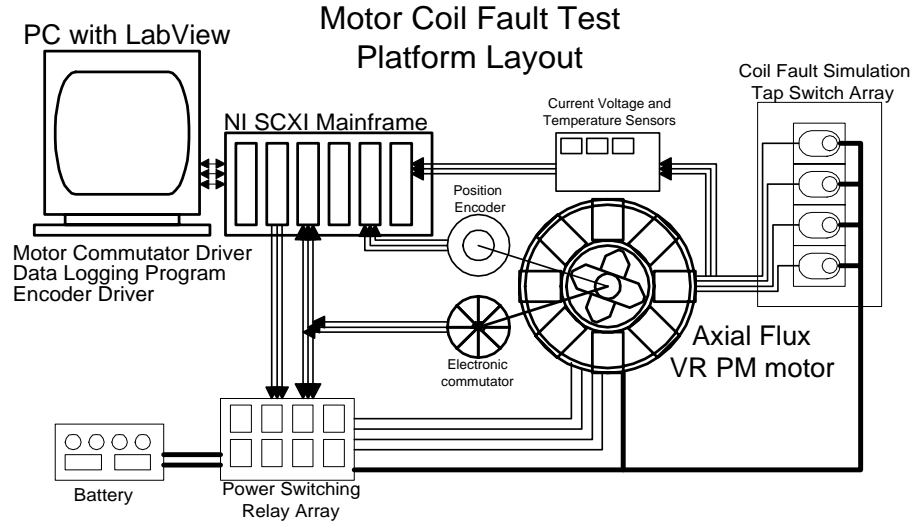


Figure 4-6. Schematic layout of the fault simulation and data collection platform.

V. Results

This section presents data and results generated with the experimental platform and prototype motor described in the previous sections.

This section shows four experimental fault cases. In each experimental run, rotor position and velocity were recorded. In addition, voltage and current were measured on both the experimental fault simulation phase (phase 1) and on a healthy phase (phase 2). The four experimental cases are described in the following paragraphs.

Figure 4-7 will be referred to in the following descriptions of each of the fault cases. This figure illustrates the experimental fault simulation phase coil and tap switch configurations used in each of the experimental fault simulation cases.

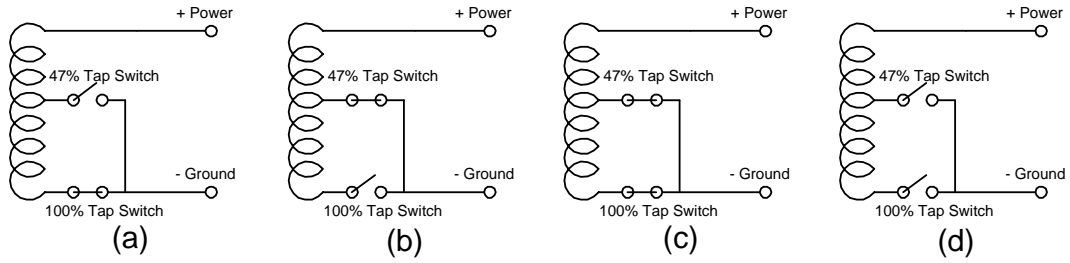


Figure 4-7. Experimental fault simulation phase with tap switches shown: (a) No-fault: 100% switch closed only. (b) Reduced-coil fault: 47% switch closed only. (c) Turn-to-turn short fault: both 47% and 100% switches closed. (d) Open phase: All switches open.

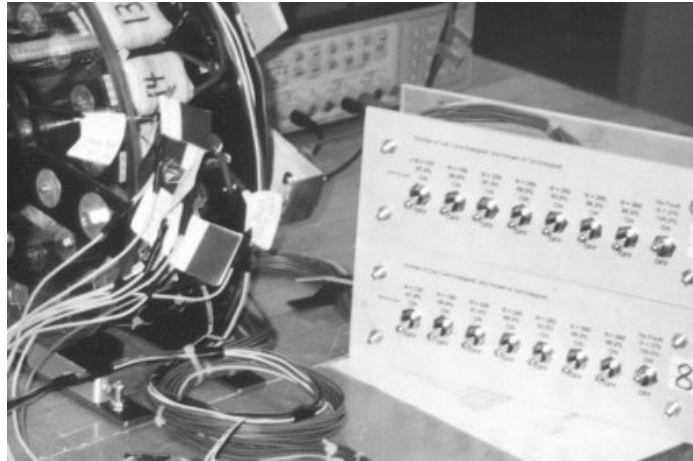


Figure 4-8. The prototype motor showing the experimental fault simulation coil and associated tap switch box.

Figure 4-8 shows a photograph of the experimental fault coil installed in the prototype motor. The tap switch array used to switch the coil taps to ground is also shown in the picture.

In the first case, the control no-fault case, the motor was run at steady state with only the 100% tap switch closed to ground. In this case, the fault test phase is expected to behave similarly to the other healthy phases. This case is illustrated in part (a) of Figure 4-7.

In the second case, data were collected with the 47% tap switch on the experimental fault simulation phase closed only (i.e. the 100% tap switch remains open). This case is illustrated in part (b) of Figure 4-7. This simulates a fault that may occur because of improper motor maintenance or repair, in which a coil has a reduced number of turns. In this case, a portion of the coil is actually destroyed or removed in a manner that allows the remainder of the coil to continue to carry current. This case will be referred to hereafter as the reduced-coil fault. It should be noted that this is not the same as the turn-to-turn coil short, which is considered below.

Case 3 simulates a turn-to-turn fault in which insulation has deteriorated producing a low resistance path from one winding rank to another. In this case, the 47% tap switch and the 100% tap switch are both closed. Here, the power source sees only 47% of the faulted phase coil, but the PM rotor induced current can flow through the entire faulted phase. This case simulates a dramatic coil short in which slightly more than half the coil has been shorted out. The turn-to-turn experimental fault simulation configuration is illustrated in part (c) of Figure 4-7.

In case 4, an open circuited phase fault is simulated by opening all of the tap switches including the 100% switch. This case is included for continuity but is not central to the main topic of this paper. This last case is illustrated in part (d) of Figure 4-7.

The following figures (Figures 4-9 through 4-12) show the results of each of the four fault cases described above. In each of the figures, data are shown for 360 electrical degrees, or one complete commutation switching sequence of the phases. The motor has 1440 electrical degrees for each full revolution of the rotor, hence each plot represents

data taken during a quarter revolution of the rotor. In all cases, time is plotted as the independent variable on the x-axis. The vertical lines in each of the plots mark off the commutation sector divisions (i.e. the points in time where one phase is switched off, and another is switch on.) The y-axes for the various data curves have been kept constant from experiment to experiment to facilitate comparison.

The motor stator phases received power from a Tektronix PS280 5 volt 3 amp constant voltage supply. All data were collected at 27° C, room temperature. The temperature was measured before and after each test and was found to have remained within 1°C of its pre test value.

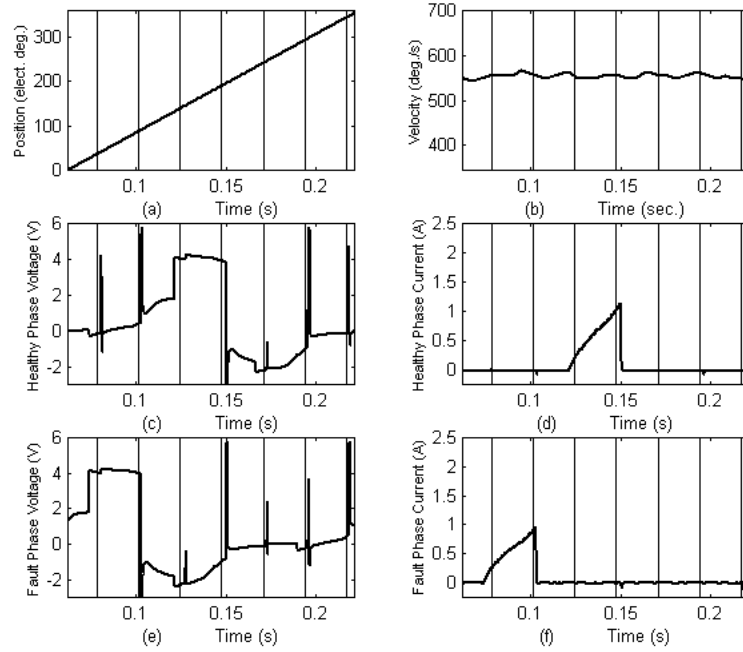


Figure 4-9. No fault motor operation data (case 1).

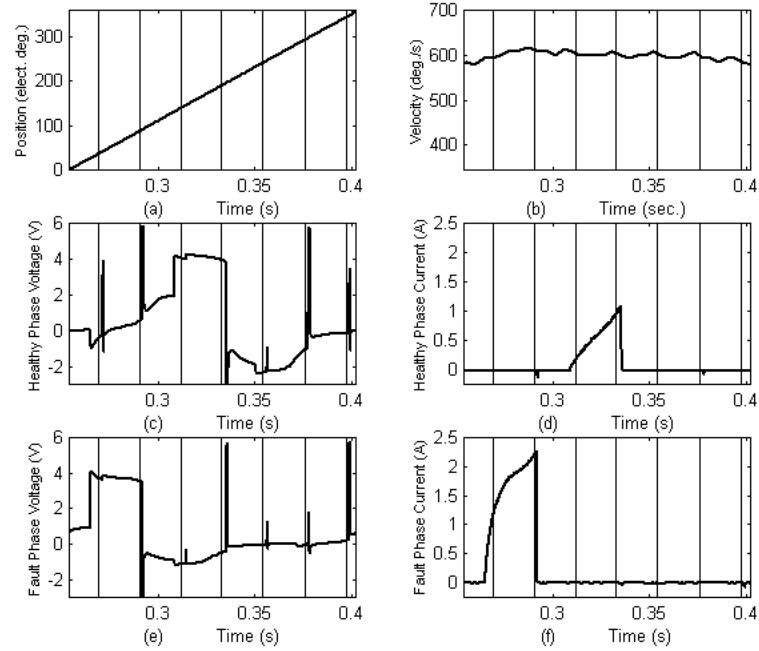


Figure 4-10. Motor operation with the reduced-coil fault (case 2).

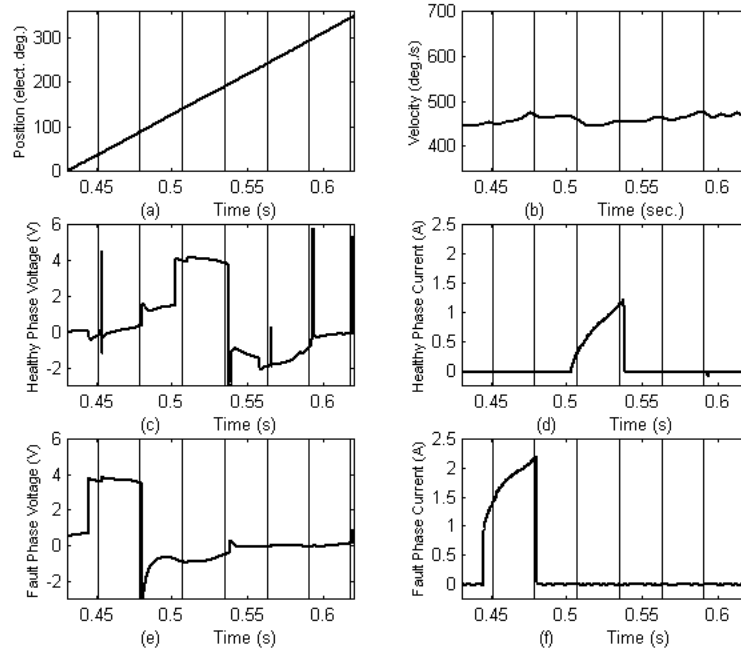


Figure 4-11. Motor operation with the turn-to-turn fault (case 3).

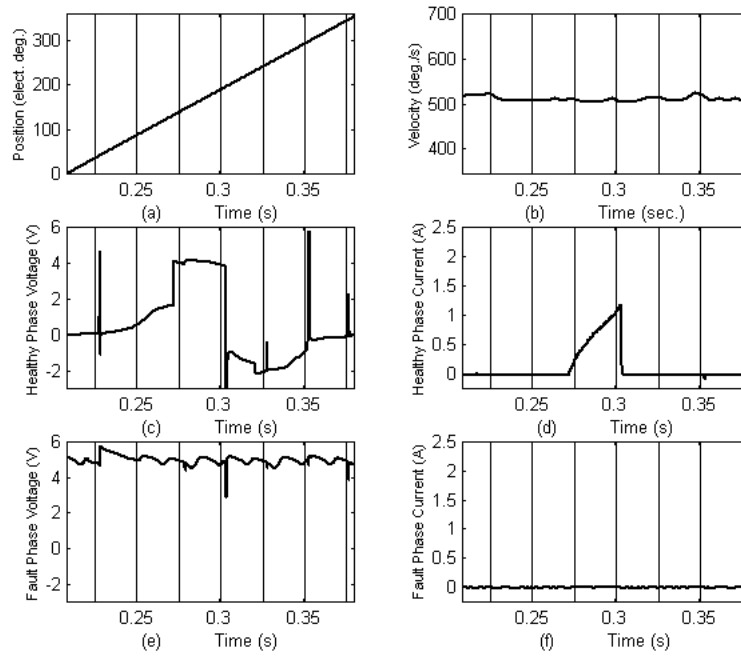


Figure 4-12. Motor operation with the open circuit fault (case 4).

In Figures 4-9 to 4-12, rotor position and velocity are shown in panels (a) and (b) respectively. The rotor position plots are similar in each of the four figures and differ only in slope. The velocity plots were obtained by numerically differentiating the position data in each of the four cases. A velocity ripple can be seen in each of the velocity plots with a valley followed by a peak in each commutation sector. The velocity ripple is caused by pulsations in torque as the PM rotor moves past each energized stator coil.

For each of the four cases, the velocities were averaged over the period of time shown in panels (b) of Figures 4-9 to 4-12. These averages were compared as a percent of the nominal average no-fault velocity. These data are summarized in Table 1 below.

Table 1. Average velocities and percentage of nominal no-fault velocity for cases 1 through 4.

	Case 1	Case 2	Case 3	Case 4
Avg. Velocity (deg/s)	556.03	599.76	463.17	511.67
% of Nominal	100%	107.8%	83.3%	92.0%

Panels (c) and (d) of Figures 4-9 to 4-12 show voltage and current respectively, measured on a normal healthy stator phase (phase 2). All voltages and currents were measured at the stator coil leads on the motor side of the driver transistor relays. Figure 4-13 shows a schematic circuit diagram of the test phase coil and sensor arrangement. In the figure, the locations of the various sensors with respect to the driver relays and the voltage power source are shown. Current sensor 1 in Figure 4-13 was used to collect the data shown above in Figures 4-9 to 4-12. Current sensor 2 was used to measure fault related currents, which are discussed later in Section IV.

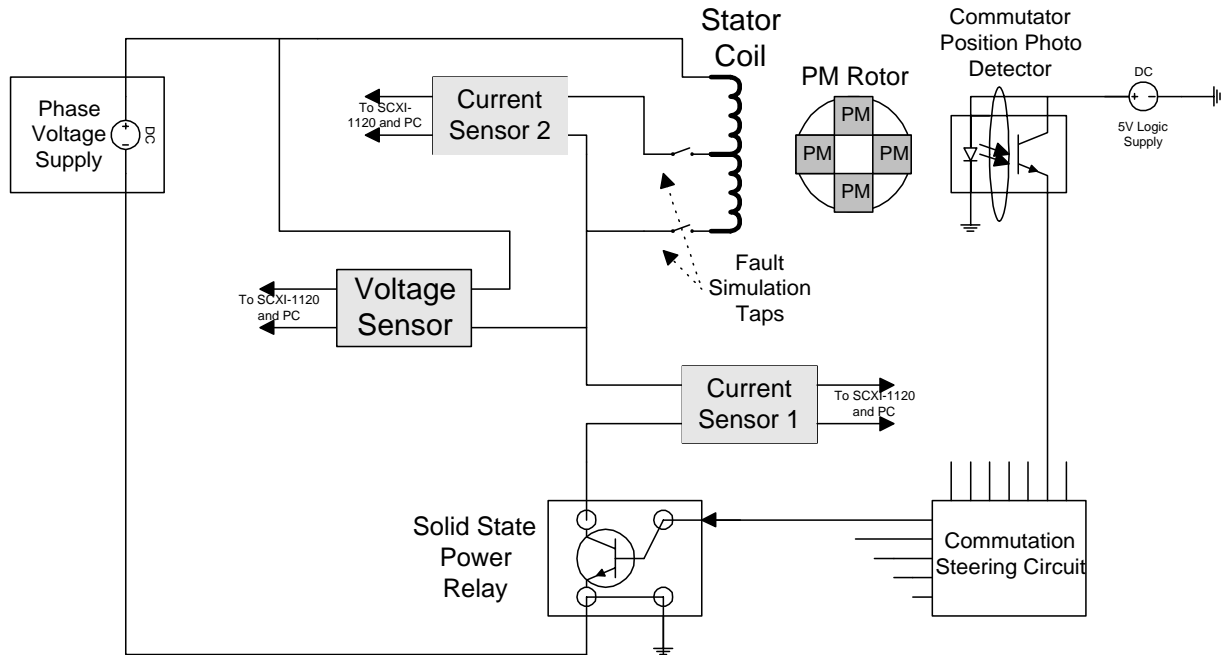


Figure 4-13. Schematic circuit diagram of the experimental fault simulation coil and sensor arrangement.

As discussed in Section II, phase excitation is controlled by the electronic commutation steering circuit in response to rotor position signals. Phase 2 is energized via the commutation steering circuit during the third full commutation sector shown. For panels (c) and (d) of Figures 4-9 to 4-12, this results in a level peak of approximately 4.2 volts and a current peak starting at 0 amps and rising approximately linearly to roughly 1.1 amps. The healthy phase only draws current during its commutation sector. In contrast, a changing voltage, due to PM rotor induced back emf, is seen in the healthy phase during the entire commutation sequence (Figure 4-9, panels c and e). For each of the four test cases, the plots of voltage and current for the healthy phase remain similar.

Voltage and current measurements for the experimental fault simulation phase are plotted in panels (e) and (f) of Figures 4-9 to 4-12. In the nominal no-fault case, the voltage and current plots for the fault phase are similar to those for the healthy phase, except that they are shifted two phase sectors to the left due to the commutation of the phases. Since the

motor was driven with a half phase commutation scheme, the peaks corresponding to the energizing of phases 1 and 2 are separated by a phase sector. Phase 5, whose current and voltage are not shown, is energized during this intervening phase sector between phase 1 and phase 3.

In all four experimental runs, the current and voltage graphs of the healthy phase remain relatively similar. In contrast, cases 2 and 3 show a 302.6% and 303.2% increase in mean current draw compared to the no-fault case, respectively. These correspond to the reduced-coil fault and the turn-to-turn fault, respectively, and are shown in panel (f) of Figures 4-10 and 4-11. Both the reduced-coil fault and the turn-to-turn fault show similar current response for the data shown. The current data for each case were plotted on the same axis against rotor position. This is shown in panel (a) of Figure 4-14. To compare the relative current profiles of the reduced-coil fault and the turn-to-turn fault with respect to the no fault case, difference curves were generated. The nominal no-fault current was subtracted from each of these two fault cases. The resulting curves were plotted on the same axis and are shown in Figure 4-14 panel (b).

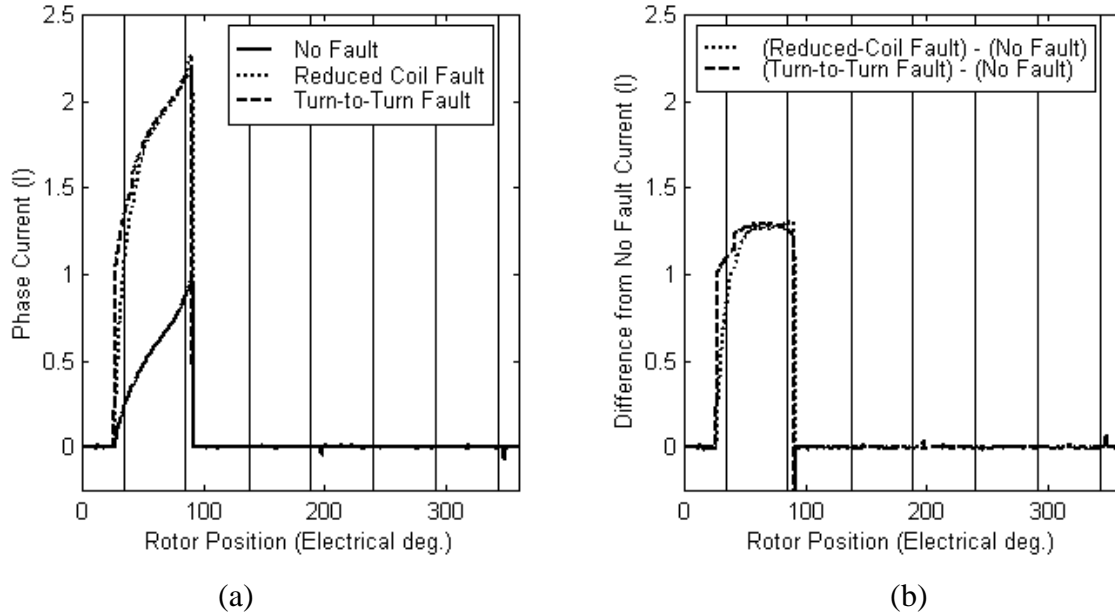


Figure 4-14. Panel (a): Phase current draw for the no-fault case, the reduced-coil fault and the turn-to-turn fault. Panel (b): The differences between each of the two fault cases and the no-fault case are plotted together.

The voltage plots for the reduced-coil and the turn-to-turn fault cases are also similar. These are shown in panel (e) of Figures 4-10 and 4-11 respectively. In both cases, the voltage rises to 3.8V when the phase is energized from the source. This is slightly less than the no-fault level of 4.2 volts. The PM rotor induced back emf voltage is approximately 50% of its no fault value for both case 2 and case 3. The voltage data for each case were plotted on the same axis against rotor position. This is shown in panel (a) of Figure 4-15. To compare the relative voltage profiles of the reduced-coil fault and the turn-to-turn fault with respect to the no fault case, difference curves were again generated. The nominal no-fault voltage was subtracted from each of these two fault cases. The resulting curves were plotted on the same axis and are shown in Figure 4-15 panel (b).

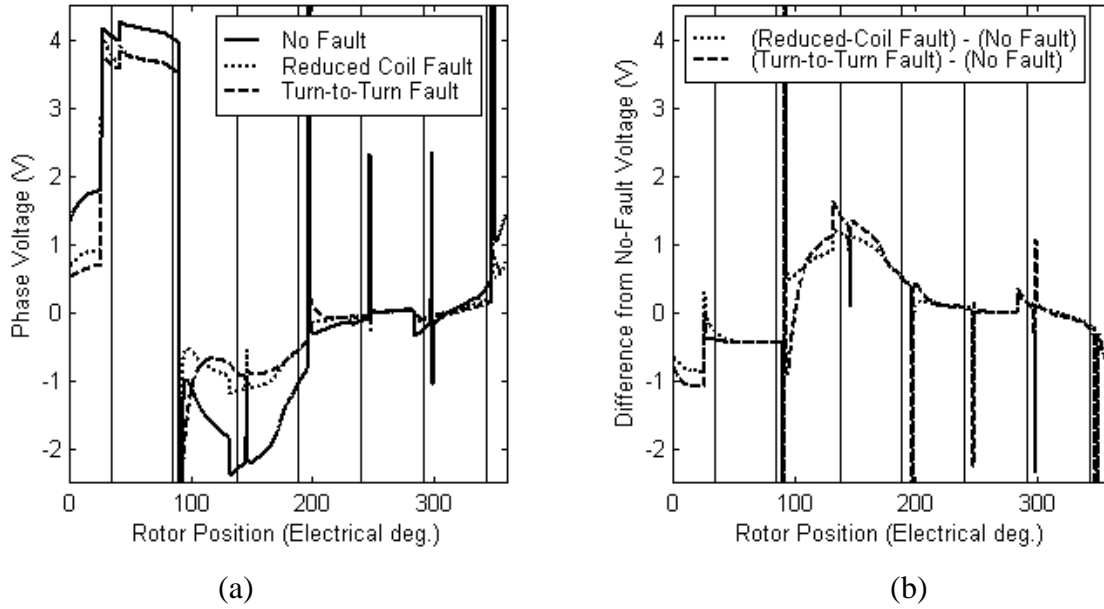


Figure 4-15. Panel (a): Phase voltage for the no-fault case, the reduced-coil fault and the turn-to-turn fault. Panel (b): The differences between each of the two fault cases and the no-fault case are plotted together.

As noted above, the voltage and current profiles of the reduced-coil fault and the turn-to-turn fault are similar. These fault cases can be most easily differentiated from their associated steady state rotor velocities. The reduced-coil fault produces an average rotor velocity of 599.76 degrees per second, while the turn-to-turn fault produces an average rotor velocity of only 463.17 degrees per second. These are shown in panel (b) of Figures 4-10 and 4-11 respectively. Panel (a) of Figure 4-16 shows velocity graphs with respect to rotor position for the no-fault case, the reduced coil case, and the turn-to-turn case. Panel (b) of Figure 4-16 shows the difference between the no-fault case and the reduced coil, and the turn-to-turn cases.

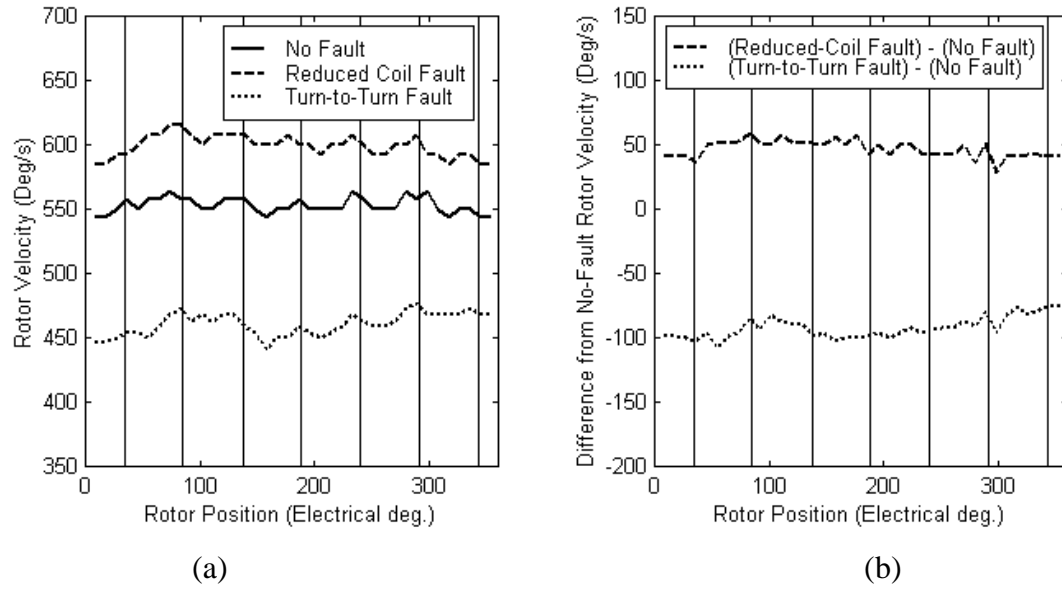


Figure 4-16. Panel (a): Velocity for the no-fault case, the reduced-coil fault and the turn-to-turn fault. Panel (b): The differences between each of the two fault cases and the no-fault case are plotted together.

In order to further investigate the nature of the fault cases discussed above, the current through the 47% tap switch was also measured in each case. The sensor labeled "current sensor 2" in Figure 4-13 shows the point at which these currents were measured. Figure 4-17 shows the current measured through the 47% tap switch for each of the 4 experimental configurations.

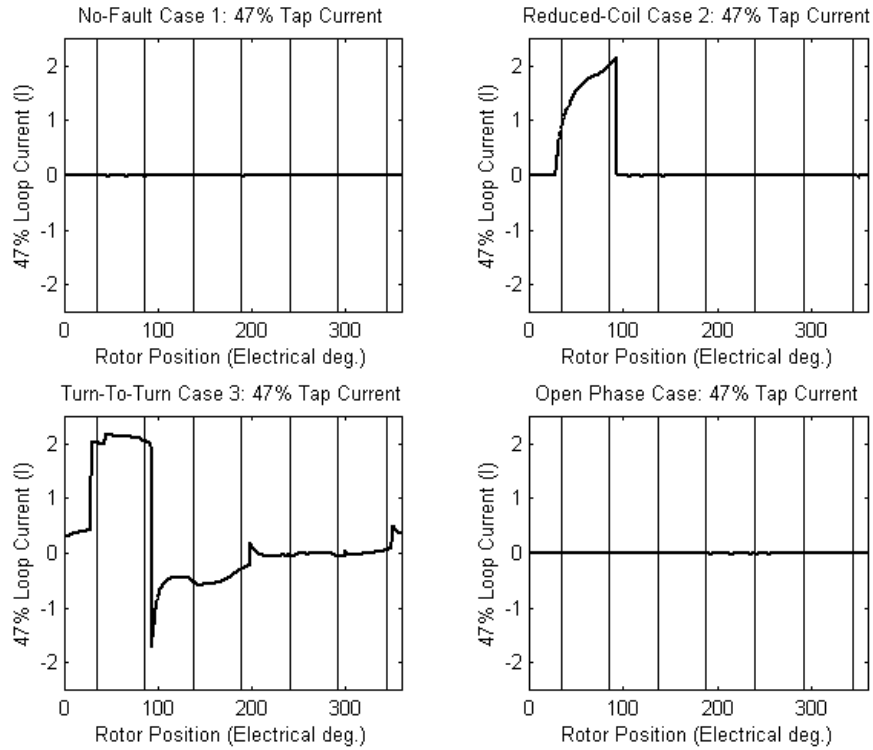


Figure 4-17. Current draw through the 47% tap switch in each of the four experimental configurations. Data are shown for 360 electrical degrees.

VI. Discussion and Analysis

Overview and identification of damping current

In this section, the data presented in the previous section will be examined in greater detail, with an emphasis on the reduction in rotor velocity seen in the turn-to-turn fault of case 3.

The most salient difference between the results of the data taken in case 2 (the reduced-coil fault), and in case 3 (the turn-to-turn failure), is seen in the velocity plots (Figure 4-10 (b) and Figure 4-11 (b)). The reduced-coil fault results in an average rotor velocity of

599.76 degrees per second. This is 108% of the no fault velocity. In comparison, case 3, the turn-to-turn short fault, produces an average rotor velocity of 463.17 degrees per second; only 83% of the no-fault case. This rotor velocity damping is due to a damping current induced in the shorted portion of the faulted coil by the relative motion of the permanent magnet rotor.

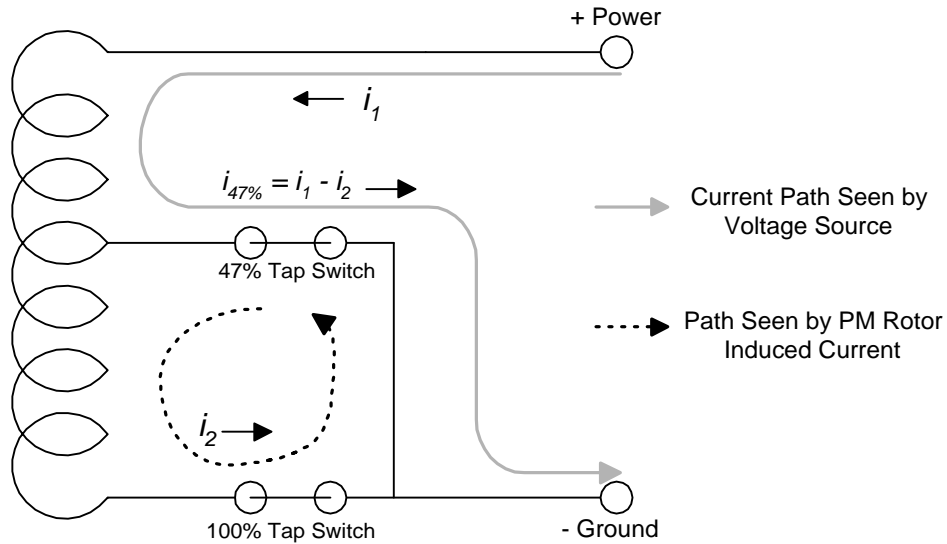


Figure 4-18. Power source and back emf induced current paths in the turn-to-turn faulted coil.

Figure 4-18 shows a diagram of the experimental fault simulation phase configured for the turn-to-turn fault. The path seen by current from the power source is indicated by the gray line, i_1 . i_1 only flows when the phase is commutated (i.e. when it is energized by the source). As the rotor moves in relation to the stator coils, an emf is induced. In the turn-to-turn fault, there is a closed circuit that permits current flow. The path seen by the current, i_2 , due to the PM rotor induced emf is shown by the dotted line in Figure 4-18. i_2 produces a back mmf that opposes rotor motion at all times during its rotation. As a result, there is a damping of the rotor velocity for a given constant source voltage.

In order to investigate the current induced in the faulted portion of the experimental fault simulation phase coil, the current through the 47% tap switch, $i_{47\%tap}$, can be written in terms of the currents, i_1 and i_2 , shown in Figure 4-18.

$$i_{47\%tap} = i_1 + i_2 \quad (4-13)$$

It is clear from this expression that i_2 , the current induced in the faulted portion of the coil, can be obtained by subtracting i_1 from $i_{47\%tap}$. It is evident from the current data shown in Figure 4-17 of the previous section that no current flows through the 47% tap switch in the no-fault or open-phase fault cases. For the reduced-coil fault case and the turn-to-turn fault case, i_2 was calculated via equation (4-13). These results are shown in Figure 4-19 and represent current flowing only in the faulted portion of the coil. It is clear that there is no net current induced by the faulted portion of the coil in the reduced coil case. In contrast, the turn-to-turn case clearly shows a current that persisted throughout the rotation of the rotor.

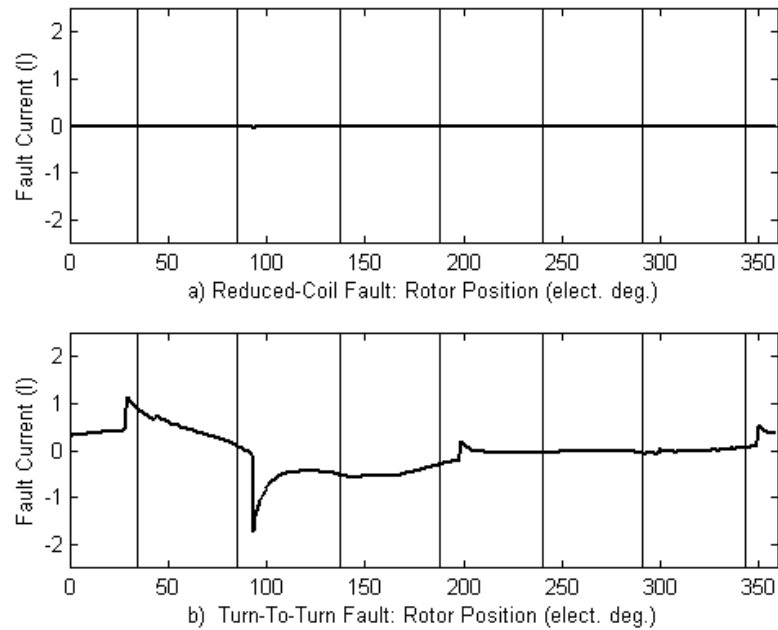


Figure 4-19. Net current flow in the faulted portion of the experimental fault simulation coil in the reduced-coil fault case (a), and the turn-to-turn fault case (b).

The case 3 turn-to-turn short fault differs significantly from the other cases. It alters the behavior of the faulted phase coil not only when the faulted phase coil is energized by the power source during its commutation phase, but also when it is disconnected from the power source during the commutation of the other phases. As in the case of an insulation failure induced coil short, the turn-to-turn short fault creates a closed circuit loop that remains, even when the phase is not energized by the source. This results in a damping torque as the PM rotor moves in relation to the closed current loop and induces a current flow. The induced current persists during the entire rotation of the rotor.

Formulation of a mathematical expression for damping torque

To investigate this damping torque further, we will use the torque equation (4-5) from the mathematical modeling section to describe the interaction between the rotor and the faulted portion of the coil:

$$T_{damp} = \frac{1}{2}(i_{damp})^2 \frac{\partial L_{fault}}{\partial(\theta)} \quad (4-14)$$

where T_{damp} , i_{damp} , and L_{fault} are the damping torque, the current induced in the faulted portion of the coil, and the inductance of the faulted portion of the coil, respectively. For clarification i_{damp} is shown as i_2 in Figure 4-18. The only difference between the inductance associated with an unfaulted coil, and the inductance of the faulted portion of the experimental fault simulation coil, is reflected in the number of winding turns. With this in mind, and using equation (1.5) from section III, we can express the partial of $L_{fault}(\theta)$ with respect to θ , as

$$\frac{\partial L_{fault}(\theta)}{\partial \theta} = N_{fault} k_{L_{fault}} \frac{\partial l_m(\theta)}{\partial \theta} \quad (4-15)$$

In this case, l_m , the unit function representing the variable part of the flux path, is the same as for the unfaulted coil. In addition, $k_{L_{fault}}$ is also unchanged from its no-fault value. Therefore $k_{L_{fault}}$ can be replaced by k_L in equation (4-15). Since we are

considering only one coil, we will drop the m subscripts. Introducing $N = N_{noFault}$ into equation (4-15), and substituting this into (4-14) we can now express the turn-to-turn fault damping torque in terms of i_{damp} (the current in the faulted portion of the coil) and a faulted turns ratio:

$$\begin{aligned} T_{damp} &= \frac{1}{2} (i_{damp})^2 \left(\frac{N_{fault}}{N_{noFault}} \right) N_{noFault} k_L \frac{\partial l(\theta)}{\partial(\theta)} \\ &= \frac{1}{2} (i_{damp})^2 \left(\frac{N_{fault}}{N_{noFault}} \right) \frac{\partial L(\theta)}{\partial(\theta)} \end{aligned} \quad (4-16)$$

This damping torque always opposes the motion of the rotor, since the origin of the current is the rotor induced back emf.

In a healthy phase, a back emf will also be induced, but this is only associated with a current flow when the phase is energized by the power source. In this instance, there is a closed circuit, including the power source. When a healthy phase is not energized by the power source, only a very small amount of current will conduct during open circuit charging and discharging of the coil as the rotor moves in relation to the phase coils. In this case, since there is very little current flow, no back mmf will be generated.

Prediction of rotor velocity from measured currents in the turn-to-turn fault case

To tie the experimental results to the mathematical description of the motor, we would like to express the ratio of the faulted steady state average torque to the average no fault torque in terms of measured currents. This will allow us to predict the expected percent reduction in average motor torque due to the turn-to-turn short induced damping.

We will consider the behavior of the 6 out of 7 remaining healthy phases under the influence of the turn-to-turn fault. Here, we will focus on the torque reduction due to damping, and neglect the changes in the positive torque production when the faulted

phase is energized during its commutation phase. We will address overall average steady-state torque from the point of view of average torque developed by the motor when one of the healthy phases is energized. In this case, the total average fault condition torque, T_{fault} , is given by

$$T_{fault} = T_{healthy} - T_{damp} \quad (4-17)$$

Where $T_{healthy}$ is the torque generated by a non-faulted phase, and T_{damp} is given in equation (4-16) above. Since the phases in this motor are both electrically and magnetically isolated, torque production in the healthy phases is not affected by the fault, although the overall motor torque is reduced due to the damping torque.

Substituting equation (4-5) from the math modeling section and (4-16) into (4-17) we get

$$\begin{aligned} T_{fault} &= T_{healthy} - T_{damp} \\ &= \frac{1}{2}(i_{healthy})^2 \frac{\partial L(\theta)}{\partial \theta} - \frac{1}{2}(i_{damp})^2 \left(\frac{N_{fault}}{N_{noFault}} \right) \frac{\partial L(\theta)}{\partial \theta} \\ &= \left((i_{healthy})^2 - \frac{1}{2}(i_{damp})^2 \left(\frac{N_{fault}}{N_{noFault}} \right) \right) \frac{1}{2} \frac{\partial L(\theta)}{\partial \theta} \end{aligned} \quad (4-18)$$

Here, again, we have replaced the m subscripts with *fault*, *healthy*, or *damp*, to clarify each term. Since only one phase is energized at a time with the brushless driver, and since the healthy phases are assumed to be similar, equation (4-18) represents the summation of equation (4-6) and can be used for average overall motor torque. Equation (new 5) and (4-18) can be combined to express the ratio of the no fault torque to the turn-to-turn fault torque:

$$\begin{aligned} \frac{T_{fault}}{T_{healthy}} &= \frac{\left((i_{healthy})^2 - (i_{damp})^2 \left(\frac{N_{fault}}{N_{noFault}} \right) \right) \frac{1}{2} \frac{\partial L(\theta)}{\partial \theta}}{(i_{healthy})^2 \frac{1}{2} \frac{\partial L(\theta)}{\partial \theta}} \\ &= \left(1 - \frac{(i_{damp})^2}{(i_{healthy})^2} \left(\frac{N_{fault}}{N_{noFault}} \right) \right) \end{aligned} \quad (4-19)$$

Neglecting changes in overall motor torque other than those due to the damping, equation (4-19) can be used to predict the average percent of torque reduction due to the damping current, i_{damp} (shown as i_2 in Figure 4-18). This is expressed in terms of measured currents and the ratio of the number of turns shorted to the number of turns in a healthy phase.

Noting that the second term in equation (4-19) is linear in current squared, we can use equation (4-19) to estimate overall average faulted motor torque as a percent of the no-fault torque. This is done by substituting the measured average squared current values over a suitable range. The current wave form due to the power source repeats once every commutation phase period, so it is averaged over one phase sector. The damping current wave form repeats every 360 electrical degrees so it is averaged over one complete commutation cycle.

To illustrate the use of equation (4-19), we will plug in current data from the turn-to-turn fault simulation case (case 3). The current data measured in the healthy phase, and the damping current measured in the 47% turn-to-turn faulted phase, were squared and averaged. Applying these to equation (4-19) gives the following result:

$$\begin{aligned} \text{mean} \frac{T_{fault}}{T_{healthy}} &= \left(1 - \frac{(i_{damp})^2}{(i_{healthy})^2} \left(\frac{N_{fault}}{N_{noFault}} \right) \right) \\ &= 1 - \frac{(0.1645)^2}{(0.3258)^2} \left(\frac{143}{270} \right) \\ &= 0.7324 \end{aligned} \tag{4-20}$$

To relate this average torque to the angular velocity data gathered, we refer to equation (4-7) from the mathematical modeling section. At steady state, there is no net acceleration over the period of one complete revolution of the rotor. In addition, the data used in equation (4-20) were collected under no-load conditions. In this case, equation (4-7) can be written for overall mean torque as follows:

$$\begin{aligned} \text{mean}(T_{\text{fault}}) &= \text{mean}\left(J \frac{d\omega}{dt} + B\omega + T_l\right) \\ &= \text{mean}(B\omega) \end{aligned} \quad (4-21)$$

Hence, for the no-load average case, rotor velocity is proportional to overall torque generation. Relating this to the average rotor velocity results presented for the turn-to-turn fault case, we see that a velocity of 73.2% of the no-fault case is predicted. This is a reduction of 27.8% from the no-fault case. The actual measured average rotor velocity was 83.3% of the no fault value.

This discrepancy can be accounted for by noting that the altered behavior of the faulted coil, when energized, was neglected in the above analysis. From the reduced-coil fault (case 2), which is not associated with damping, average rotor velocity of 107.8% of the no-fault value was reported. In both the reduced-coil fault and the turn-to-turn fault cases, the same amount of current is drawn from the power source to within 0.2% (302.6% and 303.2% of the no-fault mean current draw, respectively). Since in both of these cases, the same number of torque producing turns remain in the faulted phase (i.e. 47%), it is reasonable to assume that positive torque production in the faulted phase is similar in both cases. From the data collected in the reduced-coil case, we see that there is an overall increase of 7.8% in average rotor velocity compared to the no-fault case.

Using the result in equation (4-20) and (4-21) in conjunction with the percent velocity increase due to the altered behavior of the faulted phase when energized from the power source, an average velocity of 81.0% of the no fault velocity is predicted in the turn-to-turn case. This result differs by 2.3% from the actual measured velocity.

Identification of turn-to-turn faults from rotor velocity data

The voltage and current traces are similar in the cases of fault 2 and 3 (see panels (e) and (f) in Figures 4-10 and 4-11). The current induced in the shorted coils is not detected by the external current sensor, since it flows entirely in the interior of the coil. This current

can be an order of a magnitude higher than rated current [52][40] and can lead to a cascade failure in the coil as heat generated in the shorted turns deteriorates the insulation of neighboring turns, and introduces more shorts. A safety hazard could result if a fault goes undetected and leads to the sudden catastrophic failure of the motor. Hence, it is desirable to have metric to characterize this fault. The results presented in this work suggest that a change in rotor velocity under conditions of constant load may be useful for detecting the turn-to-turn fault and differentiating it from other winding faults.

In the case of open loop voltage speed controllers, such as that used to drive the motor used in these experiments, a change in rotor speed can be detected as a result of the damping discussed above. In cases of constant velocity drives used on fault tolerant SR motors, an associated rise in current in the healthy phases can be detected as the driver compensates for the additional damping load caused by the faulted phase [47][21][15].

These results may be most applicable to open loop speed control systems, such as those used in some electric vehicles and machines designed to be operated directly by humans. Such systems are technically closed loop systems in which the operator (a human) is acting as a complex dynamic proportional controller. In such cases, under a known load, a particular input voltage will be associated with a particular rotor velocity in the no-fault condition. In some systems, it may be possible to detect a deviation from this expected velocity and report it independently of a dynamic in-the-loop controller such as a human.

VII. Conclusion

In this work, a prototype axial flux variable reluctance permanent magnet motor was discussed. This motor was designed to be a low power version of machines similar to a class of experimental electric vehicle propulsion motors. Motors of this type possess a

high degree of inherent fault tolerance and may continue to operate with relatively little degradation in torque production in the presence of relatively severe faults.

The motor was used to study stator winding faults. One of the motor's phases was modified so that it could be used to experimentally simulate stator winding faults. A National Instruments based data collection platform was used to collect relevant data during motor operation.

Data were presented for several types of stator winding Fault. In particular, turn-to-turn faults were examined. It was found that a major turn-to-turn fault is associated with a reduction in rotor velocity when the motor is driven with a brushless driver with closed loop rotor position feedback and open loop voltage speed control.

Fault characterization results such as those presented in this paper are a necessary first step in the process of fault detection and diagnosis in a particular motor topology.

Acknowledgments

The authors of this article would like to acknowledge the support of the National Science Foundation grants ECS-9521609 and ECS-9610509 which helped make the work at the ADAC lab possible.

References

See Thesis Bibliography.

Bibliography

- [1] J.G.W. West, "DC, Induction, Reluctance and PM Motors for Electric Vehicles", IEE Colloquium on Motors and Drives for Battery Powered Propulsion, Vol. 1, pp.1-11, 1993.
- [2] K. Rajashekara, 'History of Electric Vehicles In General Motors', IEEE Transactions on industrial Applications, vol. 30, no. 4, pp. 897-904, 1993.
- [3] M.E. Hanson, 'A New Era Begins: Report on NAEVI 98' Conference', <http://evworld.com>, Digital Revolution, 1998
- [4] J.G.W. West, "DC, Induction, Reluctance and PM Motors for Electric Vehicles", Power Engineering Journal, Vol. 8, No. 2, pp. 77-88, 1994.
- [5] R.B. Tribdino, "*Nissan Hypermini EV*", Raymond Tribdino and Digital Revolution, 1997.
- [6] C.C. Chan, K.T. Chau, 'An Overview of Power Electronics in Electric Vehicles', IEEE Transactions on Industrial Electronics, vol. 44, no.1 pp. 3-9, 1997.
- [7] K.M. Rahman, B. Fahimi, G. Suresh, A.V. Rajarathnam, M. Ehsani, "Advantages of Switched Reluctance Motor Applications to EV and HEV: Design and Control Issues", IEEE Transactions on Industrial Applications, Vol. 36, No. 1, pp. 111-121, 2000.
- [8] C.C. Chan, K.T. Chau, 'An Advanced Permanent Magnet Motor Drive System for Battery-Powered Electric Vehicles', IEEE Transactions on Vehicular Technology, vol. 45, no. 1, pp. 180-188, 1996.
- [9] D.P.Sen Gupta, J.W. Lynn, *Electrical Machine Dynamics*, Macmillan Press Ltd., New York, NY, 1980.
- [10] J.R. Hendershot Jr., TJE Miller, *Design of Brushless Permanent-Magnet Motors*, Clarendon Press, Oxford, 1994.
- [11] B.J. Chalmers, E. Spooner, O. Honorati, F.Crescimbin and F. Caricchi, "Compact Permanent Magnet Machines", Electric Machines and Power Systems, Vol. 25, pp. 635-648, 1997.

- [12] F. Profumo, Z. Zhang, A. Tenconi, 'Axial Flux Machine Drives: A New Viable Solution for Electric Vehicles', Transactions on Industrial Electronics, vol. 44, no.1 p39, 1997.
- [13] P.P. Mongeau, "High Performance Electric Vehicle Drivetrain Components", IEEE Transactions on Magnetics , Vol. 31, No. 1, pp.67-72, 1995.
- [14] J.F. Eastham, M.J. Balchin, T. Betzer, H.C. Lai and S. Gair, "Disc Motor with Reduced Unsprung Mass for Direct EV Wheel Drive", Proceedings of the IEEE International Symposium on Industrial Electronics, ISIE '95, Vol. 2, pp. 569-573, 10-14 July 1995.
- [15] S. Nandi, H. A. Toliyat, "Fault Diagnosis of Electrical Machines – A Review", Electric Machines and Drives, International Conference IEMD '99 Electric Machines and Drives", pp. 219-221, 1999.
- [16] G.M. Joksimovic, J. Penman, "Detection of Inter-Turn Short Circuits in the Stator Windings of Operating Motors", IEEE Transactions on Industrial Electronics", Vol. 47, No. 5, pp. 1078-1084, 2000.
- [17] M. Chow, "Motor Fault Detection and Diagnosis", IEEE Industrial Electronics Society Newsletter, Vol. 44, No. 4, pp. 4-7, 1997.
- [18] P. Goode and M. Chow, "Using a Neural/Fuzzy System to Extract Heuristic Knowledge of Incipient Faults in Induction Motors: Part I-Methodology", IEEE Transactions on Industrial Electronics, Vol. 42, no. 2, p. 131-138, 1995.
- [19] P. Goode and M. Chow, Using a Neural/Fuzzy System to Extract Heuristic Knowledge Of Incipient Faults in Induction Motors: Part II-Application, IEEE Transactions on Industrial Electronics, Vol. 42, no. 2, p. 139, 1995.
- [20] O. Moseler, D. Juricic, A. Raker, N Muller, "Model-Based Fault Diagnosis of an Actuator System Driven by a Brushless DC Motor", Proceedings of the 1999 American Control Conference, Vol. 6, pp. 3779-3783, 1999
- [21] C.M. Stephens, "Fault Detection and Management Systems for Fault Tolerant Switched Reluctance Motor Drives", IEEE Transactions on Industrial Applications, Vol. 27, No.6, pp. 1098-1102, 1991.
- [22] F. Caricchi et al, 'Compact Wheel Drive for EVs', IEEE Industrial Applications Magazine, Nov/Dec, pp. 25-32, 1996

- [23] J. Lai, Resonant Snubber-Based Soft-Switching Inverters for Electric Vehicles, Transactions on Industrial Electronics, vol. 44, no.1 p71, 1997.
- [24] B. Brant, *Build your Own Electric Vehicle*, McGraw-Hill, 1994.
- [25] S. D'Agostino, "The Electric Car", IEEE Potentials, Vol. 12, No.1, pp.28-32, 1993.
- [26] B. Aldrich, C. Chandler, *ABCs of AFVs a Guide to Alternative Fuel Vehicles, Fourth Edition*, The California Energy Commission, 1997.
- [27] B. Moore, The Sensible Ute Toyota RAV4-EV, EV World and Digital Revolution, 1998.
- [28] G.H. Chen and K.J. Tseng, Design of a Permanent-magnet Direct-driven Wheel Motor Drive for Electric Vehicles, Record of the IEEE PESC, June 23-27, pp.1933-1939, 1996.
- [29] M Terashima et al, Novel Motors and Controllers for high-performance Electric Vehicles with Four Wheel Motors, Transactions on Industrial Electronics, vol. 44, no.1 p28, 1997.
- [30] R. Krishnan, "A Novel Single-Switch-Per-Phase Converter Topology for Four-Quadrant PM Brushless DC Motor Drives", IEEE Transactions on Industrial Energy Applications, Vol. 33, No. 5, pp. 1154-1161, 1997.
- [31] D. Patteson and R. Spee, "The Design and Development of an Axial Flux Permanent Magnet Brushless DC Motor for Wheel Drive in a Solar Powered Vehicle", Industry Applications Society Annual Meeting, Conference Record of the 1994 IEEE, Vol. 1, pp. 188-195, 2-6 Oct. 1994.
- [32] D.C. Hanselman, *Brushless Permanent-Magnet Motor Design*, McGraw-Hill, Inc., 1994.
- [33] S.A. Nasar, I. Boldea, L.E. Unnewehr, *Permanent Magnet, Reluctance, and Self-Synchronous Motors*, CRC Press, 1993.
- [34] M.M. Radulescu, C. Martis, K. Biro, "A New Electronically-Commutated Doubly-Salient Permanent Magnet Small Motor", Electric Machines and Drives Conference 11-13 Sept. 1995, IEE Conference Publication No. 412, pp. 213-216, 1995.
- [35] N. Iwabuchi, A. Kawahara, T. Kume, T. Kabashima, N. Nagasaka, "A Novel High-Torque Reluctance Motor with Rare Earth Magnet", IEEE Transactions on Industrial Applications, Vol., 30, No. 3, pp. 609-614, 1994.

- [36] M.R. Harris, B.C. Mecrow, "Variable Reluctance Permanent Magnet Motors for High Specific Output", Sixth International Conference on Electric Machines and Drives, IEEE, pp. 437-442, 1993
- [37] K. Atallah, F. Caparrelli, C.M Bingham, P.H. Meller, D. Howe, C. Cossar, L. Kelly, P. Kjaer, J. Gribble, T.J.E. Miller, R. Capwell. C. Whitey, "Comparison of Electric Drives for Flight Control Surface Actuation", Ninth International Conference on Electric Machines and Drives (Conf. Publ No. 468), pp. 159-163, 1999.
- [38] C.C. Chan, J.Z. Jiang, H.G. Chen, X.Y. Wang, K.T. Chau, IEEE Transactions on Industrial Applications, vol. 30, No. 5, pp. 1258-1266, 1994.
- [39] C.C. Chan, K.T. Chau, J.Z. Jiang, W. Xia, M. Zhu, R. Zhang, "Novel Permanent Magnet Drives for Electric Vehicles", IEEE Transactions on Industrial Electronics, Vol. 43, No. 2, pp. 331-339, 1996.
- [40] J.A. Haylock, B.C. Mecrow, A.G. Jack and D.J. Atkinson, "Operation of Fault Tolerant Machines With Winding Failures", IEEE Transactions on Energy Conversion", Vol. 14, No. 4, pp.1490-1495, 1999.
- [41] B. Fahimi, G. Suresh, J. Mahdavi, M. Ehsani, "A New Approach to Model Switched Reluctance Motor Drive Application to Dynamic Performance Prediction, Control and Design", IEEE Power Electronics Specialists Conference, Vol. 2, pp. 2097-2102, 1998.
- [42] Y. Sozer, H. Kaufman, D.A. Torrey, "Direct Model Reference Control of Permanent Magnet Brushless DC Motors", Proceedings of the 1997 IEEE Conference on Control Applications, pp. 633-638, 5-7 Oct. 1997.
- [43] H. Yeo, C. Hong, J. Yoo, H. Jang, Y. Don, Y. Park, "Sensorless Drive for Interior Permanent Magnet Brushless DC Motors"
- [44] S.A. Nasar, I. Boldea, *Electric Machines Steady-State Operation*, Hemisphere Publishing Corp., 1990.
- [45] G. Amaratunga, K.W. Kwan, M. Tso, D.G. Crawley, "An Integrated Circuit for Driving A VR Step Motor as a Brushless DC motor", IEE Colloquium on Microcomputer Instrumentation and Control Systems in Power Electronics, pp. 4/1-4/4, 1988.
- [46] N. Hemati, "Dynamic Analysis of a Variable Reluctance Permanent-Magnet Brushless DC Motor", 23rd Annual IEEE Power Electronics Specialists Conference, PESC '92 Conference Record, Vol. 2, pp. 989-992, 1992.
- [47] A.G. Jack, B.C. Mecrow, J.A. Haylock, "A Comparative Study of Permanent Magnets and Switched Reluctance Motors for High Performance Fault Tolerant

Applications", Conference Record of the 1995 IAS IEEE Industry Applications Conference. Vol. 1, pp. 734-740, 1995.

[48] V.K.Shamra, S.S. Murthy, B. Singh, "Analysis of Switched Reluctance Drive under Fault Conditions", Conference Record of the 1998 33rd IAS IEEE Industry Applications Conference. Vol. 1, pp. 553-562, 1998

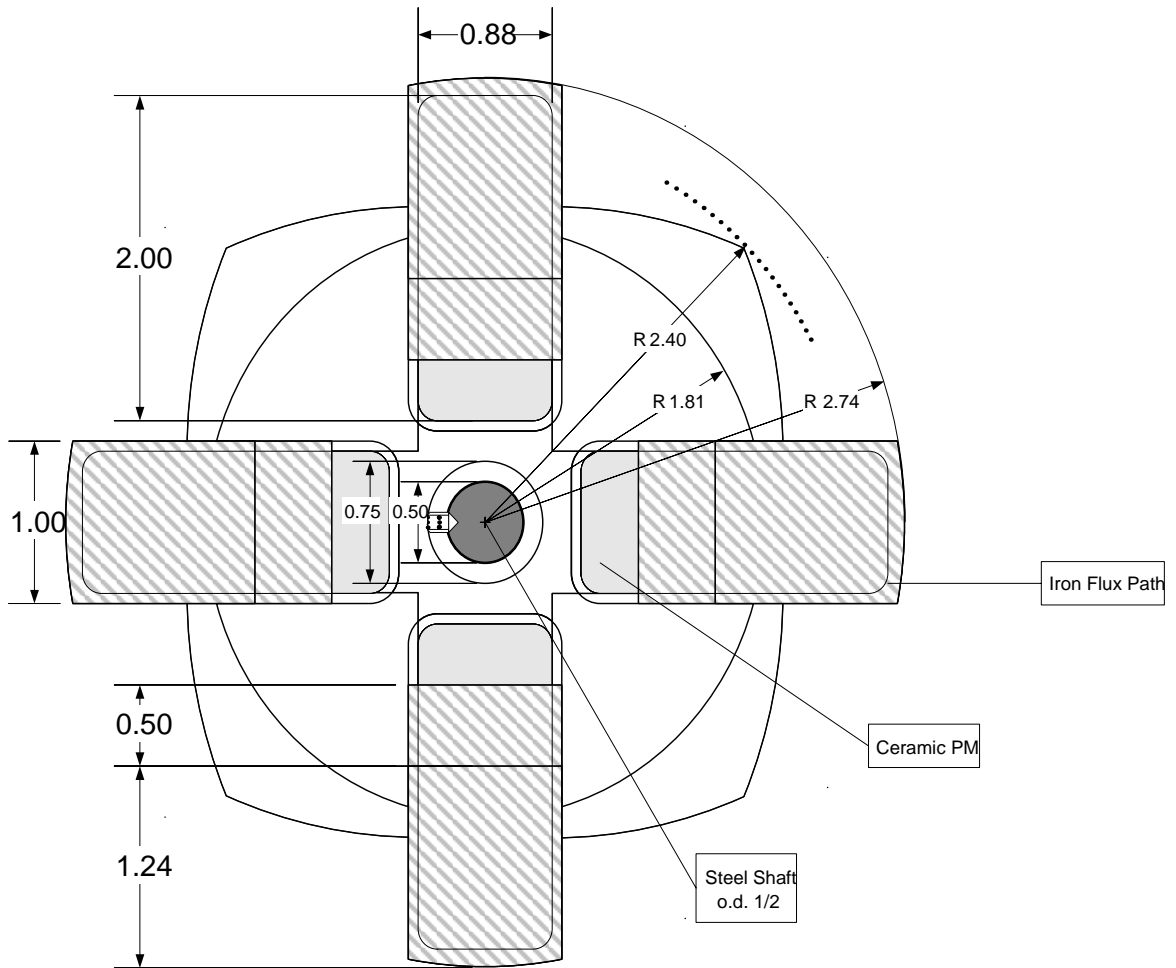
[49] A.L. Nelson and M. Chow, "Electric Vehicles and Axial Flux Permanent Magnet Motor Propulsion Systems", IEEE Industrial Electronics Society Newsletter, Vol. 46, No. 4, pp. 3-7, 1999.

[50] H.C. Lovart, V.S. Ramsden, B.C. Mecrow, "Design of an In-Wheel Drive for a Solar-Powered Electric Vehicle", Eighth International Conference on Electric Machines and Drives, Conf. Publ. No 444, pp. 234-238, 1997.

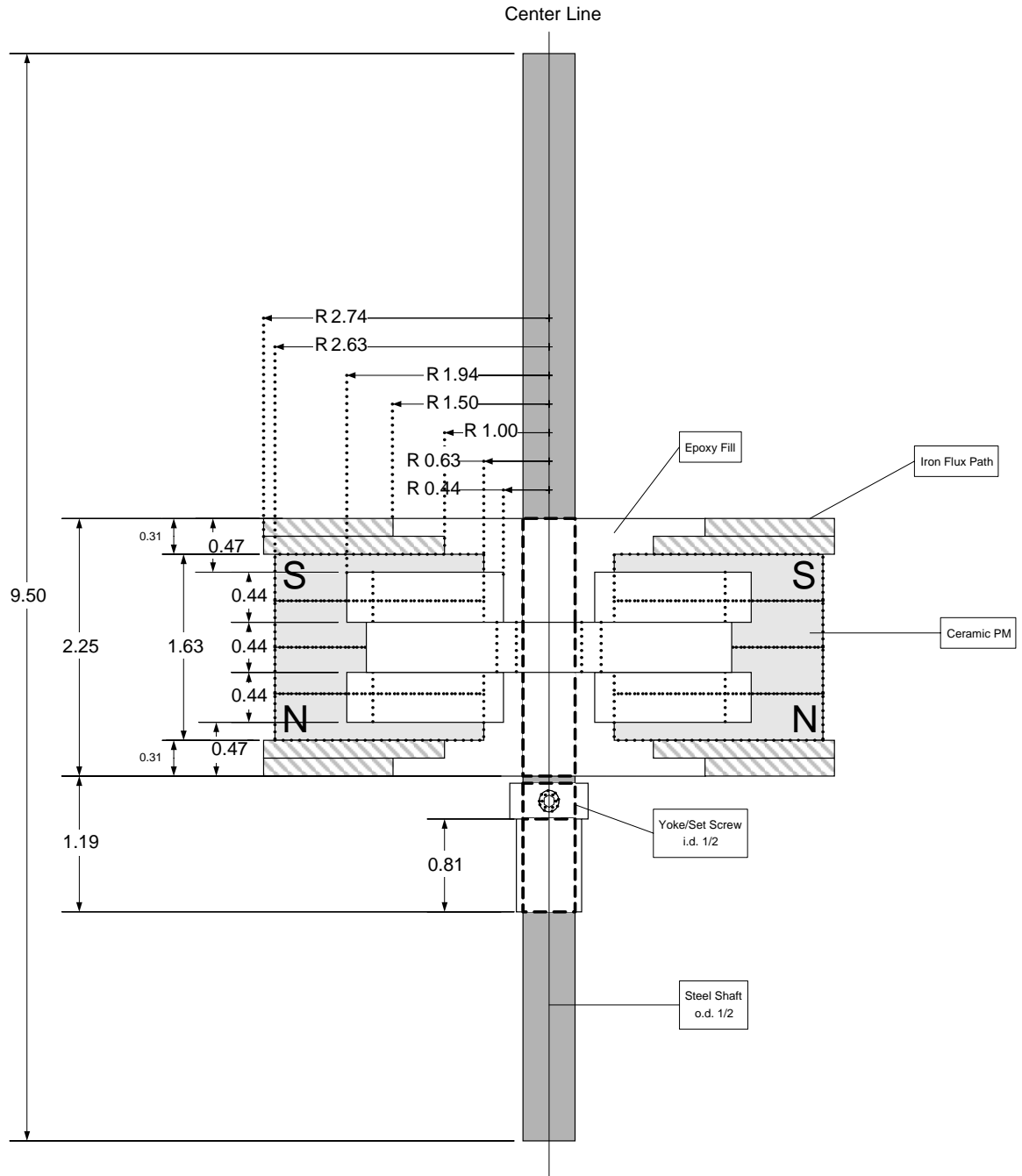
[51] I. Boldea, S.A. Nasar, *Electric Machine Dynamics*, Macmillan Publishing Co., New York, NY, 1986.

[52] F. Caricchi, F. Crescimbin, A. Di Napoli, "Prototype of Innovative Wheel Drive with Water-Cooled Axial-Flux PM Motor for Electric Vehicle Applications", IEEE APEC '96 Conference Proceedings, Vol. 2, pp. 764-770, 1996.

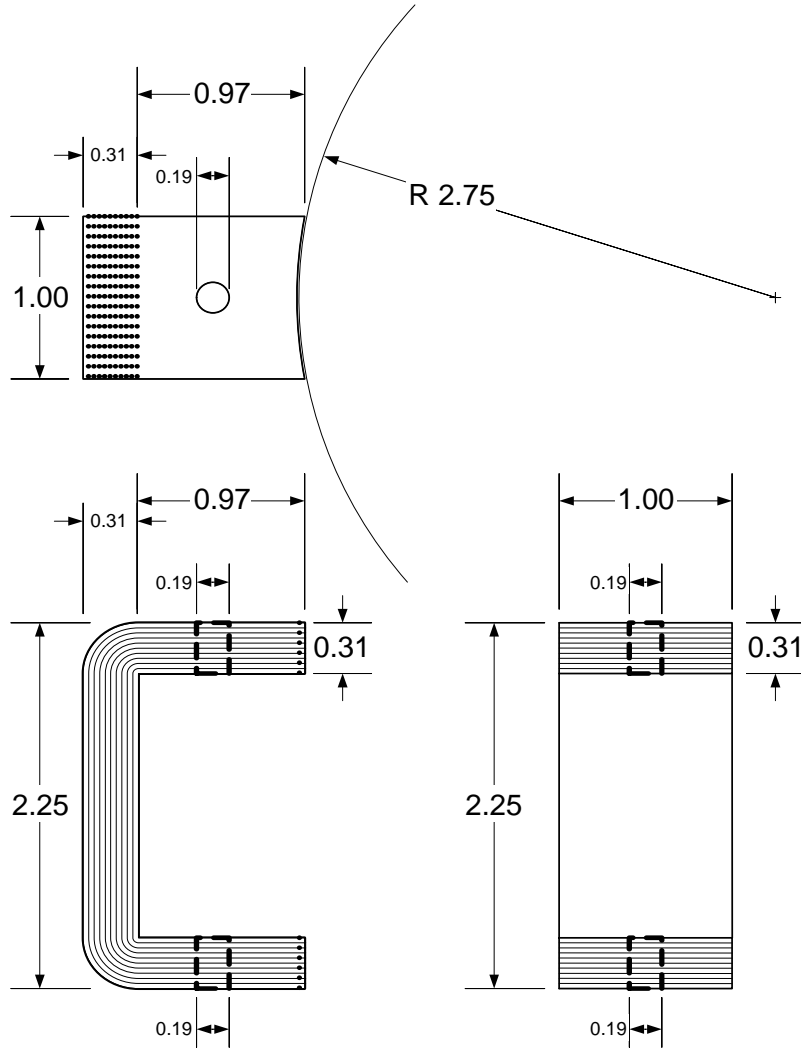
Appendix A: Motor Mechanical Drawings



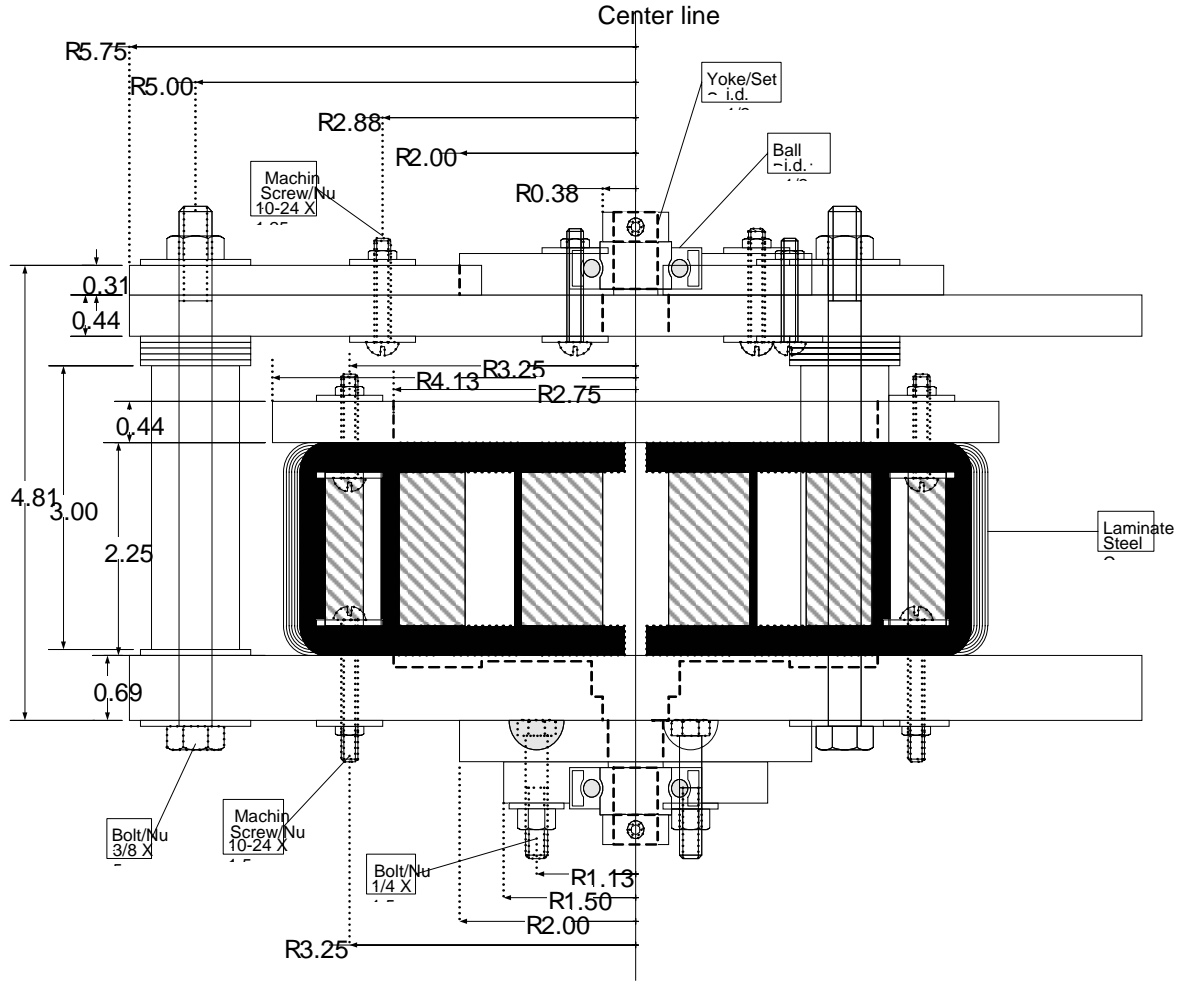
PM Rotor: Top View



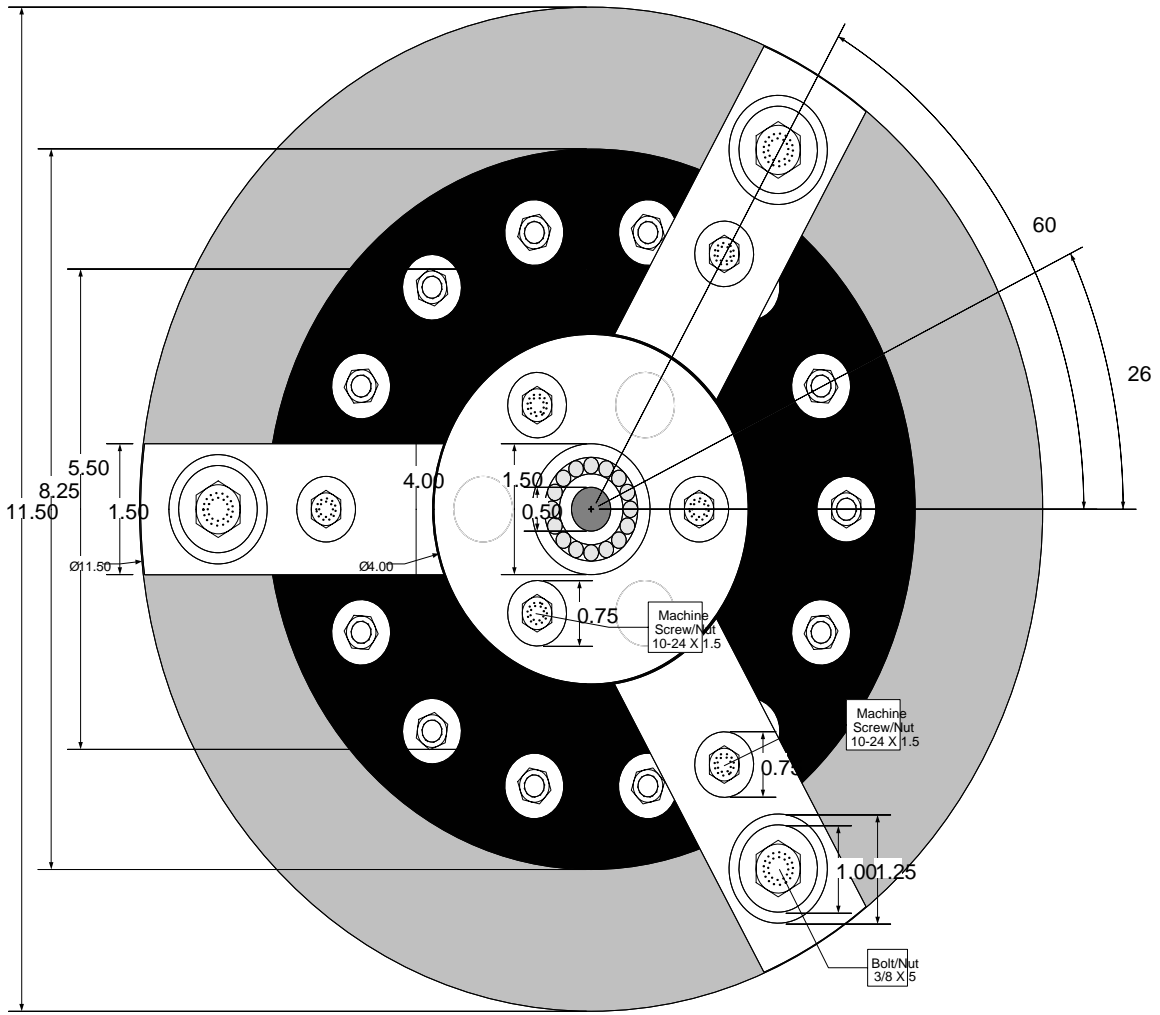
PM Rotor: Side View



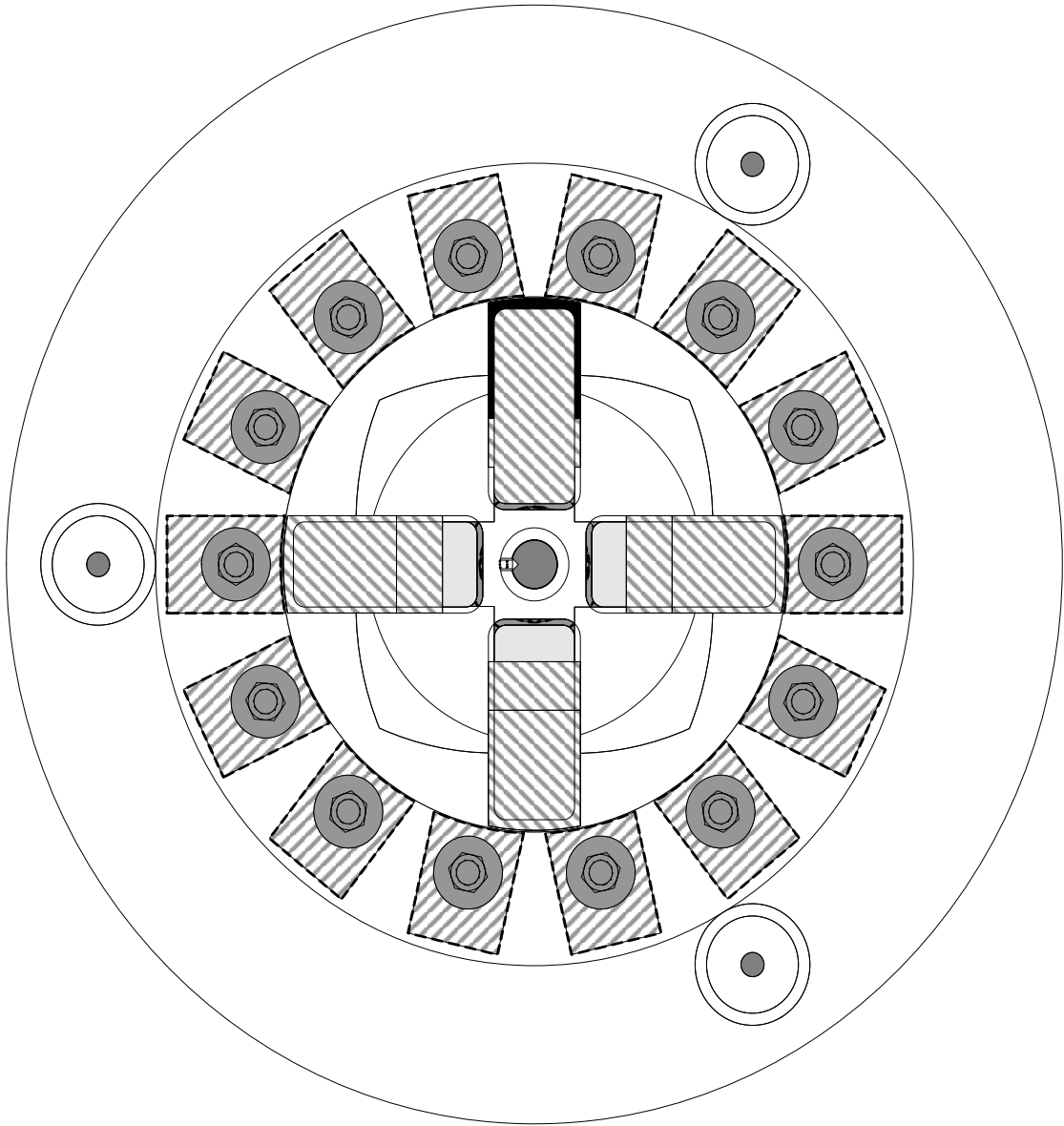
Laminated Stator Coil Core



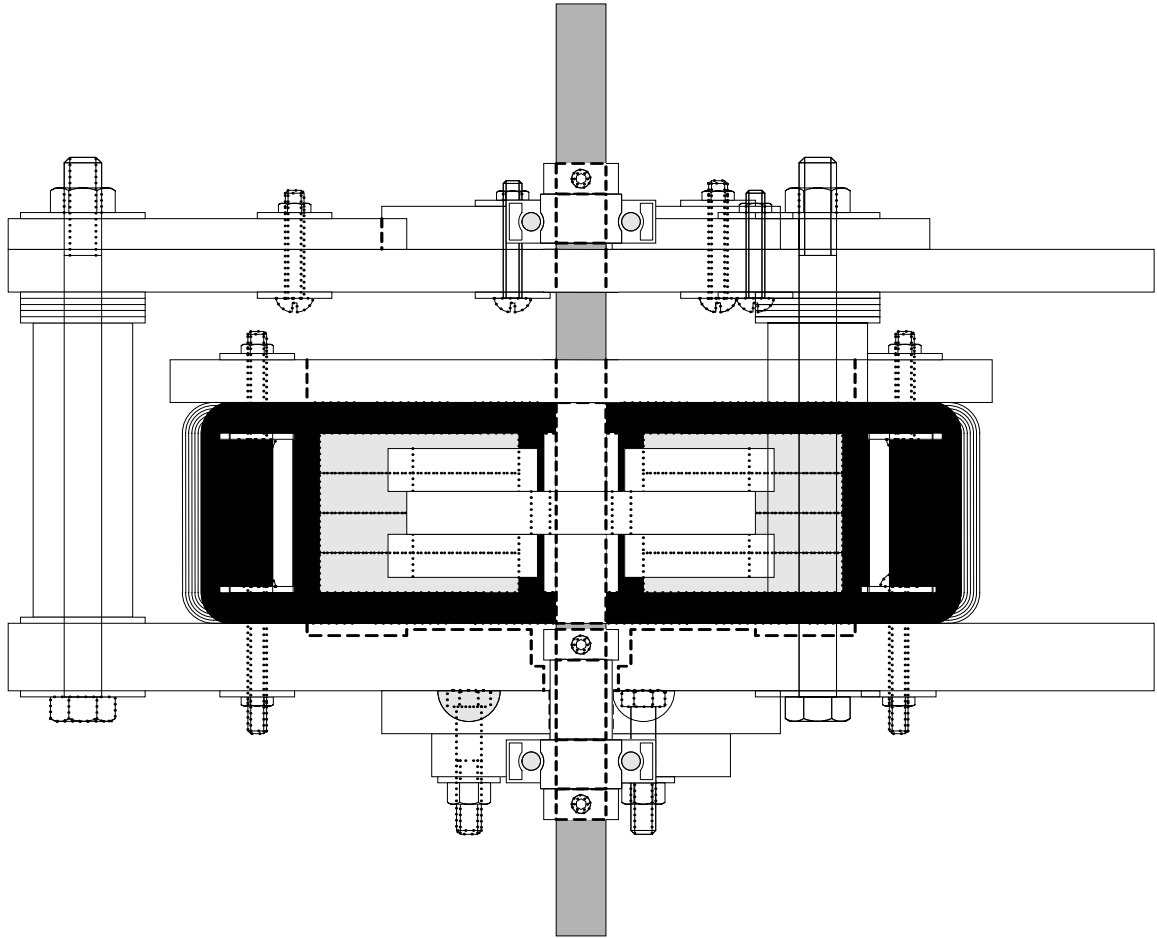
Stator: Side View



Stator Top Plate

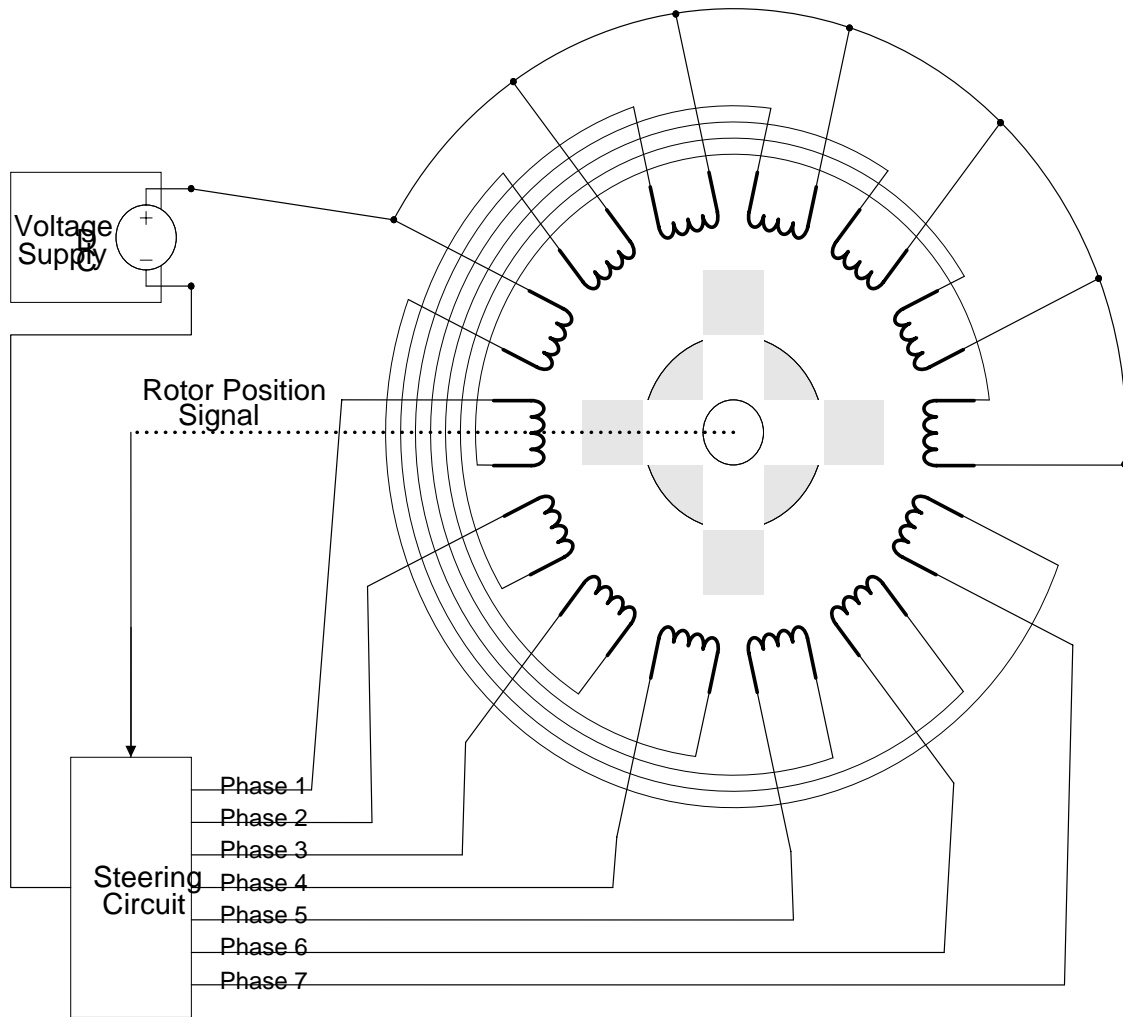


Rotor-Stator Assembly: Top View

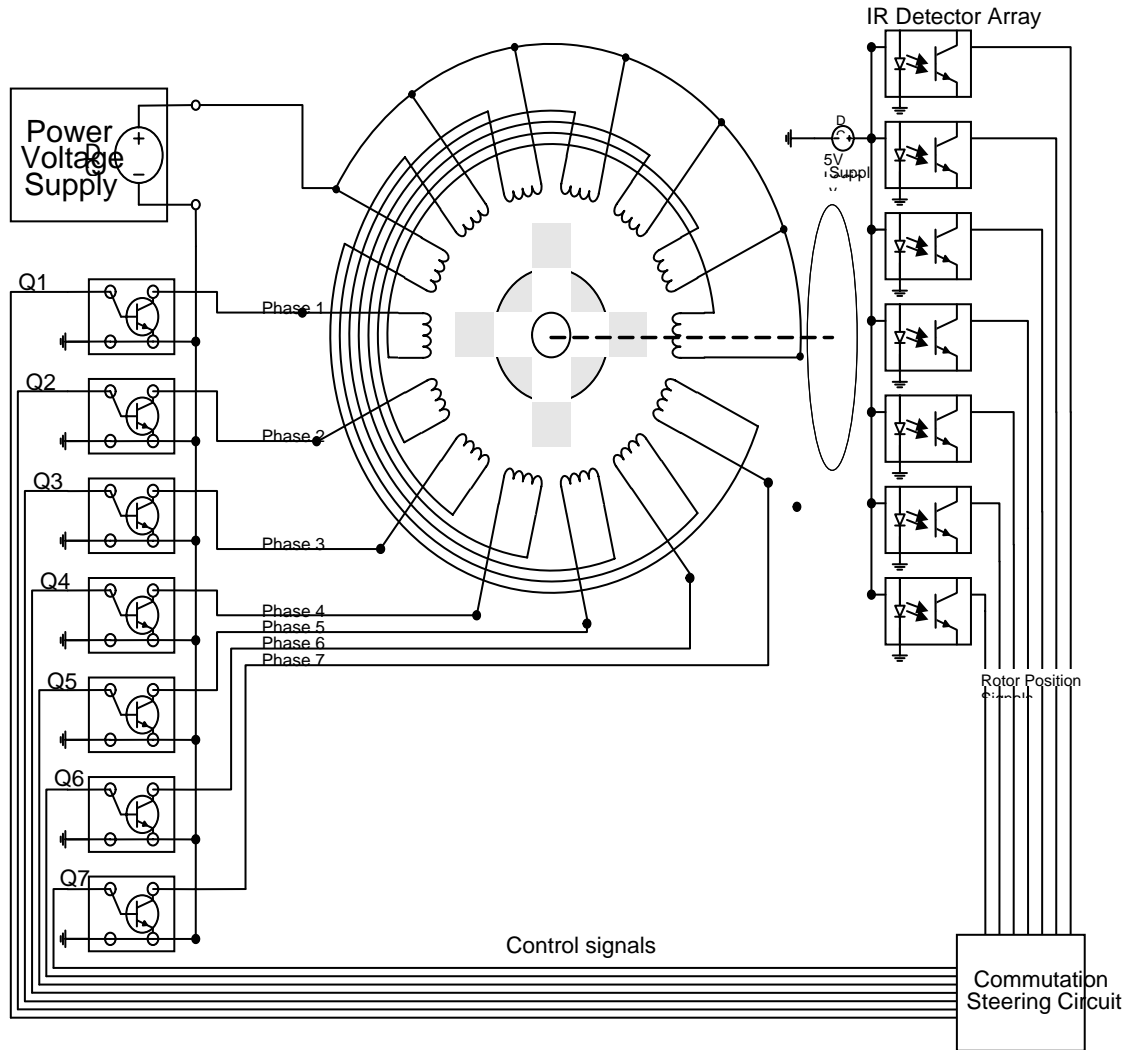


Rotor-Stator Assembly: Side View

Appendix B: Motor Electrical Schematics

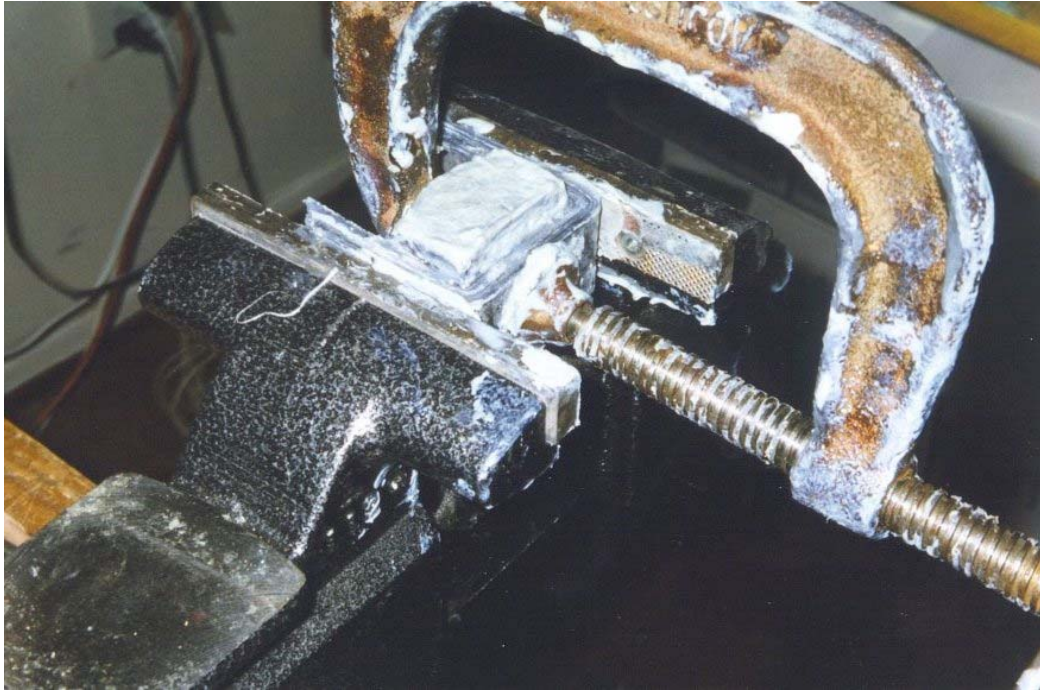


Motor Stator Coil Wiring Diagram

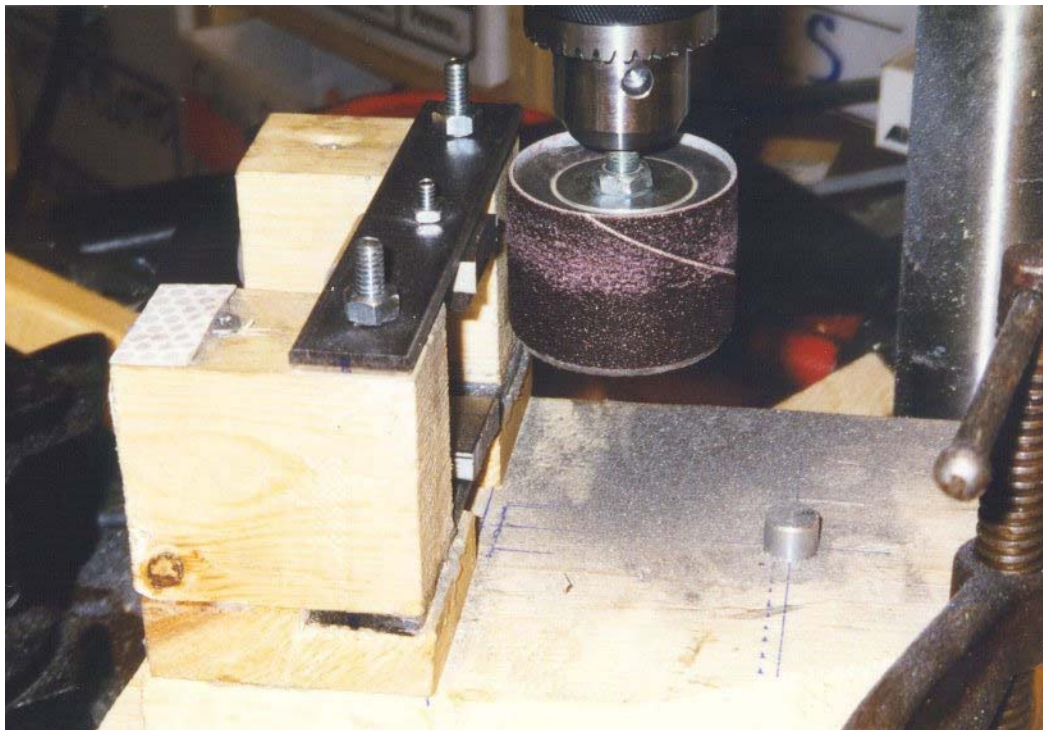


Brushless DC Commutator and Control Circuit

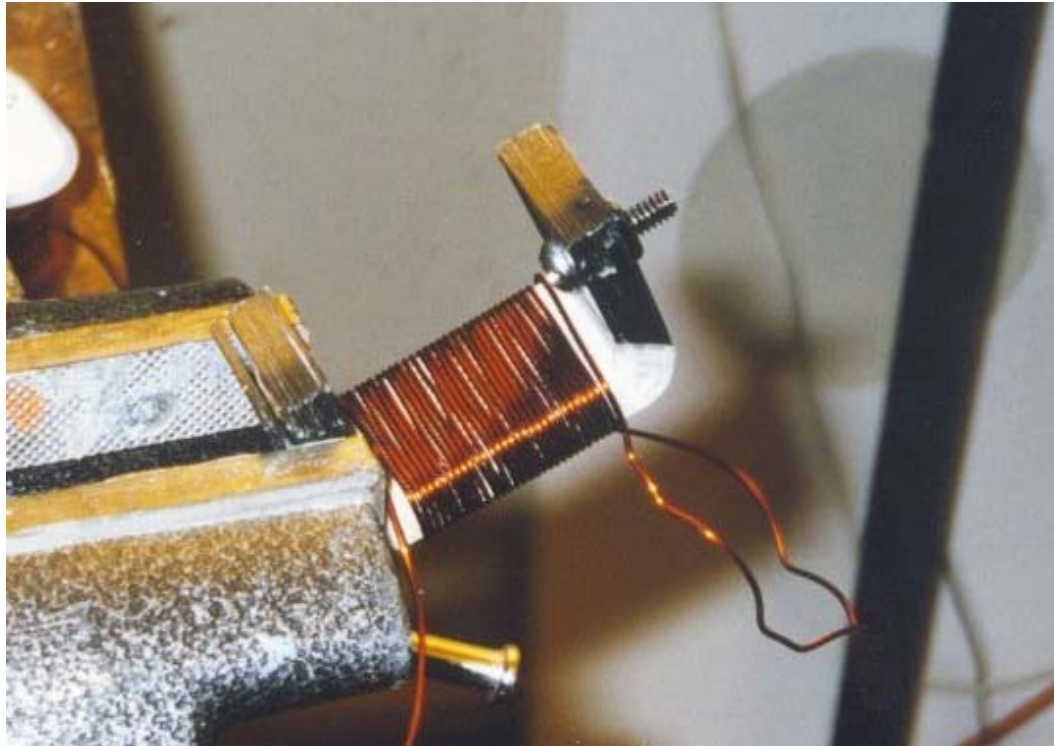
Appendix C: Motor Fabrication Photos



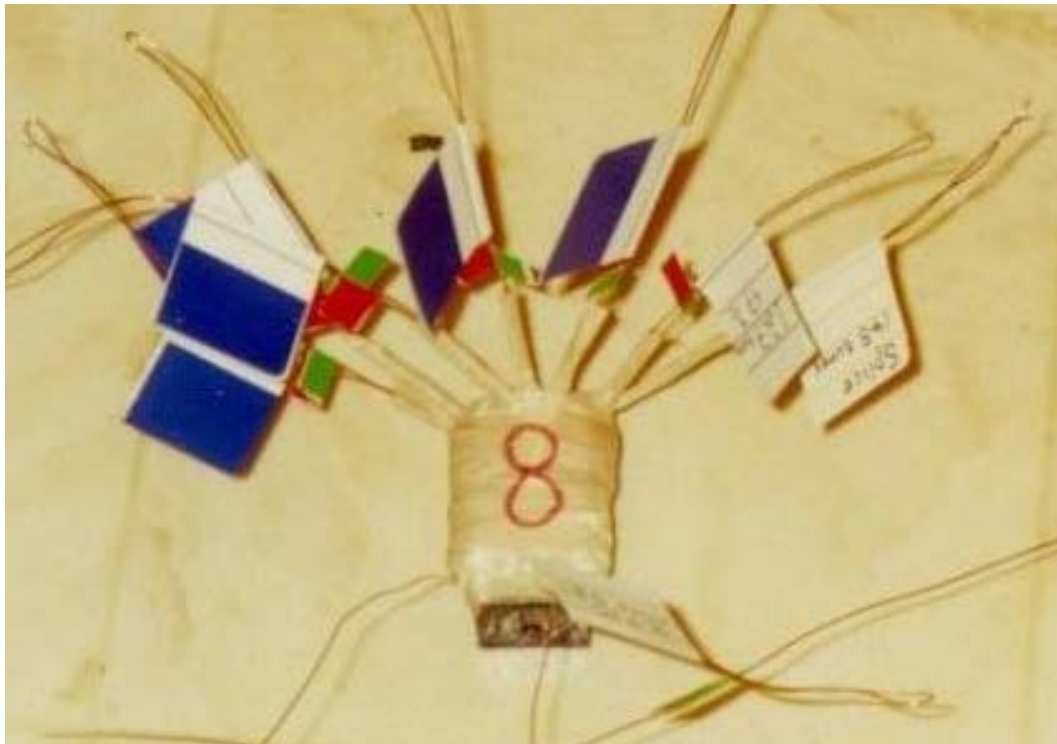
Forming laminated soft steel and epoxy stator coil core



Machining stator core flux path face



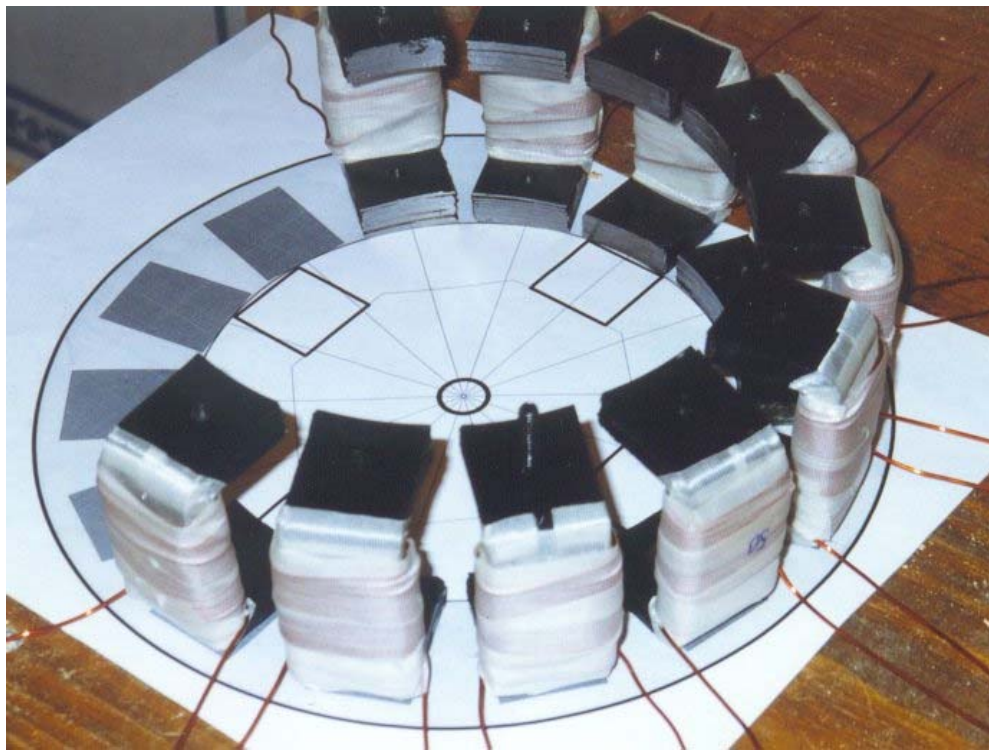
Winding stator core



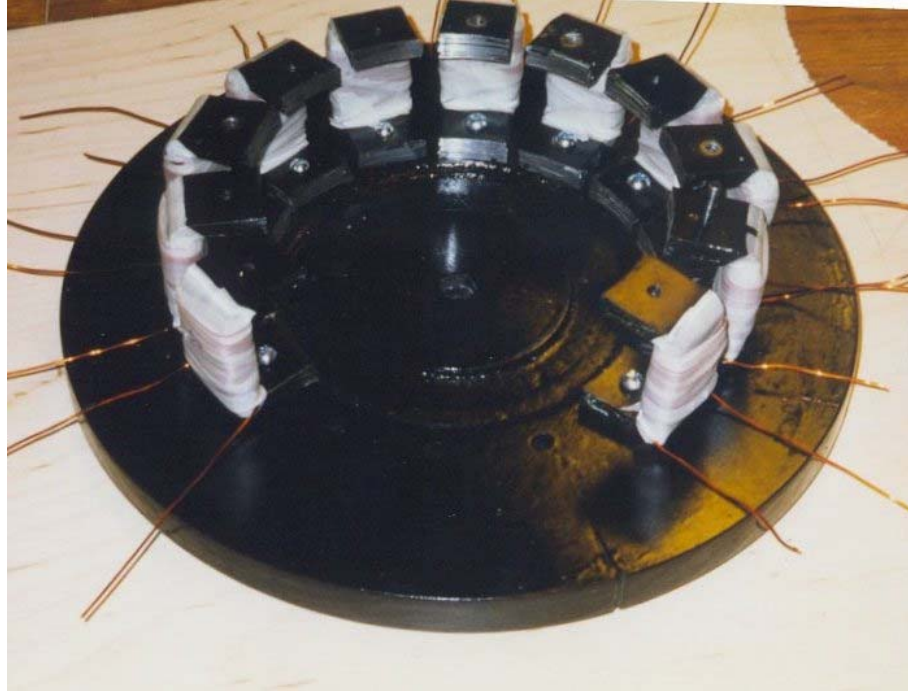
Wound stator core with fault simulation taps shown



Partial (unwound) stator core assembly



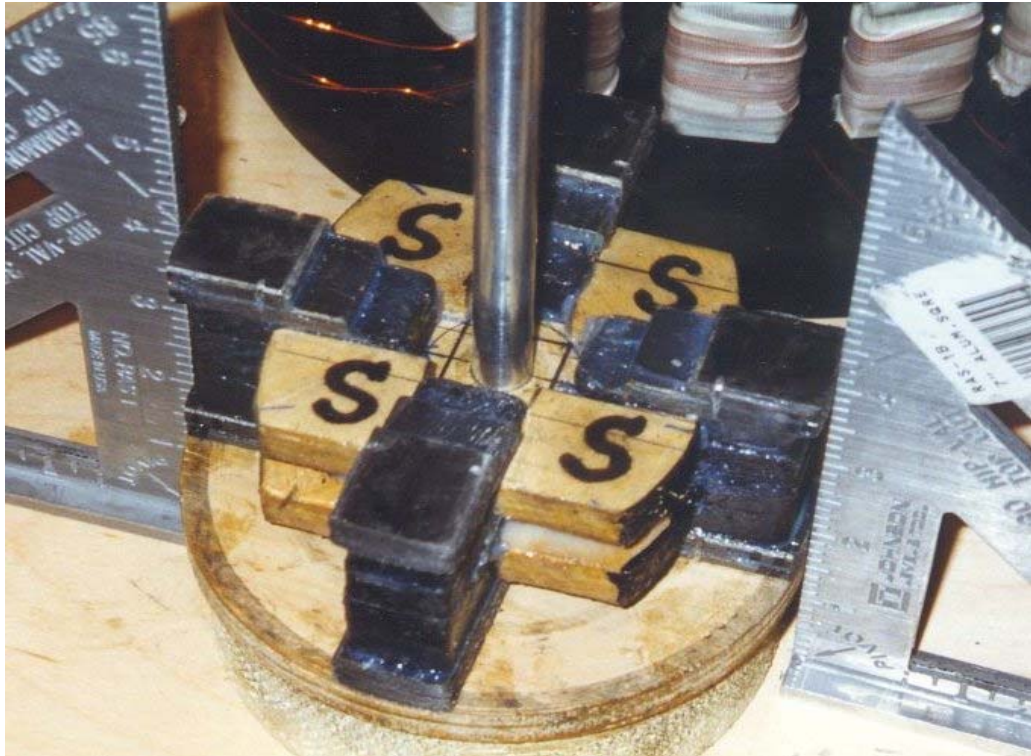
Partial (wound) stator core assembly



Partial stator assemble: 11 of 14 cores on back plate



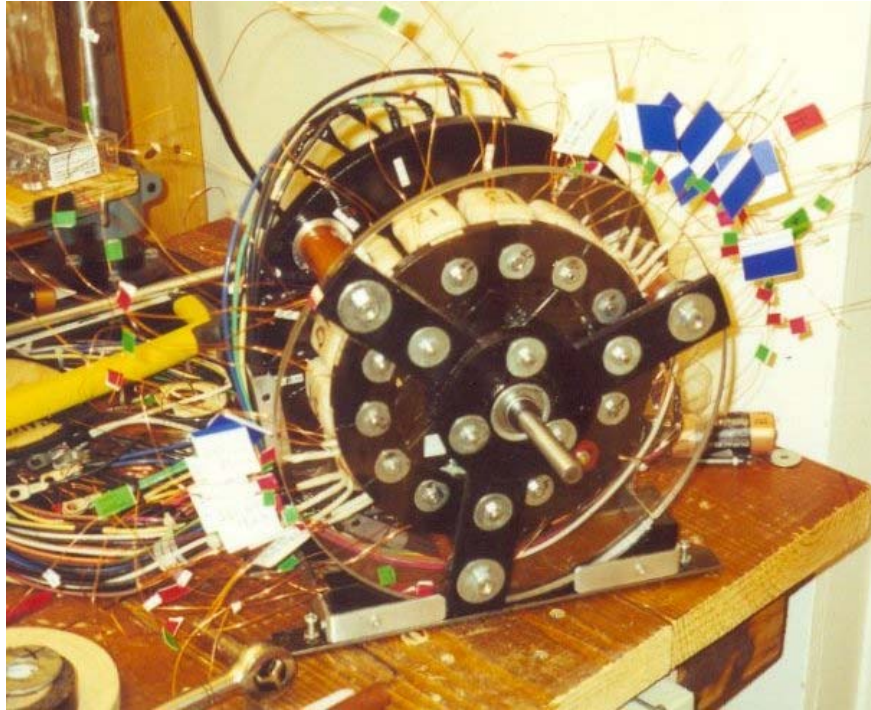
Complete stator assembly



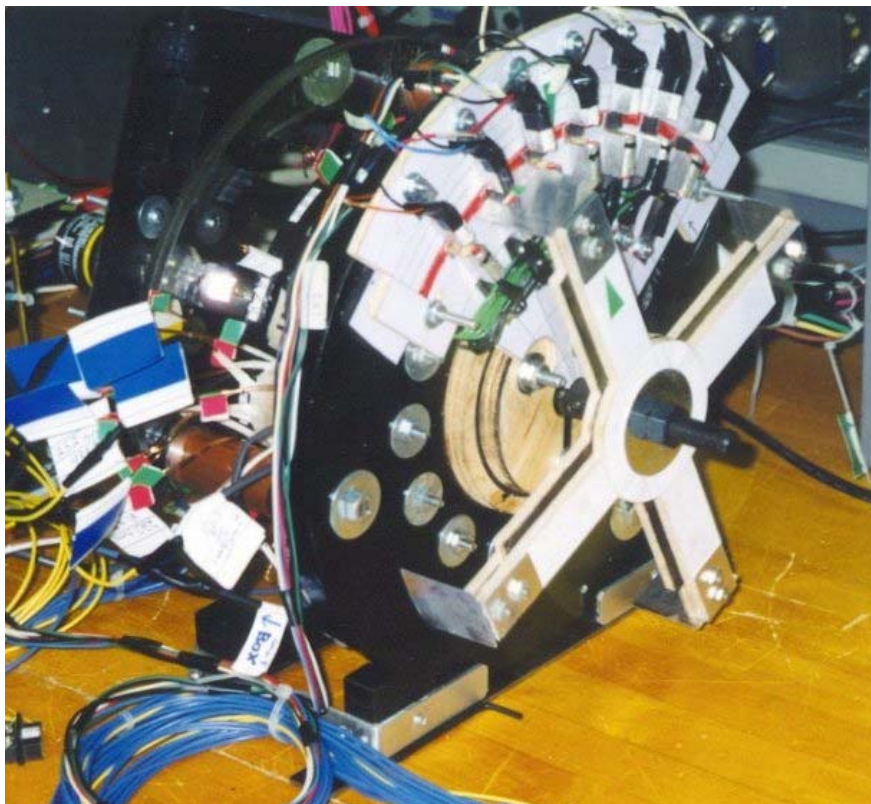
PM rotor assembly



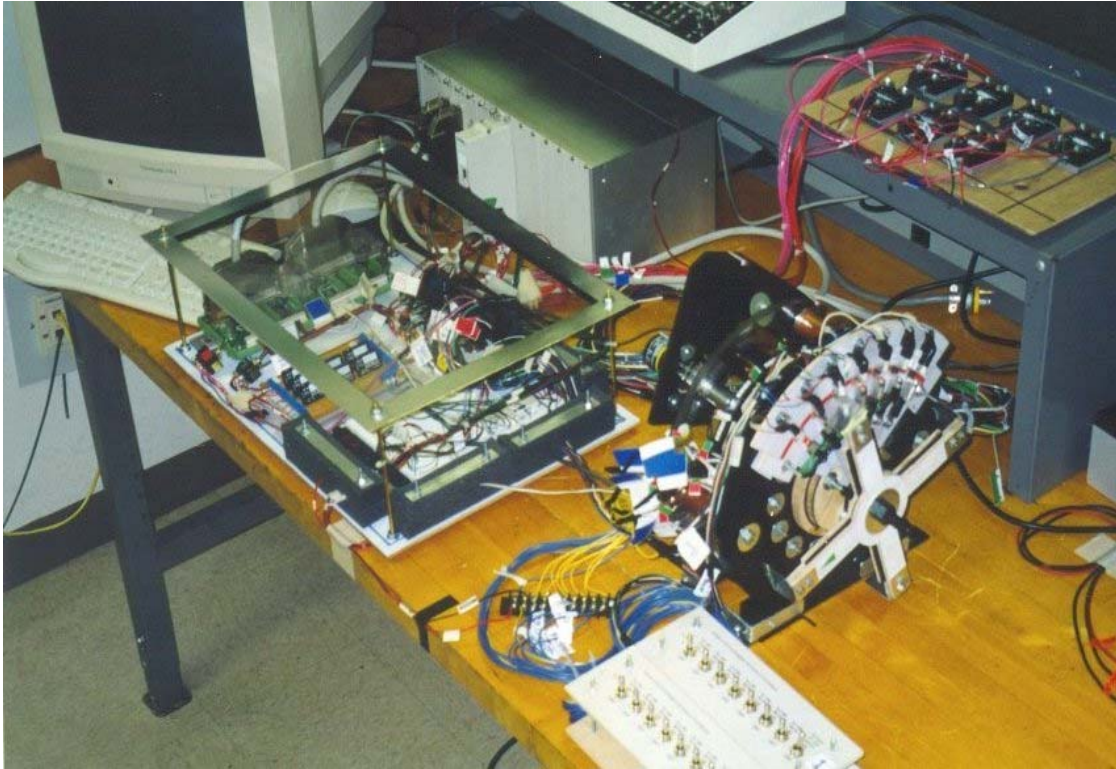
Stator assembly, rotor assembly, and motor top plate



Motor wiring



Motor with seven phase optical brushless commutator assembly



Research test bed setup including: motor, switching relays, driver and data collection electronics, computer, National Instruments main frame, and fault simulation switch box.

